NSF Grant ATM-9321361

National Science Foundation

RELATIONSHIP BETWEEN STORM STRUCTURE AND LIGHTNING ACTIVITY IN COLORADO CONVECTION OBSERVED DURING STERAO-A

by Timothy James Lang

Steven A. Rutledge, P.I.

Colorado State University

DEPARTMENT OF ATMOSPHERIC SCIENCE

PAPER NO. 651

RELATIONSHIP BETWEEN STORM STRUCTURE AND LIGHTNING ACTIVITY IN COLORADO CONVECTION OBSERVED DURING STERAO-A

by

Timothy James Lang

Department of Atmospheric Science

Colorado State University

Fort Collins, CO 80523

Research Supported by

National Science Foundation

under Grant ATM-9321361

November 1997

Atmospheric Science Paper No. 651

ABSTRACT

RELATIONSHIP BETWEEN STORM STRUCTURE AND LIGHTNING ACTIVITY IN COLORADO CONVECTION OBSERVED DURING STERAO-A

Concurrent measurements from the CSU-CHILL multiparameter Doppler radar, the ONERA VHF lightning interferometer, and the National Lightning Detection Network, obtained during Phase A of the Stratosphere-Troposphere Experiments: Radiation, Aerosols, Ozone (STERAO-A) field project, provided a unique data set with which to study the relationships between convective storm microphysics and associated lightning. Two events have been examined in detail: storms of 10 and 12 July 1996. Both storms underwent major organizational transitions during their lifetimes, identified by sharp changes in total lightning flash rates, dominant cloud-to-ground (CG) flash polarity, or dominant flash type (cloud-to-ground vs. intra-cloud). Both storms also featured relatively high intra-cloud (IC) flash rates.

The 10 July 1996 storm evolved from a multicellular line to an intense unicellular storm. The unicellular stage was marked by a sharp peak in IC flash rate as identified by the interferometer. Cloud-to-ground flash rates were low throughout the storm's lifetime. Small hail was produced during the entire observation period, suggesting storm updraft speeds were significant. The storm of 12 July evolved from an intense multicellular, hail-producing storm to a weaker rainstorm. Before this transition, hail was being produced and the CG flash rates were low. After the transition, hail was no longer being produced

and negative CG flash rates were significantly larger. Storm updraft speeds likely weakened during the transition.

These observations are consistent with the elevated-dipole hypothesis to explain low CG production in convective storms, especially if the observed high IC flash rates mostly neutralized any charged core before it descended toward the ground. Alternatively, if significant charging does not occur during wet growth of hail and graupel, both these storms might have produced enough wet-growth ice to prevent the generation of a lower positive charge center that could act to stimulate CG production. However, the radar data, in particular the linear depolarization ratio (LDR) data, suggest that dry growth was more prevalent than wet growth.

ACKNOWLEDGEMENTS

I would like to thank the following people, without whom this thesis would not have been possible: my advisor; Steve Rutledge, for excellent guidance and support; my committee members, Jeff Collett and V. N. Bringi; the CSU-CHILL staff - Pat Kennedy, Dave Brunkow, Ken Pattison, and Bob Bowie - for help with operational and data analysis issues before, during, and after STERAO-A; James Dye of NCAR for guidance and insight; Larry Carey -for help with understanding and interpreting the radar and flat plate data, Jesse Ryan - for assistance with the operation and analysis of the flat plates during and after STERAO-A, Paul Hein - for maintaining the computers and analysis software, Kristy Rouault - for help with fiscal issues and office supplies, and other members of the CSU Radar Meteorology group, past and present - for support, company, discussions, ideas, and general assistance; Pierre Laroche and Eric Defer of ONERA for providing and helping analyze the interferometer data; Paul Krehbiel of New Mexico Tech for insight regarding short-duration discharges; Marshall Space Flight Center for providing the NLDN data; Bill Rison of New Mexico Tech for providing flat plate antennas for STERAO-A; Bill Skamarock of NCAR for providing the soundings; Earle Williams of MIT for help with understanding interferometer analysis issues; and Charlie Wilkins for outfitting the mobile flat plate van for operations during STERAO- A.

TABLE OF CONTENTS

Chapter/Section Title	Page
1. INTRODUCTION	**1**
1.1 Background Motivation	1
1.2 Overview of the STERAO-A field project and the case studies	5
1.3 Scientific objectives and organization of the thesis	7
2. DESCRIPTION OF INSTRUMENTATION AND METHODOLOGY	**10**
2.1 CSU-CHILL multiparameter Doppler radar	10
2.1.1 Description of CSU-CHILL radar and measured variables	10
2.1.2 Multiparameter radar data analysis methods	16
2.2 ONERA VHF lightning interferometer	23
2.3 National Lightning Detection Network	26
2.4 Field change meters	27
3. INTERCOMPARISON OF LIGHTNING SENSORS	**37**
3.1 VHF lightning interferometer vs. the National Lightning Detection Network	37
3.1.1 Introductory material	37
3.1.2 Intercomparison of ITF and NLDN data from 10 July 1996	38
3.1.3 Intercomparison of ITF and NLDN data from 12 July 1996	41
3.2 VHF lightning interferometer vs. flat plate antennas	42
3.3 Short-duration flashes in the VHF lightning interferometer data	44
3.4 How the ITF data will be interpreted in this study	49
4. ANALYSIS OF THE 10 JULY 1996 STORM	**64**
4.1 Atmospheric conditions	64
4.2 Overview of storm evolution and major transition	65
4.3 Comparison of lightning and bulk precipitation rates	69
4.4 Identification of bulk precipitation types	75
4.5 Discussion and summary	80

5. ANALYSIS OF THE 12 JULY 1996 STORM 117
5.1 Atmospheric conditions 117
5.2 Overview of storm evolution and major transition 118
5.3 Comparison of lightning and bulk precipitation rates 120
5.4 Identification of bulk precipitation types 126
5.5 Discussion and summary 129

6. DISCUSSION AND CONCLUSIONS 152
6.1 Analysis of possible mechanisms for low CG production in intense storms 152
6.2 Recommendations for future research 159

REFERENCES 162

LIST OF TABLES

Table Caption	Page
2.1 Characteristics of the CSU-CHILL radar during the STERAO-A field project	30
2.2 Overview of algorithm used to calculate rain and hail rates from CSU-CHILL multiparameter radar data.	31
2.3 Hydrometeor identification matrix, based on multiparameter radar data, used in this study to distinguish between bulk precipitation types below the freezing level.	32
2.4 Characteristics of the ONERA VHF lightning interferometer during the STERAO-A field project.	33
2.5 Criteria used by the ITF analysis software to separate and classify flashes.	34
3.1 Square of the correlation coefficient, ρ^2, between one-minute ITF and CHILL FCM flash rates for the 12 July 1996 storm as a function of the filtering distance (from CHILL) applied to the ITF data. Flashes outside this distance are not considered in the ITF flash rate calculations.	54
3.2 Same as Table 3.1 except that ITF flashes lasting less than 1 ms have been excluded from flash rate calculations.	55

LIST OF FIGURES

Figure Caption	Page
1.1 Schematic map of the operational area of STERAO-A. Pictured are the locations of the CSU-CHILL radar (CHL), the VHF interferometer receiving stations (large dots), and the fixed flat plate antennas. The best-resolution lobes of the ITF are marked by the dark solid circles, and the nominal ranges of the fixed flat plates (at CHL and FTM) are marked by the light solid circles. CYS is Cheyenne, Wyoming; ATS is the CSU Atmospheric Science Department in Fort Collins, Colorado; FTM is the Fort Morgan, Colorado, Airport; and DIA is the Denver International Airport.	9
2.1 Schematic representation of the combined elevational and azimuthal receiving station for the ONERA VHF interferometer. The azimuthal-only receiving station is similar in appearance, but lacks the elecation sensor and hence is somewhat shorter.	35
2.2 Schematic illustration of how the two VHF interferometer receiving stations combine to give the three-dimensional location of a VHF source. The combined azimuthal and elevational receiving station, ITF_1, gives an elevation angle, φ_1, and an azimuthal angle, θ_1, to the source. The azimuthal-only station, ITF_2, gives an additional azimuthal angle, θ_2, to the source. The projection of the three-dimensional VHF source onto the horizontal plane, H, gives the two-dimensional location of the source, M(x,y).	36
3.1 Five-minute NLDN and ITF CG rates as a function of time for the 10 July 1996 storm.	56
3.2 Five-minute CG rates as a function of time for the 10 July storm. CGs are split into three categories: those detected and classified by both the ITF and NLDN, those detected and classified by only the ITF, and those detected and classified by only the NLDN.	57
3.3 Same as Figure 3.1 except for the 12 July 1996 storm.	58
3.4 Same as Figure 3.2 except for the 12 July 1996 storm.	59
3.5 One-minute ITF and CHILL FCM total flash rates as a function of time for the 12 July 1996 storm. ITF flashes farther than 35 km from the CHILL radar have been excluded from ITF flash rate calculations.	60

3.6 Normalized ITF flash duration frequency spectra for two different storms: 10 July 1996 and 12 July 1996. The spectra are normalized by dividing the number in each bin by the total number of flashes on the respective day. Note that the abscissa of this plot is logarithmic. 61
3.7 Same as Figure 3.5 except that ITF flashes lasting less than 1 ms have been excluded as well. 62
3.8: Five-minute ITF IC and sub-ms flash rates for 10 July 1996. Sub-ms flashes are defined as flashes lasting less than 1 ms. ICs are IC flashes lasting 1 ms or longer. 63
4.1 Data from the mobile CLASS sounding launched from the Fort Morgan, CO, Airport at 1450 MDT on 10 July 1996. Plotted in skew-T/Log-p format are vertical profiles of temperature, dewpoint, and winds. 85
4.2 a) Horizontal cross-section of radar reflectivity (dBZ) at 0.5 km AGL, for 1629 MDT on 10 July 1996. 86
b) Same as Figure 4.2a except for 1701 MDT. 87
c) Same as Figure 4.2b except for 1731 MDT. 88
d) Same as Figure 4.2c except for 1803 MDT. 89
e) Same as Figure 4.2d except for 1834 MDT. 90
f) Same as Figure 4.2e except for 1900 MDT. 91
g) Same as Figure 4.2f except for 1932 MDT. 92
h) Same as Figure 4.2g except for 2001 MDT. 93
i) Same as Figure 4.2h except for 2030 MDT. 94
4.3 a) Vertical cross-section of radar reflectivity (dBZ) at 45.2° azimuth, for the radar volume beginning at 1932 MDT. Vertical scale is in km AGL; horizontal scale is in km from the radar. 95
b) Same as Figure 4.3a except the plotted field is Doppler velocity (m s^{-1}). Negative velocities are toward the radar, positive are away. 96
4.4 a) Horizontal sweep of radar reflectivity (dBZ) at 3.5° elevation, from the radar volume beginning at 1932 MDT. Distances are in km and azimuthal angles are in degrees. 97
b) Same as Figure 4.4a except for Doppler velocity (m s^{-1}). 98
4.5 Five-minute NLDN CG rates and 5-minute ITF IC rates for the 10 July 1996 storm. Data points are plotted at the start of each 5-minute period. 99
4.6 a) Horizontal cross-section of radar reflectivity (dBZ) at 0.5 km AGL for the 1803 MDT radar volume. Also shown are ground strike locations of all NLDN-detected CG lightning that occurred during the duration of the volume scan. Negative CGs are marked with a minus sign, and positive CGs are marked with a plus sign. 100
b) Same as Figure 4.6a except for the 1809 MDT volume scan. 101

4.7 a) Horizontal cross-section of radar reflectivity (dBZ) at 0.5 km AGL for the 1803 MDT radar volume. Also shown are mean horizontal positions (marked by plus signs) of all ITF-detected IC lightning that occurred during the duration of the volume scan. 102
b) Same as Figure 4.7a except for the 1809 MDT volume scan. Marked by solid lines are the positions of the vertical cross-sections in Figure 4.8 (a-d, respectively). 103
4.8 a) Vertical cross-sections of radar reflectivity (dBZ) at 88 km north of the CHILL radar, for the 1809 MDT volume scan. 104
b) Same as Figure 4.8a except at 75 km north of CHILL. 105
c) Same as Figure 4.8b except at 67 km north of CHILL. 106
d) Same as Figure 4.8c except at 55 km north of CHILL. 107
4.9: Time histories of radar-inferred storm complex total precipitation mass flux (rain + hail) at 0.5 km AGL and 5-minute IC flash rates. Fluxes are plotted at the start of each radar volume, and flash rates are plotted at the start of each 5-minute period. 108
4.10 Time histories of radar-inferred storm complex total rain and hail mass fluxes at 0.5 km AGL. Fluxes are plotted at the start of each radar volume. 109
4.11 Comparison between radar-inferred storm complex total precipitation fluxes at 0.5 km AGL, calculated via the method of the present study and via the method of Carey and Rutledge (1997). 110
4.12 Comparison of radar-inferred volumes of small (< 2 cm) hail below the freezing level, for three different reflectivity gradient filtering thresholds. 111
4.13 Time histories of radar-inferred volume of small, wet hail below the freezing level for the 10 July 1996 storm. 112
4.14 Time histories of radar-inferred volumes of small hail mixed with rain and rain only, below the freezing level. 113
4.15: Time histories of the areal coverage at 0.5 km AGL of small hail only, small hail mixed with rain, and rain only. 114
4.16 a) Vertical cross-section of radar reflectivity (dBZ) along the 50° azimuth for the volume beginning at 2357 MDT. The horizontal scale (distance from the radar) is in km, and the vertical scale (distance AGL) is in km. The arrow denotes the region of probable wet growth. 115
b) Same as Figure 4.16a except for LDR (dB). Note that LDR values below -26 dB are not displayed. 116
5.1 Data from the mobile CLASS sounding launched from the Fort Morgan, CO, Airport at 1356 MDT on 12 July 1996. Plotted in skew-T/Log-p format are vertical profiles of temperature, dewpoint, and winds. 133
5.2 a) Horizontal cross-section of radar reflectivity (dBZ) at 0.5 km AGL, for 1658 MDT on 12 July 1996. 134

b) Same as Figure 5.2a except for 1730 MDT. 135
c) Same as Figure 5.2b except for 1804 MDT. The line denotes the position along which the vertical cross-section in Figure 5.5 is taken. 136
d) Same as Figure 5.2c except for 1832 MDT. 137
e) Same as Figure 5.2d except for 1855 MDT. 138
f) Same as Figure 5.2e except for 1931 MDT. 139
g) Same as Figure 5.2f except for 1959 MDT. 140
h) Same as Figure 5.2g except for 2031 MDT. 141
5.3 Five-minute NLDN CG flash rates for the entire 12 July 1996 storm complex, broken down by polarity. 142
5.4 Five-minute ITF IC flash rates and radar-inferred rain and hail fluxes at 0.5 km AGL for the entire 12 July 1996 storm complex. 143
5.5 Vertical cross-section of radar reflectivity (dBZ) at 11 km west of CHILL for the radar volume beginning at 1804 MDT. 144
5.6 Horizontal cross-section of radar reflectivity (dBZ) at 0.5 km AGL for the radar volume beginning at 1937 MDT. Also plotted are the ground strike locations of NLDN-detected CG lightning that occurred during the duration of the volume scan. Plus signs refer to positive CGs, and minus signs to negative CGs. The lines denote the positions along which the vertical cross-sections in Figures 5.7 (a-b, respectively) are taken. 145
5.7 a) Vertical cross-section of radar reflectivity (dBZ) at 24 km east of CHILL for the radar volume beginning at 1937 MDT. 146
b) Vertical cross-section of radar reflectivity (dBZ) at 56 km east of CHILL for the radar volume beginning at 1937 MDT. 147
5.8 a) Horizontal cross-section of radar reflectivity (dBZ) at 0.5 km AGL for the radar volume beginning at 1741 MDT. Also plotted are the mean horizontal positions of ITF-detected IC lightning that occurred during the volume scan. 148
b) Horizontal cross-section of radar reflectivity (dBZ) at 0.5 km AGL for the radar volume beginning at 1855 MDT. Also plotted are the mean horizontal positions of ITF-detected IC lightning that occurred during the volume scan. 149
5.9 Comparison of radar-inferred areal coverages at 0.5 km AGL of small hail mixed with rain, computed using three different reflectivity gradient thresholds. 150
5.10 Radar-inferred areal coverage of rain at 0.5 km AGL for the 12 July 1996 storm. 151

CHAPTER 1

INTRODUCTION

1.1 Background Motivation

Intense or severe convective storms are sometimes characterized by low production of cloud-to-ground (CG) lightning flashes during all or a portion of their lifetimes (e.g., MacGorman and Nielsen, 1991; Billingsley and Biggerstaff, 1994; Maddox et al., 1997). This anomalous lightning signature can be associated with very high intra-cloud (IC) lightning flash rates, as well as a higher-than-normal percentage of positive CG lightning (Carey and Rutledge, 1997). Thus, it is possible for a storm to produce large hail, strong winds and tornadoes, but have a CG lightning signature similar to that of a non-severe convective cell. Hence, as CG lightning data become more available for the "nowcasting" of severe weather, it is important to document and develop physically based explanations for low CG rates in certain intense storms.

Several hypotheses have been offered to explain this anomalously low production of CGs. One hypothesis invokes the non-inductive charging theory of cloud electrification (NIC). According to NIC, charge is separated through collisions between graupel and ice crystals in the presence of supercooled water. The sign of the charge transferred to the graupel particle depends on the environmental temperature, the liquid water content (LWC), and hydrometeor terminal velocities. For typical values of cloud LWC, however, the sign of the charge transferred to the graupel particle changes at a given temperature,

referred to as the charge-reversal temperature. Takahashi (1978) found this temperature to be approximately -10 °C. Other researchers (e.g., Saunders et al., 1991) have found somewhat different, but still comparable, charge reversal temperatures. At temperatures lower than this, in the upper regions of the thunderstorm, the graupel charge negatively and the ice crystals charge positively. At temperature higher than this, near the base of the cloud, the graupel charge positively and the ice crystals charge negatively. This lower region of net positive charge has been discussed in Williams (1989), and is thought to provoke CG lightning (Clarence and Malan, 1957; Williams et al., 1985; Williams et al., 1989a). However, based on the results of Saunders et al. (1991) and Saunders and Brooks (1992), significant charging should not occur during wet growth regimes, as the rebounding efficiency of collisions goes to zero in such situations. If substantial wet growth is not occurring in these lower regions of the cloud, above the charge-reversal temperature, then the lower positive charge region should not develop as strongly. Hence, CG lightning might be suppressed. Note, however, that the results of Saunders et al. (1991) and Saunders and Brooks (1992) are in contradiction to the results of Takahashi (1978), especially as interpreted by Williams et al. (1991), who found significant charging in regimes of probable wet growth. This conflict has not been resolved yet.

A second hypothesis is that for intense storms with high precipitation rates, the electrical current associated with charged precipitation (precipitation current, J_P) may be large enough to offset charge carried to ground by the CG lightning current (J_L). Results vary widely, but the current state of research suggests that precipitation current (Rust and Moore, 1974; Moore, 1976; Moore and Vonnegut, 1977; Gaskell et al., 1978, Marshall and Winn, 1982; Soula and Chauzy, 1996; Baranski, 1996) may be comparable to CG

lightning current (Livingston and Krider, 1978; Krehbiel, 1981), at least in an average sense. Hence, it may be possible that in certain intense convective storms, the instantaneous precipitation rates become high enough that J_p is large compared to J_L. In this case the precipitation current may remove separated charge quickly enough that CG lightning is less favored.

A final hypothesis is known as the elevated dipole hypothesis (MacGorman and Nielsen, 1991). In this hypothesis, intense updrafts of severe storms loft the negative charge center and the upper positive charge region to greater heights. (See Williams, 1989, for a discussion of the tripole structure of thunderstorms.) Because of the increased distance between the negative charge center and ground, IC lightning should be preferred over CG lightning. In addition, such strong updrafts could enhance charging and hence flash rates. Thus, enhanced IC lightning could neutralize enough charge so that when the cores do descend as the cells decay, CG lightning still is not favored because of lower electric fields due to less space charge.

Before a discussion on how these hypotheses will be examined, some background material on convective storm classification will be reviewed. Convective storms can be classified in terms of three major types: ordinary single cell, multicell, and supercell (e.g., Weisman and Klemp, 1984). Ordinary single-cell storms are characterized by a single updraft in its developing stages, which is destroyed by evaporative cooling due to entrainment of dry air as well as by precipitation loading. The development of a downdraft in response to these processes signals the decay phase of the cell. When the downdraft strikes the ground it spreads out horizontally as a gust front. Should this gust front trigger the development of new cells, then a multicell storm can result. Such a storm

is characterized by the continued decay of old cells and the subsequent development of new cells, typically on a preferred flank. Supercells consist of a single long-lived cell which has a rotating updraft-downdraft couplet. The separation of the updraft and downdraft allows the storm to exist for a considerable period of time, as the updraft and downdraft mutually support one another. The major factors determining whether single cell, multicell, or supercell storms will develop in a given area are the Convective Available Potential Energy (CAPE) and the ambient wind shear (Weisman and Klemp, 1982, 1984).

Additionally, multicell storms may be further subdivided into two types: non-severe and severe, the latter defined according to United States National Weather Service (NWS) criteria as producing large (2 cm in diameter) hail or winds with speeds of 50 knots or more. Severe multicells typically are characterized by strong updrafts which tilt over the downdraft, so that precipitation falls out of the updraft into the downdraft, and thus loading is not as effective at weakening the updraft. The strong updraft allows for the development of large hail.

Up to this point the discussion has focused on storms under the assumption that they remain the same type throughout their lifetimes. However, this need not be the case. During Phase A of the Stratosphere-Troposphere Experiments: Radiation, Aerosols, Ozone (STERAO-A) field project, which will be discussed in the next section, many storms could not be classified as a single type throughout their lifetimes. There was a case where a storm began as a multicellular line, but later became unicellular in character. There were many cases of multicell non-severe storms which became severe at some point in their life cycles. These transitions often were accompanied by major shifts in the

storms' lightning patterns. These included changes in the IC-CG lightning ratio, changes in IC flash rate, changes in CG flash rate, and changes in dominant CG lightning polarity (i.e., positive vs. negative CGs).

Such storms provide an excellent opportunity to examine the hypotheses for the significant reduction of CGs in some intense convective storms. By examining a storm's lightning and microphysical structure before, during, and after a major transition, any changes in these features can be clearly documented. By noting what has changed and what hasn't as the storm undergoes a major evolution, a better understanding of the relationships between storm microphysics and lightning can be obtained. Knowledge of these relationships then can be used to test the aforementioned hypotheses.

In addition, the study of these transitions provides an additional benefit for the "nowcasting" of severe weather. Documentation of any notable changes in lightning patterns during these transitions can assist forecasters in attempts to determine whether a given storm is transitioning from non-severe to severe, or from severe to non-severe.

1.2 Overview of the STERAO-A field project and the case studies

Phase A of the Stratosphere-Troposphere Experiments: Radiation, Aerosols, Ozone (STERAO-A) field project took place during the summer of 1996 over the plains of northeastern Colorado. The purpose of the project was to study trace gas production and transport by deep convection, especially nitrogen fixation by lightning. The project was centered around the CSU-CHILL multiparameter Doppler radar near Greeley. The radar was used to characterize the microphysical and kinematic structure of sampled storms. Also available was the Office National d'Etudes de Recherches Aerospatiales (ONERA)

VHF lightning interferometer (ITF), which maps VHF emissions from lightning in three dimensions. The National Oceanic and Atmospheric Administration (NOAA) WP-3D aircraft had several on-board instruments to make low- to medium-altitude concentration measurements of various trace gases, especially NO_x (NO and NO_2). The WP-3D also had a tail-scanning X-band Doppler radar to characterize the storm-relative wind field via dual-Doppler observations. Instruments on board the University of North Dakota (UND) Citation aircraft made high-altitude trace gas concentration and in situ microphysical measurements of several storms, and often worked in concert with the WP-3D. There was a network of three field change meters (FCM; also know as flat plate antennas) – one mobile, two fixed – to make measurements of total flash rate for storms within the nominal sensor range of 35-40 km. The fixed sites were the CSU-CHILL radar and the Fort Morgan Airport, approximately 75 km ESE of CHILL. The mobile field change meter was operated from a chase van that was deployed from CHILL. Additionally, an electric field mill was stationed at the Fort Morgan Airport. Finally, project participants had access to CG data from the National Lightning Detection Network (NLDN).

Figure 1.1 is a schematic map of the area in which the STERAO-A project took place. Included are the positions of the CHILL radar which had a maximum range of 150 km during STERAO-A, the positions of the ITF receiving stations and the ITF's two best-resolution lobes, and the positions of the fixed FCMs along with range rings.

The presence of data from both the CHILL radar and the ITF provided a unique data set for which to study the relationships between convective storm microphysics and associated lightning. This research utilized data from the CHILL radar, the ONERA ITF, the NLDN, and the flat plates; and focused on two case studies of deep convective storms,

10 and 12 July 1996. (All dates and times are in terms of the local time, Mountain Daylight Time.)

The 10 July 1996 storm began as a multicellular line but toward the end of its long lifetime it became unicellular in nature, with characteristics that are often displayed by supercells, such as mid-level rotation and a Weak Echo Region (WER). Throughout the storm's lifetime, CG rates were extremely low, peaking at only 9 CGs in a 5-minute period, but usually varying between 0 and 2 CGs per 5-minute period. The IC flash rate for this storm was relatively high, around 20 ICs per minute throughout much of the storm's lifetime. The radar-inferred precipitation fluxes, especially the hail flux, trended the IC rates well, but sometimes precipitation peaks lagged the IC peaks by up to several minutes. IC flashes peaked near 50 per minute during the storm's quasi-supercellular stage. During this stage there were almost no CGs.

The storm of 12 July 1996 was a multicell storm which became severe before full volume radar scanning was initiated. This storm reverted to non-severe status during the course of detailed observations. Before this transition, radar-inferred hail fluxes were quite high, but afterward, hail fluxes were small. Before the transition, both negative and positive CG rates were relatively low, usually well under 5 per 5-minute period. Positive CGs made up a significant fraction of this small CG population. After the transition, however, positive CG rates remained low but negative CG rates exploded, varying between 10 and 25 per 5-minute period for over an hour.

1.3 Scientific objectives and organization of the thesis

The primary objective of this research is to analyze a unique data set consisiting of concurrent measurements from the CSU-CHILL radar and the ONERA VHF interferometer, and during the course of this analysis to examine the validity of various hypotheses offered to explain the low production of CGs in some intense convective storms. To review, these hypotheses are: significant wet growth of graupel and hail that would suppress the development of a lower positive charge region (which normally could act to provoke CG lightning), removal of charge by large precipitation currents relative to lightning currents, and the elevated dipole mechanism acting in concert with enhanced IC flash rates. Offshoots of this objective are the presentation of detailed case studies of major transitions in convective storms and the documentation of additional cases of low-CG intense convective storms. This information could have potential use in the "nowcasting" of severe weather.

A secondary objective is to provide an intercomparison of the data from the various lightning sensors; in particular, to provide verification for the ITF flash rates.

This thesis is organized into six chapters. After this introductory chapter, Chapter 2 discusses the various sensors used in this research, and the methodology used to interpret their data. Chapter 3 presents results from an intercomparison of the various lightning sensors. The results are interpreted in order to determine a strategy for how best to include the ITF data in the research. Chapter 4 presents the first case study, the storm of 10 July 1996. Chapter 5 presents the second case study, the storm of 12 July 1996. Chapter 6 presents conclusions and recommendations for future research.

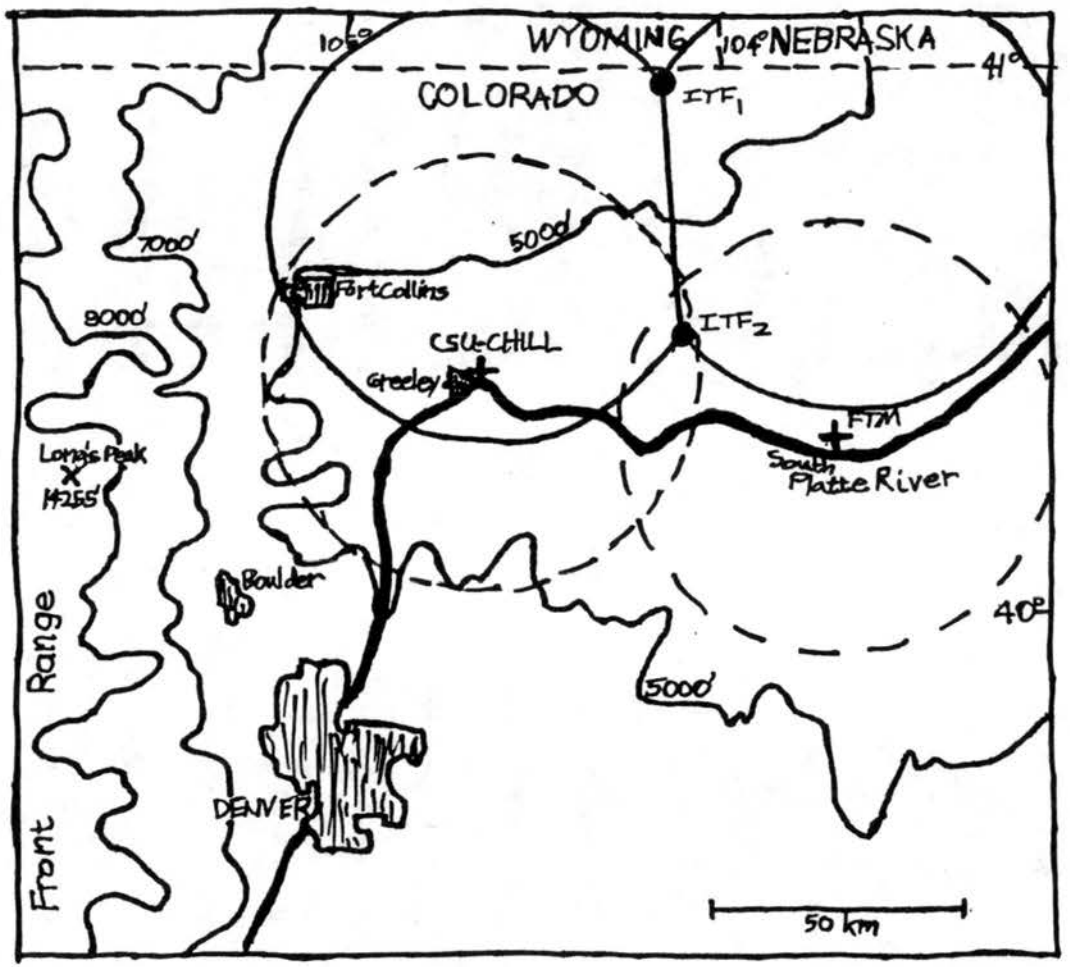

Figure 1.1: Schematic map of the operational area of STERAO-A. Pictured are the locations of the CSU-CHILL radar, the VHF interferometer receiving stations (large dots), and the fixed flat plate antennas (crosses). The best-resolution lobes of the ITF are marked by the dark solid circles, and the nominal ranges of the fixed flat plates (at CHILL and Fort Morgan) are marked by the dashed circles. FTM is the Fort Morgan Airport.

CHAPTER 2

DESCRIPTION OF INSTRUMENTATION AND METHDOLOGY

The purpose of this chapter is to describe the instruments used in this research and to review the methodology used in the analysis of the data from these sensors. The four sensors that will be covered are the CSU-CHILL radar, the Office National d'Etudes de Recherches Aerospatiales (ONERA) VHF lightning interferometer (ITF), the National Lightning Detection Network (NLDN), and flat plate antennas (FCM).

2.1 CSU-CHILL multiparameter Doppler radar

2.1.1 Description of CSU-CHILL radar and measured variables

Table 2.1 lists the operational characteristics of the CSU-CHILL radar. It is a dual linearly polarized S-band Doppler radar. The radar alternately transmits horizontally polarized and vertically polarized microwave radiation, and simultaneously detects both polarization states via dual receivers.

For the STERAO-A project (including the two case studies to be discussed in Chapters 4 and 5) a plan-position indicator (PPI) sector scanning strategy was used. Full volume coverage of storms with the preservation of good temporal resolution (~ 6 minutes or less) was the goal. Individual elevation sweeps typically were separated by 1° or less. Sector boundaries were set in order to contain most or all of the echo exceeding 30 dBZ. At times, however, the size or proximity of the storm forced certain compromises in the

scanning strategy in order to maintain good temporal resolution, including the following: decreased elevational resolution, particularly at high elevation angles; not scanning to the top of the storm echo (i.e., "topping" the storm); and more restrictive azimuthal boundaries so that the storm was not completely contained within the sector. Additionally, during the storm of 12 July 1996, two different and conflicting scanning strategies were alternately employed: the one described above, and a second one associated with another field project occurring at the same time. The latter field project was concerned mainly with sampling low elevation angles with PPI sectors, but also employed range-height indicator (RHI) scans. The STERAO-A scanning strategy had priority, but unfortunately (for the purposes of this study) during 12 July 1996 the second scanning strategy was employed at times. This decreased the temporal resolution of the full-volume sector scans around these times.

The multiparameter variables measured by the radar included horizontal reflectivity (Z_h), radial velocity (V_r), differential reflectivity (Z_{dr}), linear depolarization ratio (LDR), correlation coefficient at zero lag (ρ_{hv}), and differential phase (Ψ_{dp}). These variables give information on the size, shape, orientation, thermodynamic phase, and radial velocity of hydrometeors in a bulk sense. Through the use of these variables, it is possible to map regions of hail, rain, and mixed-phase precipitation, as well as to distinguish large ($\geq$ 2 cm diameter) hail from other hydrometeor types and to determine rain and hail rates with good accuracy (e.g., Doviak and Zrnic, 1993; Balakrishnan and Zrnic, 1990a,b; Zrnic et al., 1993).

A brief discussion of the radar variables used in this study is necessary in order to understand how they can be used to distinguish between precipitation types and to

determine precipitation amounts. This discussion is in large part adapted from Carey and Rutledge (1996, 1997).

Horizontal reflectivity measures the amount of power backscattered by individual radar volumes. For scattering by spherical targets with diameters much smaller than the wavelength of the incident radar beam (i.e., the Rayleigh scattering regime; $r \leq 0.07\lambda$, where λ is the wavelength of the radar), reflectivity depends on the sixth power of the hydrometeor diameter. Hence, this reflectivity factor is most sensitive to the largest particles.

The radial velocity variable measures the speed of the targets, but only along the radial direction (i.e., away from or toward the radar). This variable is determined through standard Doppler radar techniques. (See Doviak and Zrnic, 1993, for a review of these.)

Differential reflectivity measures the reflectivity-weighted mean axis ratio of hydrometeors. It is defined, in decibels (dB), as

$$Z_{dr} = Z_h - Z_v , \tag{2.1}$$

where Z_v is the reflectivity from the vertically polarized wave. Because Z_{dr} is reflectivity-weighted, it is also sensitive to the dielectric factor and the size of the scattering hydrometeor. For example, water particles have a higher dielectric constant than ice particles, so a raindrop with the same size and axis ratio as a graupel particle will have a higher differential reflectivity than the graupel particle. Raindrops with diameters greater than 1 mm are deformed into oblate spheroids by aerodynamic drag as they fall. Furthermore, they tend to fall with their maximum dimension oriented horizontally (Pruppacher and Beard, 1970). Thus, $Z_h > Z_v$ and Z_{dr} is positive in rain. Also, Z_{dr} increases with drop size. Hail tends to be spherical in shape, or if it is not, it tends to

tumble as it falls (Aydin et al., 1984). Thus, regions of hail tend to have a differential reflectivity near zero. Rain and hail mixtures can also have Z_{dr} near zero provided the hail is large enough to dominate the reflectivity. It is possible to have negative Z_{dr} in regions where the hail is prolate in shape (i.e., the vertical axis is longer than the horizontal axis – Zrnic et al., 1993; Hubbert et al., 1997). Also, for S-band radars like the CHILL, non-Rayleigh scattering by large, wet, oblate hail can drive differential reflectivity negative (Aydin and Zhao, 1990). Differential attenuation also is capable of driving Z_{dr} negative (Bringi et al., 1990).

Linear depolarization ratio measures the ratio of the cross-polar signal power to the co-polar power. It is defined as

$$LDR = 10\log\left(\mathbf{Z}_{vh}/\mathbf{Z}_{hh}\right) \text{ [dB]}, \tag{2.2}$$

where **Z**, the reflectivity factor, has units of $mm^6\ m^{-3}$, h and v represent the horizontal and vertical polarizations, respectively, and the first subscript stands for the backscattered electric field and the second stands for the incident electric field. If the vertically (horizontally) polarized incident electric field is aligned with either the major or minor axis of an oblate target, then there can be no horizontally (vertically) polarized backscattered field. Thus, for such a situation, LDR approaches negative infinity. However, the CHILL radar's integrated cross-polarization isolation limits the lowest value of LDR to approximately -35 dB (Mueller et al., 1995). In thunderstorms, most oblate hydrometeors tend to wobble as they fall, so there is a distribution of canting angles which raises LDR. Irregularly shaped hydrometeors (i.e., hail with lobes) increases LDR as well. Also, LDR increases as precipitation particles become more oblate (provided they are canted) or their

dielectric factor increases (Frost et al., 1991). For rain, canting is generally negligible, so LDR varies between -27 dB and -30 dB. Low-density graupel has a smaller dielectric factor than rain, so it has a lower LDR than rain, typically less than -30 dB (Frost et al., 1991). Wet aggregates in the radar bright band exhibit very high depolarization. Depolarization in hail also can be very significant because hailstones often exhibit complex motions (e.g., tumbling) as they fall (Knight and Knight, 1970). Tumbling *wet* hailstones can exhibit LDR values around -20 dB, with maximum values approaching -10 dB (Aydin and Zhao, 1990).

Differential phase is defined as

$$\Psi_{dp} = \phi_{dp} + \delta \,, \tag{2.3}$$

where ϕ_{dp} is the differential propagation phase, and δ is the backscatter differential phase, both in degrees. The differential propagation phase is defined as $\phi_{dp} = \phi_{hh} - \phi_{vv}$, where ϕ_{hh} is the cumulative phase shift for horizontally transmitted and received polarized radiation during the round trip from radar to resolution volume and back, and ϕ_{vv} is the same for vertically polarized electromagnetic waves. Differential propagation phase results from propagation through an anisotropic medium such as rain. Backscatter differential phase results from backscatter in a radar resolution volume containing particles large enough so that they scatter in the non-Rayleigh regime. At S-band, hail is often large enough to cause such non-Rayleigh scattering (especially when wet), so δ must be separated from ϕ_{dp} through the use of filtering techniques. This study used the filtering technique of Hubbert et al. (1993).

The specific differential phase, K_{dp}, was used in this research. It is calculated from the range derivative of ϕ_{dp}. After filtering Ψ_{dp} to remove the contribution from δ, K_{dp} can be

estimated using finite difference techniques. Given measurements of ϕ_{dp} at two different ranges, r_1 and r_2, K_{dp} can be estimated as

$$K_{dp} = \frac{1}{2}\frac{d\phi_{dp}}{dr} \approx \frac{\phi_{dp}(r_2) - \phi_{dp}(r_1)}{2(r_2 - r_1)} \ [^\circ \text{ km}^{-1}]. \tag{2.4}$$

Specific differential phase is not sensitive to isotropic scatterers, such as quasi-spherical or tumbling hail. It is, however, extremely sensitive to anisotropic scatterers such as oblate raindrops. Thus, in a mixed phase environment, K_{dp} will be sensitive only to the rain portion. From theoretical considerations, Jameson (1985) showed that specific differential phase is linearly related to the liquid water content of precipitation, which allows for accurate rainfall measurements, especially in heavy rain ($\geq$ 60 mm h^{-1}; Chandrasekar et al., 1990). Because K_{dp} is basically insensitive to hail, this variable provides accurate rain rate estimates even in mixed-phase environments. Specific differential phase can be used in conjunction with Z_h to separate the contributions of rain and hail to total reflectivity, and thus allow for estimates of the hail rate (hail mixing ratios) in addition to the rain rate (rain mixing ratios - Balakrishnan and Zrnic, 1990b; Carey and Rutledge, 1997).

The correlation coefficient at zero lag between the horizontally and vertically polarized backscattered radiation depends on the distributions of sizes, shapes, and canting angles of the hydrometeors, as well as on the phase shift upon backscatter. The correlation coefficient is high ($\geq$ 0.97) in rain. It decreases in mixed-phase hydrometeors because the size, shape, and canting angle distributions, as well as the differential backscatter phase, broaden or increase as the ice particle size increases. Correlation decreases are maximum if the reflectivity factors from the ice and water hydrometeors are similar. If either hydrometeor dominates the reflectivity, then the correlation coefficient is weighted toward

that hydrometeor type. Several researchers (Balakrishnan and Zrnic, 1990a, Kennedy and Rutledge, 1995; Carey and Rutledge, 1997) have used the correlation coefficient to infer regions of large (≥2 cm) hail and/or to distinguish between large and small (< 2 cm) hail.

2.1.2 Multiparameter radar data analysis methods

CSU-CHILL radar data were edited using the Research Data Support System (RDSS) software developed at the National Center for Atmospheric Research (NCAR; Oye and Carbone, 1981). Most ground clutter and unwanted clear air echo (including anomalous propagation) were removed by thresholding on Z_h (removing data with $Z_h < 0$ dBZ) and ρ_{hv} (removing data with $\rho_{hv} < 0.7$). The threshold value for horizontal reflectivity does not impact any of the precipitation measurements, since according to the reflectivity-rain rate relationship (Jones, 1955) used for light rain in this study, it corresponds to a rain rate much less than the 1 mm h^{-1} threshold used in the precipitation analyses, to be discussed later in this section. The threshold value for the correlation coefficient is well below any value seen in real precipitation data (e.g., Carey and Rutledge, 1997), so it too will not impact the analysis in a negative fashion. Additional clutter and clear air echo were removed manually. All radial velocity folds were corrected using RDSS. Differential phase was filtered using the technique of Hubbert et al. (1993), as mentioned previously. This filter attenuates gate-to-gate fluctuations while preserving physically meaningful trends. Specific differential phase was then calculated by the finite differencing approximation in Eq. 2.4.

All variables were interpolated to a Cartesian grid using the REORDER software package, which also was developed at NCAR. The gridding scheme used a Cressman

filter (Cressman, 1959), with a variable radius of influence. For the filtering process, azimuthal spacing was assumed to be 1°, the half-power width provided by the CHILL antenna. Elevational spacing was set at 1° as well, because most elevation sweeps were spaced 1° or less apart. However, during part of the 12 July 1996 storm's lifetime, when it was closest to the radar, high-elevation sweeps were spaced greater than 1° apart. For these volumes, the elevational spacing in the gridding routine was set at 1.5°. Grid resolution for both storms was set at 1.0 km in both horizontal directions and 0.5 km in the vertical direction. However, the grid resolution should not impact the analysis to any depth, since the variable radius of influence for the Cressman filter takes into account effects of beam widening with distance, and is the major factor in determining the interpolated data values. The choice of grid resolution merely affects how those interpolated values are averaged and distributed.

Storms were gridded so as to include, as best as possible, all echo of 10 dBZ and greater from the cells of interest. After reviewing all of the radar volumes for each case study, cells which did not seem related to the main storm were removed before gridding the data if they couldn't be excluded through choice of grid geometry. During the 10 July storm, the radar volume scans sometimes did not extend far enough in the azimuthal direction to include related cells, but were opened up at a later time to include these cells. During the 12 July storm, some cells were far from the main storm at one time, but later merged with the main storm. Unfortunately, including these cells in the grid when they were distant was not possible because of computer resource limitations, but they were included later when they were closer. This artificial exclusion of cells from both storms

will have an effect on the radar data analysis, in particular the precipitation analyses. This will be taken into consideration when these data are interpreted in Chapters 4 and 5.

The multiparameter variables Z_{dr}, LDR, and ρ_{hv} are often corrupted in areas of strong reflectivity gradients because of the effect of mismatched sidelobe patterns. Herzegh and Carbone (1984) found that when the main beam sampled a region of weak reflectivity in the vicinity of a high reflectivity gradient, measurements of differential reflectivity can be dominated by large sidelobe contributions from a more reflective region. A typical method of dealing with this problem is to filter out possibly bad Z_{dr} data by thresholding on azimuthal and elevational reflectivity gradients. (Radial gradients do not contribute to this problem.) Often these thresholds are range-dependent, becoming more restrictive at greater ranges. In the case of Carey and Rutledge (1996), these thresholds were set by one-dimensional calculations of Z_{dr} bias using CSU-CHILL antenna patterns and horizontal reflectivity profiles as input. Unfortunately, such thresholding can often remove good data along with the corrupted data, since a given threshold does not always hold true throughout the data. That is, the actual reflectivity gradient threshold which signals the onset of data corruption by sidelobe contributions frequently varies throughout the data (L. Carey, private communication, 1997). Thus, a single filtering threshold, even a range-dependent one, is unsatisfactory.

The approach adopted in this work was not to perform this thresholding during the editing stages of data analysis. Instead, the unthresholded data were gridded, and any analysis software which use Z_{dr}, LDR, and/or ρ_{hv} first calculated the local reflectivity gradient in Cartesian space. Then, based on a gradient threshold, a decision was made to include or exclude the particular data from the analysis. In this manner, sensitivity tests

with different thresholds could be performed more easily than the previous method. Calculating the reflectivity gradient in Cartesian space is not strictly correct, however, as the natural coordinates of the radar are spherical, and gradients in spherical coordinate space are what cause the sidelobe contamination problem. A more rigorous approach would be to calculate the gradients in spherical coordinates before gridding the data, perhaps creating a separate data field for reflectivity gradient which then can be gridded along with the other data for easy comparison and sensitivity testing. This approach will be explored in future work.

In this thesis there are two objectives focused on the radar data analysis: 1) calculate near-surface rain and hail rates, and thus make estimates of the storm-total mass flux for each precipitation type, and 2) distinguish between regions of different hydrometeor types in a bulk sense.

Rain and hail rates are calculated through the following algorithm, which is summarized in Table 2.2. If the specific differential phase at a grid point is above the noise level, 0.25 $^\circ$ km^{-1}, then it is used to calculate the rain rate at that point following the method of Sachidananda and Zrnic (1987). If $K_{dp} < 0.25\ ^\circ$ km^{-1}, then a reflectivity-rain rate relationship (commonly known as a Z-R relationship) from Jones (1955) is used to calculate the rain rate. If this rain rate is between 1 and 20 mm h^{-1}, then this rain rate is used in the flux calculations described below. If the Z-R relationship gives a rain rate higher than 20 mm h^{-1}, then it is assumed that the reflectivity is almost entirely due to hail ($K_{dp} < 0.25\ ^\circ$ km^{-1}), and no rain rate is calculated at the grid point. Differential reflectivity also could be used to assess the possibility of hail contamination (Golestani et al., 1989),

but such analysis would be subject to possible errors due reflectivity gradients, as well as other problems which will be discussed later.

The hail rate is calculated by first using K_{dp} to determine the reflectivity factor (in mm^6 m^{-3}) due to rain at a grid point by substituting the K_{dp}-R relationship from Sachidananda and Zrnic (1987) into the Z-R relationship from Jones (1955), then subtracting this rain reflectivity factor from the horizontal reflectivity factor. The difference is the reflectivity factor due to hail, which is then input into the hail reflectivity-hail rate relationship of Carey and Rutledge (1997), which is based on the Cheng and English (1983) hail size distribution, to determine hail rate in mm h^{-1} liquid equivalent. However, if Z_{hail} is not within 7 dB of Z_{rain}, then the hail rate is assumed negligible, after Balakrishnan and Zrnic (1990b). Note that this method assumes Rayleigh scattering by hail, which may not be valid for S-band radars like the CHILL, especially in large hail.

There are some important sources of error in these radar-derived precipitation rates. Differential phase provides superior estimates of rain rate, especially at high rain rates (> 60 mm h^{-1}), but is still subject to errors on the order of 10-20% based on raindrop size distribution variation and radar estimation errors alone (Chandrasekar et al., 1990). Radar reflectivity-rain rate relationships provide comparable errors, but only when rain rates are low (< 20 mm h^{-1}) - otherwise they are much larger (Chandrasekar et al., 1990). Thus, 10-20% serves as a lower bound for errors in rainfall estimates, with an upper bound around 30-40% for those times when assumptions are grossly violated. These errors will affect rain rate calculations as well as the hail rate calculations. In addition, hail rate calculations are subject to further errors. After the initial rain rate calculation, the computation of reflectivity factor due to rain is subject to errors on the order of a few

dBZ (Doviak and Zrnic, 1993). The choice of the Cheng and English (1983) hailstone size distribution may not be valid at any specific time during hailfall, and furthermore as mentioned above the assumption of Rayleigh scattering for hail is not always valid either, especially for large hail. Hail rate is inherently difficult to measure properly via in situ methods, so it is difficult to accurately quantify the magnitude of the error associated with these radar-inferred hail rates. However, estimates of error magnitudes on the order of 50% or more probably are not unreasonable, especially in regions where the assumptions about hail size distribution and Rayleigh scattering are not valid. For example, the given algorithm could significantly overestimate hail rate during those times that hail reflectivity is caused mostly by a few large hailstones, rather than the broader distribution predicted by Cheng and English (1983).

Precipitation fluxes are computed by summing all the precipitation rates over the whole horizontal grid at a specific vertical level (usually the lowest level – 0.5 km above ground level, or AGL – in this case). Fluxes are calculated for the entire storm complex, not individual cells. While a cell-by-cell precipitation analysis may be preferable, in practice it would be difficult to do properly due to the possibility of the choice of analysis region geometry improperly influencing results. That is, it is often difficult to clearly distinguish between two or more cells in multicellular convection, especially on the outskirts of cores and when cores are merging or splitting. In these situations it is obvious that analysis geometry could play a major role in precipitation flux computations, making the analysis results more an artifact of the geometry than real precipitation rates. Though the possibility of quantitative cell-by-cell analysis is lost, computing fluxes for the entire storm

complex removes this potentially large source of error. However, qualitative cell-by-cell analysis of radar reflectivity structure and lightning will be performed.

These precipitation analyses are similar to the methods employed by Carey and Rutledge (1997). However, there are some differences. Carey and Rutledge (1997) split the rain rate calculations into three parts, one for light rain ($1 \leq R \leq 20$ mm h^{-1}), one for moderate rain ($20 < R < 60$ mm h^{-1}), and one for heavy rain ($R \geq 60$ mm h^{-1}). For light rain they used the Z-R relationship of Jones (1955), and for heavy rain they used the R-K_{dp} relationship of Sachidananda and Zrnic (1987), but for moderate rain they used a reflectivity-differential reflectivity relationship, which is also from Sachidananda and Zrnic (1987). However, this relationship can be prone to hail contamination, so they used a Z_{dr} correction method based on the results of Golestani et al. (1989) when the probability of hail contamination was deemed high. This method was tested on the data for the 10 July storm. The results will be discussed in Chapter 4, but it appears that the flux calculation method of Carey and Rutledge (1997) still may be prone to hail contamination despite the correction methods, at least for the 10 July storm.

The precipitation calculation method employed in this thesis avoids this hail contamination problem by not using differential reflectivity in any way. It is especially desirable to use only K_{dp} and Z_h for the precipitation calculations for 10 July, as this storm was at a very long range from the radar. At long ranges the other multiparameter variables are more easily susceptible to sidelobe contamination, and thus are less useful.

Table 2.3 lists the multiparameter variable matrix employed in order to distinguish between different bulk hydrometeor species. This study employed Z_h, Z_{dr}, LDR, K_{dp}, and ρ_{hv} to determine regions of large hail, small hail, large hail mixed with rain, small hail

mixed with rain, and rain only. This matrix is identical to the one used by Carey and Rutledge (1997). The matrix itself, which is applicable only when the environmental temperature is at or above freezing (i.e., near the surface), is a modified form of the one proposed by Doviak and Zrnic (1993). Carey and Rutledge (1997) adjusted these values in order to incorporate more recent modeling and observational results, and to maximize agreement with surface reports of precipitation type and size. Note that in this study the main concern is to distinguish between large and small hail, whether they are mixed with rain or not. Note that multiparameter radar measurements are not unique, in that more than one hydrometeor mix could give the same set of multiparameter radar measurements. Thus, this matrix is only valid as long as its assumptions are valid, and when they are not, large errors (which are difficult to quantify) could result. Thus, this matrix is best used to infer the main hydrometeor types present, and to gain a sense of the basic trends occurring.

2.2. ONERA VHF lightning interferometer

This discussion of the ITF is adapted from Mazur et al. (1997), Laroche et al. (1994), and private communications between the author and ONERA researchers, notably E. Defer and Dr. P. Laroche. The ITF uses interferometric techniques to map VHF emissions from lightning in three dimensions.

Several researchers (e.g., Warwick et al., 1979; Richard and Auffray, 1985; Rhodes et al., 1994) have used interferometric lightning mapping in the past with good success. In radio interferometry, the difference in arrival times of electromagnetic waves at two different antennas is translated into a differential phase, which can then be used to

calculate the angle to the radiation source. Through the use of several antenna pairs, the source can be located in three-dimensional space. The baselines connecting the antenna pairs are measured in wavelengths and half-wavelengths in order to resolve ambiguities in the arrival angle.

The ONERA ITF system itself consists of two main receiving stations. One station consists of two separate antenna sets – the elevation sensor, which measures the elevation angle of the sources; and the azimuthal sensor to determine the azimuthal direction to the source. The second receiving station senses only azimuthal information. Each antenna set consists of circular, vertically polarized electric dipole arrays. The operational characteristics of the ONERA ITF are listed in Table 2.4. Figure 2.1 shows a schematic of the combined azimuth and elevation receiving station. The azimuth-only receiving station is similar in appearance, though it is shorter and lacks the elevation sensor. Figure 2.2 demonstrates how the two stations combine to give reconstruction of a VHF source in three-dimensions.

During the STERAO-A project, the two receiving stations were separated by a baseline approximately 40 km in length, oriented roughly northwest to southeast. (The southernmost receiving station was the azimuth-only sensor.) A spatial resolution of 1-2 km is obtained in the two lobes (east and west) whose boundaries are defined by a distance of approximately 50 km off the baseline. (See Figure 1.1 for a schematic representation of the ITF lobes during STERAO-A.) The ITF cannot unambiguously resolve the positions of VHF sources along or near the baseline, so the best ITF cases occurred when storms were situated within one of the high-resolution lobes.

The three basic types of discharges identified by the ITF are the recoil streamer, the negative leader, and the spider discharge. See Uman (1987) for a detailed review of these types of discharges. Recoil streamers and spider discharges generally are associated with intra-cloud (IC) lightning, whereas negative leaders are associated with cloud-to-ground (CG) lightning. It is important to note that these discharges do not exhaust the list of possible lightning discharges, only those that emit significant VHF radiation within the ITF's band (110-118 MHz). In particular, events involving positive breakdown (e.g., positive leaders associated with positive CGs) do not emit much VHF radiation, nor do return strokes associated with CG lightning. (They are lower frequency emitters.)

The ITF's elevational resolution is set to optimize the resolution of IC lightning data. At low elevation angles (i.e., less than 8°), the resolution degrades from the value listed in Table 2.4. Thus, the ITF does not resolve negative leader processes associated with CG lightning as well as say, recoil streamer processes associated with IC lightning. Additionally, after analysis of the ITF data from STERAO-A, it was found that the elevational resolution of the sensor was less than the value expected based on the results of past field projects involving the ITF (P. Laroche, private communication, 1997). Thus, the true elevational resolution of the ITF was coarser than the 0.5° value listed in Table 2.4. This has an impact on the mapping of both IC and CG lightning, but it will affect the resolution of CG data the most since the low-elevation resolution is by nature more coarse.

During post-processing of the data using the Analyse software developed by ONERA, flashes were identified and classified based on the criteria listed in Table 2.5. These criteria are based on current knowledge of the various VHF-emitting lightning discharge

processes (P. Laroche, private communication, 1997). The criteria govern how the software groups individual localizations (i.e., single VHF sources) into VHF radiation bursts, and how it groups these bursts into separate flashes. The software distinguishes between IC and CG lightning on the basis of an altitude threshold on negative leader processes. Related negative leaders occurring below a given altitude, set by observations from previous field experiments with the interferometer, are classified as CG flashes. Above this altitude they would comprise an IC flash. It is important to note that spider discharges associated with ICs often resemble negative leaders associated with CGs. Thus, a group of spider discharges occurring below the threshold altitude could be incorrectly classified as a CG flash. Thus, the known elevational resolution problems with the ITF during STERAO-A could have profound impacts on the proper classification of IC and CG lightning. This possibility will be explored in Chapter 3.

2.3 National Lightning Detection Network

The NLDN is comprised of a network of magnetic direction finder (DF) sensors and time-of-arrival (TOA) sensors that spans the contiguous United States. The purpose of the network is to accurately locate, in time and space, the ground strike locations of cloud-to-ground (CG) lightning flashes. The network also gives information about the multiplicity (i.e., number of return strokes) and approximate strength of each flash. This strength estimate can be converted to an estimate of peak current through the following relation (Orville, 1991):

$$I_{peak} = 0.19 \bullet I_{LLP} + 2.3, \tag{2.5}$$

where I_{LLP} is the signal strength in Lightning Location and Protection (LLP) units, and I_{peak} is the peak flash current (kA).

Recently, the NLDN was upgraded to its current combination of DF and TOA technology (Cummins et al., 1996). This upgrade was reported by Cummins et al. (1996) to have improved detection efficiency in northeastern Colorado to approximately 90% or more, with a median location accuracy of 0.5 km.

An unexpected result of this upgrade is the inclusion of a previously undetected population of weak positive flashes. These discharges may not be true positive CGs; instead, many could be intra-cloud (IC) discharges which are being falsely identified as positive CGs. It has been suggested that some detected positive discharges with peak currents under 7 kA may be IC discharges (P. Krehbiel, private communication, 1997). However, no positive CGs with peak currents under this threshold were observed in any of the NLDN data for the storms of 10 and 12 July. Therefore, for the purposes of this study, all detected NLDN CGs were considered to be true CG events.

2.4 Field change meters

During the STERAO-A field project, a network of three flat plate antennas, or FCMs, was maintained. Two were located at fixed sites, and one was mobile. The FCMs were essentially identical to the unit used by Carey and Rutledge (1996, 1997). Therefore, the following discussion is adapted from those papers.

The purpose of the FCM is to measure the electrostatic field change associated with both IC and CG lightning (Uman, 1987). Thus, the total flash rate of storms can be estimated with these sensors. In this study, a FCM consisted of a disk-shaped conductor

with its long axis parallel to the ground. The disk was mounted on a stand with its accompanying electronics, and then inverted toward the ground to minimize precipitation contamination. Any change in the ambient electrostatic field was accompanied by a change in the voltage difference across the output. The time constant of the resistor-capacitor network was 30 ms for the mobile FCM, and 25 ms for the fixed FCMs. These time constants are long enough to reproduce the field changes by most IC and CG lightning, yet short enough to bring the output voltage back to zero between flashes. Voltage and time data were sampled at approximately 1 kHz. These FCMs were not calibrated, so voltage data could not be used to estimate electrostatic field changes, though signal strengths could be inferred in a relative sense.

The FCMs have a detection range of approximately 35-40 km (B. Rison, private communication, 1997) at the most sensitive gain setting (the only gain setting used during almost all project days, including 12 July). However, the detection efficiency of the instruments is not well known, but probably is a function of signal strength and range to flash. Also, the FCMs do not resolve direction or range to the flash, so it was important to ensure that only one storm was in range at a time, to avoid ambiguity in flash rate estimates for a single storm.

The FCM data were post-processed using an equally weighted running mean filter designed to eliminate a known source of 60 Hz noise. Lightning flashes were then counted in the data by comparing signal amplitudes to the noise amplitude. The signal-to-noise ratio threshold for counting a particular signal as a flash was set by using the flash-counting algorithm on data from fair-weather days (i.e., days when no storms were in range), and determining an SNR ratio that was as low as possible, but would not be

susceptible to noise-induced false signals. Return strokes were treated by requiring 500 ms to pass before the next signal could be counted as a flash.

Because of the unknown detection efficiency and the nature of the flash-counting algorithm, the FCMs probably cannot be used to estimate the total flash rate very accurately. However, they can be used to examine trends in flash rates with reasonable confidence, as in Carey and Rutledge (1996, 1997). However, any trends in the data need to be analyzed with caution, as due to the limited range of the instrument and the fact that the detection efficiency itself is probably range-dependent, such trends may reflect storms moving into and out of range, and not necessarily any true changes in the total flash rate.

FCM data wre obtained for part of the 12 July 1996 storm's lifetime. Unfortunately, no FCM data were obtained for the 10 July storm. The 12 July FCM data will be utilized in Chapter 3 in an intercomparison with the ITF. They will not be used in the case studies. The reason for this is because the data for this day generally reflect the influence of the movement of the storm into and out of range, and therefore not real trends in storm flash rate. Also, the FCM appears to detect far fewer flashes than the ITF, as will be shown in Chapter 3.

CSU-CHILL radar characteristic	Value during STERAO-A
Wavelength (cm)	11
Polarization	Linear; H and V
Antenna diameter (m)	8.5
3 dB beamwidth (°)	1.0
1st sidelobe level (dB)	< -27
Integrated cross-polarization isolation (dB)	< -32
Peak power (kW)	800
(Pulse length)/2 (h/2, m)	150
Pulse repetition frequency (Hz)	1000
Pulse per integration	128
Receiver noise power (dBm)	-115
Maximum Range (km)	150

Table 2.1: Characteristics of the CSU-CHILL radar during the STERAO-A field project

Overview of precipitation rate calculations

If $K_{dp} \geq 0.25\ ^\circ\ km^{-1}$: $R(K_{dp}) = 40.683 \bullet (K_{dp})^{0.866}$	(Sachidananda and Zrnic, 1987)
If $K_{dp} < 0.25\ ^\circ\ km^{-1}$ and $1\ mm\ h^{-1} < R(Z_h) < 20\ mm\ h^{-1}$: $Z_h = 486 \bullet R(Z_h)^{1.37}$	(Jones, 1955)
Hail ($mm\ h^{-1}$ liquid equivalent): $H\left(K_{dp}, Z_{hail}\right) = \frac{88.0}{\exp\left[5.38 \times 10^{-6} Z_{hail} \left\{K_{dp}\right\}^{-0.297}\right]}$	(Carey and Rutledge, 1997)

Table 2.2: Overview of algorithm used to calculate rain and hail rates from CSU-CHILL multiparameter radar data.

Hydrometeor type ($T \geq 0$ °C)	Z_h (dBZ)	Z_{dr} (dB)	LDR (dB)	K_{dp} (° km^{-1})	ρ_{hv}
Small hail (D < 2 cm)	≥ 50	≤ 0.5	< -18	< 0.5	> 0.96
Small hail and rain	≥ 50	< 1.0	-27 to -20	≥ 0.5	≤ 0.98
Large hail (D ≥ 2 cm)	≥ 55	≤ 0.5	≥ -18	< 0.5	≤ 0.96
Large hail and rain	≥ 55	< 1.0	≥ -20	≥ 0.5	≤ 0.96
Rain	< 60	> 0.5	< -27	≥ 0.5	≥ 0.97

Table 2.3: Hydrometeor identification matrix, based on multiparameter radar data, used in this study to distinguish between bulk precipitation types below the freezing level.

VHF Interferometer Characteristic	Value during STERAO-A
Frequency band (MHz)	110-118
Bandwith (MHz)	1
Time resolution (μs)	23
Elevational resolution (°)	0.5
Azimuthal resolution (°)	0.25

Table 2.4: Characteristics of the ONERA VHF lightning interferometer during the STERAO-A field project.

ITF Flash Classification Criteria	Value for Analysis
Maximum burst velocity ($m\ s^{-1}$)	100,000,000
Minimum duration of a leader/spider discharge (μs)	800
Minimum altitude of a leader (m) – above this altitude it's a spider discharge, below it's a leader	1,500
Maximum number of sampling periods (23 μs each) between two successive points of a burst	10
Maximum duration of a flash (μs)	1,000,000
Maximum distance between two bursts of the same flash (m)	25,000
Maximum time between two bursts of the same flash (ms)	250

Table 2.5: Criteria used by the ITF analysis software to separate and classify flashes.

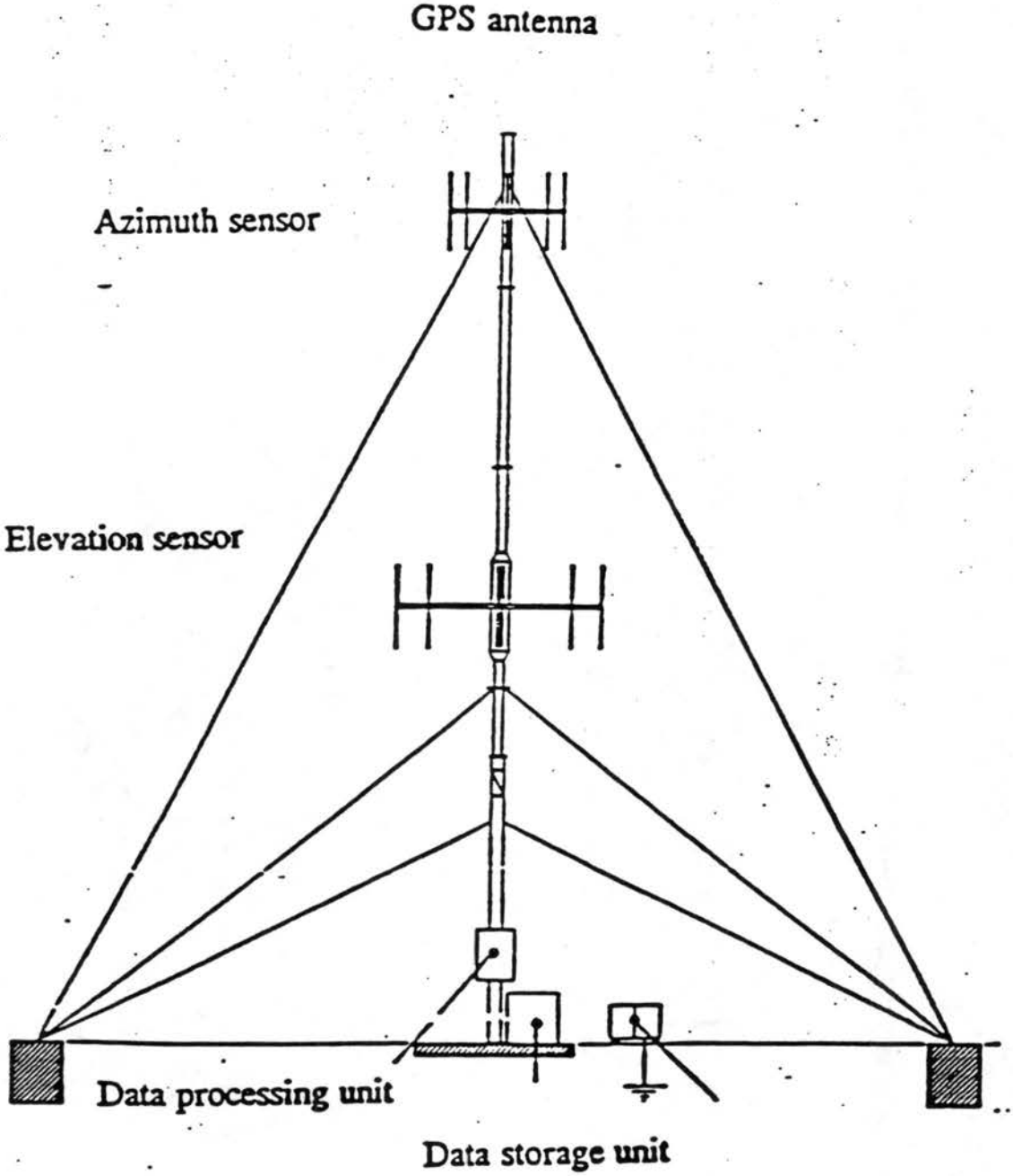

Figure 2.1: Schematic representation of the combined elevational and azimuthal receiving station for the ONERA VHF interferometer. The azimuthal-only receiving station is similar in appearance, but lacks the elecation sensor and hence is somewhat shorter.

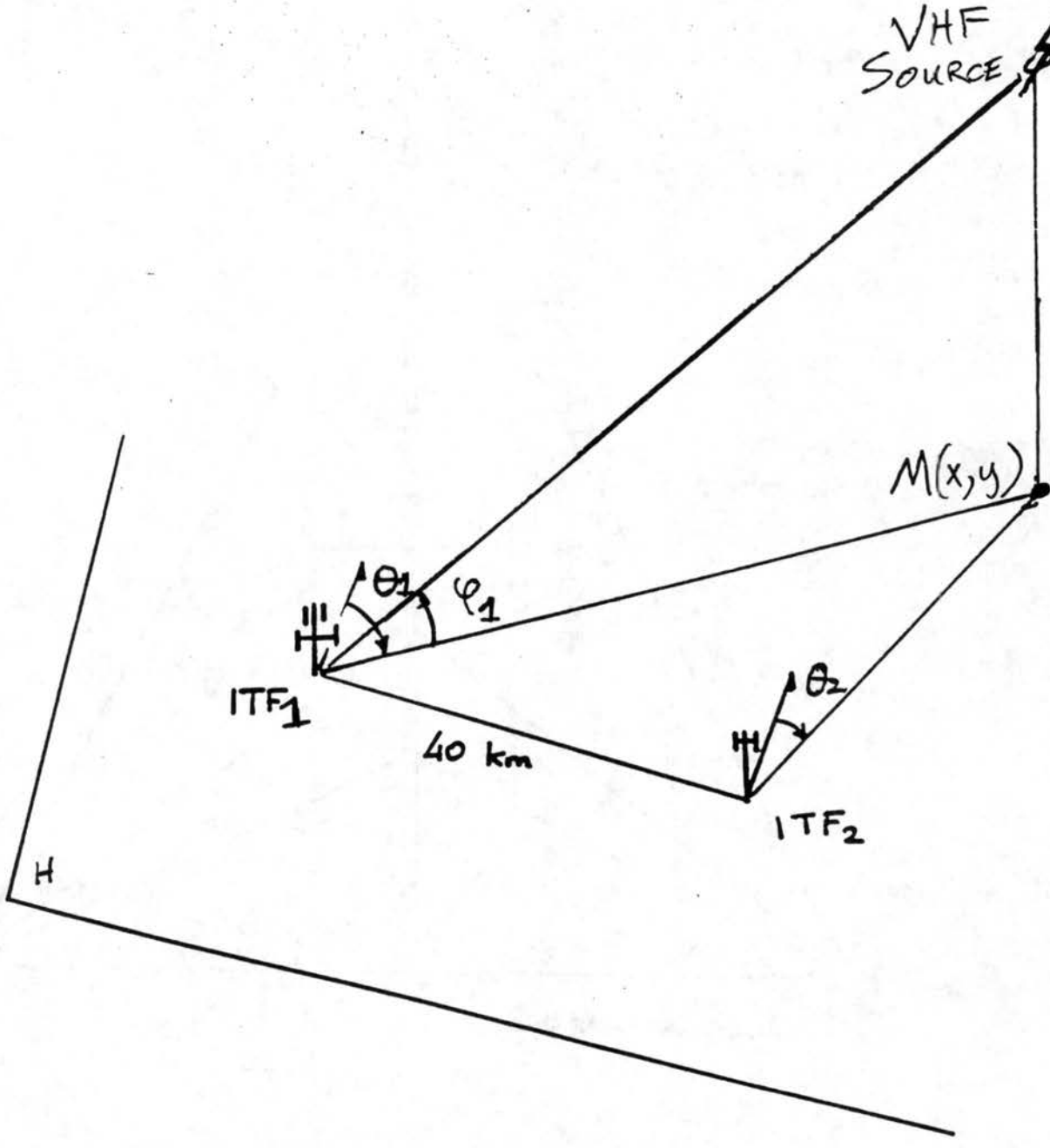

Figure 2.2: Schematic illustration of how the two VHF interferometer receiving stations combine to give the three-dimensional location of a VHF source. The combined azimuthal and elevational receiving station, ITF_1, gives an elevation angle, φ_1, and an azimuthal angle, θ_1, to the source. The azimuthal-only station, ITF_2, gives an additional azimuthal angle, θ_2, to the source. The projection of the three-dimensional VHF source onto the horizontal plane, H, gives the two-dimensional location of the source, M(x,y).

CHAPTER 3

INTERCOMPARISON OF LIGHTNING SENSORS

In this chapter the data from the different lightning sensors used during the STERAO-A field project - specifically the VHF lightning interferometer (ITF), the National Lightning Detection Network (NLDN), and the flat plate antennas (FCM) - are compared. The objective of this intercomparison is to develop a strategy for interpreting the ITF data, so that it can be used properly in the case studies (Chapters 4 and 5).

3.1 VHF lightning interferometer vs. the National Lightning Detection Network

3.1.1 Introductory material

Before commencing with the intercomparison of the ITF and the NLDN data, it is important to note that these platforms measure different aspects of lightning. To summarize, the ITF maps VHF emissions from lightning, both intra-cloud (IC) and cloud-to-ground (CG). However, as was noted in the last chapter, only certain parts of a lightning discharge are expected to radiate strongly in the VHF band. For example, the negative stepped leader process of a CG discharge is associated with VHF emissions, but return strokes and positive discharges emit only weakly at VHF frequencies. Thus, the ITF is expected to map the leader stages of a CG well, but will have a difficult time mapping return strokes and positive CGs. The ITF is additionally hampered by its reduced vertical resolution at low elevation angles, as discussed in Chapter 2. Furthermore, the

added vertical resolution degradation that occurred during STERAO-A (also discussed in Chapter 2) compounds the task of properly detecting, classifying, and mapping CG lightning with the ITF.

In contrast, the NLDN detects only the return stroke stages of a CG. It is not intended to detect or locate IC lightning, though it is possible that some ICs are falsely identified as CGs by the NLDN, as discussed in Chapter 2. In contrast to the ITF, which locates the positions of the negative leaders (i.e., the flash channels), the NLDN only locates the ground strike positions of CG lightning, not the positions of the flash channels themselves.

For the purposes of this intercomparison then, CG data from the two sensors will be compared. Note that flashes are not classified as CGs by the ITF in real time. Instead, they are classified during post-processing with the use of an altitude threshold on negative leader processes, as mentioned in Chapter 2. This classification algorithm is still in testing at ONERA. Later versions of ITF data from 10 and 12 July 1996 (received from ONERA) need not have flashes classified the same. The NLDN data are not expected to change in the future, however.

3.1.2 Intercomparison of ITF and NLDN data from 10 July 1996

The storm of 10 July 1996 began as a multicellular line, but late in its lifetime one cell dominated and became supercellular in character, with mid-level rotation and a Weak Echo Region (WER). For much of its lifetime it stayed within the highest resolution eastern lobe of the ITF, making it an ideal case for comparing CG data from the ITF and NLDN. The storm was very isolated, with few unrelated cells nearby, so it was easy to remove CG data from these unrelated cells for the intercomparison. Five-minute CG rates

were calculated for the remaining data from both sensors and the results are plotted in Figure 3.1. CG rates for each 5-minute period are plotted at the start of their respective time periods. Both sensors appear to capture the CG burst between 1600 and 1645 MDT, and the subsequent dearth of CGs in the approximately 1-hour period following this burst. Then after 1745, CG rates from both sensors begin to diverge, with significant disagreement after 1830 through the end of the storm. After 1830, ITF CG rates became quite large, but NLDN CGs were almost nonexistent. Also, the NLDN CG burst around 1810 MDT was not captured by the ITF. Overall, the ITF detects and classifies significantly more CGs than the NLDN.

This disagreement between the CG data from the two sensors becomes even greater when an attempt is made to match individual CGs from the two sensors, in order to gain a sense of which "CGs" are being detected by only one sensor, and which are being detected by both. When matching individual CGs between the two sensors, two problems arose. One was that, at the time the intercomparison was done, only 1-second resolution data were available for the two sensors, so it was difficult to estimate the time difference between the two sensors' clocks. The second problem was that the ITF data contained the mean horizontal position of the radiating flash channel, whereas the NLDN data of course gave the ground strike location of the flash. CG lightning is known to travel horizontally, sometimes on the order of several km, before striking the ground. Thus the mean horizontal flash channel position and the ground strike location need not be identical, especially when the inherent location errors of the two sensors are considered. Thus, the criteria used to judge whether a given NLDN CG and a given ITF CG were the same were that they occurred at the same time, to the nearest second (due to the time

resolution of the data, and keeping in mind the fact that the two clocks were not synchronized during STERAO-A), and that their horizontal positions be within 10 km of one another. In practice it was found that the time criterion was the strongest; that is, when an NLDN CG and an ITF CG were coincident, they were almost always very close to one another, from a distance perspective. Thus, the distance criterion for flash matching was not very important; increasing the distance to greater than 10 km would not change the results significantly.

Using this flash matching algorithm, the following were identified: CG flashes which were detected by both sensors, CG flashes which were detected and classified by the NLDN only, and CG flashes which were detected and classified by the ITF only. The results are plotted in the form of 5-minute flash rates in Figure 3.2. As can be seen, during the early period of the storm's lifetime, when Figure 3.1 appeared to show rough agreement between the two sensors, Figure 3.2 demonstrates this agreement in bulk flash rates to be misleading. During this time there is a significant number of CGs that are being detected and classified by only one sensor; the other sensor is either not detecting anything, or it is not classifying any detected flash as a CG. This problem only becomes worse after 1745 MDT. For the entire storm, the number of CG flashes detected and classified by both sensors is quite low, especially compared to the number of CGs detected and classified by only one sensor. After 1830, the number of CGs detected and classified by the ITF only is especially high, as might be expected based on Figure 3.1.

There is a small population of flashes detected and classified as CGs by the NLDN, but not by the ITF. An attempt was made to match these NLDN CGs to ITF ICs using the same algorithm for matching NLDN and ITF CGs. Interestingly, all of these NLDN CGs,

save one, corresponded to a detected and classified ITF IC. If the CG intercomparison is specialized to only NLDN positive CGs, then 1 of 13 NLDN positive CGs corresponded to an ITF CG. Most of the remainder corresponded to ITF ICs.

3.1.3 Intercomparison of ITF and NLDN data from 12 July 1996

The same CG data intercomparison performed on 10 July data also was performed on the 12 July data. The storm of 12 July 1996 began as a cluster of several cells over the Cheyenne Ridge in southeastern Wyoming. As the storm moved to the southeast and entered Colorado, the storm remained multicellular. Substantial reflectivity (> 40 dBZ) continued to cover a large area throughout the remainder of the time of radar sector coverage. With such large areas of contiguous echo, the storm was not very isolated, so the ITF data were not edited to exclude unrelated cells. The NLDN data were edited to exclude flashes outside the ITF lobes, however. This intercomparison was done using older ITF data, like the 10 July intercomparison. These data covered the time period from 1730 to 1910 MDT. After this time span, the storm moved out of the lobes, so later data were impacted by these lobe effects. Figure 3.3 is a plot of 5-minute CG flash rates for both sensors throughout the intercomparison time period. Much like 10 July, overall the ITF detects and classifies many more CGs than the NLDN, but unlike 10 July this occurs throughout the analysis period, not just during a portion of it.

Individual CGs were matched using the method employed with the 10 July data. The result is Figure 3.4, which is the same as Figure 3.2 except now for 12 July. In general, very few CGs are detected and classified by both sensors. CGs detected and classified by only the ITF dominate the plot.

Of the 21 CGs that were detected and classified by only the NLDN for this time period, 12 matched up with detected and classified ITF ICs. Sixteen of these 21 NLDN-only CGs were positive CGs.

3.2 VHF lightning interferometer vs. flat plate antennas

For 12 July 1996, concurrent data from the flat plate fixed at the CHILL radar and from the ITF exist from 1747 to 1910 MDT. One-minute total flash rates were calculated during post-processing of the FCM data for this time period. By combining the ITF CG and IC data, one-minute ITF total flash rates can be computed. However, in order to properly compare these two estimates of storm total flash rate, the issue of the flat plate's limited range must be addressed. As stated in Chapter 2, the CHILL flat plate had a range of 35-40 km at the most sensitive gain setting, which is what it was set at during this time period. However, recall that the flat plate's detection efficiency is a function of both range to flash and flash strength. Thus, the ITF data were filtered to exclude, from the flash rate calculations, flashes beyond a certain distance from CHILL. Because of the uncertainties about flat plate range and detection efficiency, this filtering distance was varied and sensitivity tests were performed.

Figure 3.5 shows 1-minute total flash rates from both the ITF and the CHILL FCM. The filtering distance in this case was 35 km, the lower limit of the flat plate maximum range estimate. Note that any trends seen in these data do not necessarily reflect true trends in storm flash rate. The large increase in flash rates from both sensors toward the end of the period is mostly due to the storm moving into range for the FCM, and moving into the 35 km filtering circle for the ITF. In general, the ITF detects many more flashes

than the CHILL FCM, though the two flash rates seem to trend one another fairly well, especially toward the end of the intercomparison period.

Table 3.1 lists the square of the correlation coefficient, ρ^2, for the two flash rates throughout this intercomparison period, for different filtering distances ranging from 20 km to 40 km. The correlation between the two flash rates increases as the filtering distance becomes more restrictive, with ρ^2 reaching a maximum of 0.935 when ITF flashes with mean positions more than 20 km away from CHILL are excluded. A minimum of 0.774 occurs when ITF flashes with mean positions more than 40 km away from CHILL are excluded. This is strong evidence that the detection efficiency of the FCM is range dependent, if we assume that the ITF has a detection efficiency near 100% (or at least is mostly independent of range from CHILL). Correlations improve as the ITF range filter becomes more restrictive because distant flashes are detected by the FCM less often than closer flashes.

There is the possibility of some minor precipitation contamination of the CHILL FCM during the time period 1845-1900 MDT as the main storm grazed the radar site. Thus, FCM flash rates during this time may be artificially elevated, with an unknown but probably minor effect on the correlation analyses.

Despite its limitations, and assuming that the ITF has a very high detection efficiency, it appears that the FCM is a good tool for estimating total flash rate trends, based on this intercomparison. However, it is preferable that the storms sampled by the flat plate move slowly or be nearly stationary, in order to control false trends created by storm movement into and out of range.

3.3 Short-duration flashes in the VHF lightning interferometer data

Figure 3.6 shows normalized frequency distributions of ITF-derived flash durations for the storms of 10 and 12 July. These are the durations of the VHF emissions from each flash, and thus may not necessarily reflect the true flash durations (i.e., the time for which the lightning channel is ionized and current is propagating). Flash data have not been edited in any way. The plot limits extend from the lowest possible time resolution of the ITF, 23 μs, to the maximum allowed duration of a flash, 1 second (set by the flash-classification criteria). The distributions for both days are very similar. Why this is so is not certain. Both days' data contain several thousand flashes each, so whatever is forcing the similarity of the two distributions is likely common to both days. The distribution shapes may be caused by the ITF or its classification algorithm, making the distributions entirely or partly instrument-related artifacts. Or, the spectra could be due to the physics of the lightning, which also would be common to both days, as long as the processes governing the electrification and electrical discharging of these two storms were the same. It is not known which of these two possibilities, if any, are true. However, ONERA researchers have no idea how the ITF or its flash classification algorithm could force the distributions presented here (P. Laroche, private communication, 1997).

The distributions themselves appear to be bimodal. The first mode which will be considered is centered around $10^{-0.6}$ s, or 250 ms. This mode is distributed roughly lognormally, and appears consistent with other observed lightning duration spectra (Uman, 1987).

The second mode is a bit more complex, and is less easily understood. The maximum occurs at $10^{-4.6}$ s, or 23 μs, the temporal resolution limit of the ITF. In fact, over 20% of flashes on either day last 23 μs or less, more than any other bin in the entire distribution. This corresponds to a single localization of VHF radiation as seen by the ITF. There are also a few gaps in the distributions for this particular mode, where no flashes with the given durations occur on either day. This is a curious phenomenon as the surrounding bins contain relatively large numbers of flashes.

The tails of the two modes appear to meet somewhere in the vicinity of $10^{-3.0}$ s, or 1 ms. This duration, 1 ms, was chosen as the boundary between the two modes. While this decision is somewhat arbitrary, it is apparent from the spectra that, because so few flashes occupy the region from $10^{-3.0}$ s to $10^{-2.0}$ s, or 1 ms to 10 ms, choosing a different boundary between these two durations will not change the results significantly. Thus, the ITF flash duration frequency spectra were considered to be comprised of two different populations of flashes: a more standard flash population with approximately lognormally distributed durations, centered near 250 ms in this case; and a population of "sub-millisecond" flashes with durations on the order of individual strokes in a flash (Uman, 1987). The former population is probably what most researchers consider lightning flashes (Uman, 1987); the nature of the latter population is in question, but it is important to understand this nature as these sub-millisecond flashes make up close to one-third of the flash populations for either day. Maier et al. (1996) have reported observing similar short-duration "flashes" with the Lightning Detection and Ranging (LDAR) system, a time-of-arrival (TOA) VHF mapping system at the Kennedy Space Center in Florida.

There are a few possible explanations for these sub-millisecond (hereafter referred to as sub-ms) flashes. One is that they actually are components (i.e., individual strokes) of longer flashes – perhaps flashes that also are detected and classified by the ITF, and are part of the more standard flash population – but are being falsely classified as separate flashes by the ITF classification algorithm. The flash classification algorithm is very likely not perfect, and so some errors in flash classification are expected. Some of these sub-ms flashes do appear to be quite close, in space and time, to other, longer flashes. However, many sub-ms flashes are isolated in both time and space.

Another explanation is that, while the VHF emissions from these sub-ms flashes may last less than 1 ms, the actual flashes themselves last much longer. That is, perhaps many of these sub-ms flashes actually are longer flashes which do not radiate strongly in the VHF, like positive flashes and return strokes, so only a few VHF radiation localizations can be attributed to them, giving the false appearance of a short duration for the entire flash.

A final possibility is that these sub-ms flashes may be in fact true short-duration flashes lasting on the order of tens of microseconds, perhaps a subset of IC discharges. This possibility has been examined before, by Taylor et al. (1984), who used a VHF mapping system in a single storm to distinguish between long-duration (i.e., standard) IC flashes, which occurred near the middle of the thunderstorm, and short-duration IC flashes which were centered near the top of the storm, in the vicinity of the positive charge region (Williams, 1989). Unlike the sporadic long-duration IC events, the short-duration ICs occurred on a near-continuous basis. In a private communication, P. Krehbiel (1997) mentioned that these sub-ms flashes instead may be what he called "positive bi-polar

discharges". These discharges last on the order of 10-20 μs, and can be considered a kind of failed upward-propagating leader from the region of negative charge near cloud mid-levels (Williams, 1989). The "failed leader" does not reach the upper positive charge region, and thus no return strokes or recoil streamers occur.

In order to understand how to best interpret these sub-ms ITF flashes, a more detailed intercomparison of the ITF and FCM data was performed. Figure 3.7 is the same as Figure 3.5, except that ITF flashes with durations less than 1 ms also have been excluded from the analysis. Not surprisingly, ITF flash rates have been reduced, but the ITF still counts many more flashes than the CHILL FCM. Table 3.2 lists the results of correlation analyses of flash rates from the two sensors. The format is the same as Table 3.1, except now ITF flashes lasting less than 1 ms have been excluded. In all cases, correlations have improved over those presented in Table 3.1, which includes the sub-ms flashes.

As mentioned in Chapter 2, the CHILL FCM data are sampled at 1 kHz. Thus, the FCM cannot possibly resolve events associated with electrostatic field changes lasting less than 1 ms. Indeed, undersampling of events lasting longer than 1 ms, say up to 10 ms, will also be a problem with this sensor. Because the correlations improve when the sub-ms ITF flashes are excluded from the analyses, the sub-ms flashes likely are not being detected with good efficiency by the FCM. The FCM cannot detect anything shorter than 1 ms, so this implies that the sub-ms flashes also tend to be associated with electrostatic field changes lasting less than 1 ms. Another possibility is that these events may last lionger than 1 ms but are not associated with substantial electrostatic field changes, so that they do not register well on the flat plate.

If the sub-ms ITF flashes were actually parts of longer flashes that do not radiate strongly in the VHF, then these flashes probably should register electrostatic field changes lasting significantly longer than 1 ms, on average. Recall from previous discussions that such flashes could consist of positive discharges and return strokes. These events commonly are registered on this type of FCM (Carey and Rutledge, 1997), so a significant percentage of them should be detectable in the FCM data. A fellow member of the radar meteorology group at Colorado State University, J. Ryan, looked for evidence of sub-ms ITF flashes that were isolated in time and space in the CHILL FCM data from 12 July 1996. He considered 80 such ITF flashes, lasting between 23 and 500 μs, and having mean horizontal positions within 35 km of the CHILL FCM. He found no signals corresponding to these flashes, which is what would be expected if such flashes were associated with electrostatic field changes lasting less than 1 ms (J. Ryan, private communication, 1997). This, along with the observed trend of improved correlations when the sub-ms ITF flashes are excluded, implies that these sub-ms ITF flashes are not parts of longer, non-VHF emitting flashes, so this possibility is ruled out on a tentative basis.

If the sub-ms ITF flashes are actually parts of longer, detected discharges, and thus are being falsely classified as separate discharges by the ITF, then removing them from the correlation analyses should improve the correlations, as the ITF would be counting individual flashes twice or more, whereas the FCM, if it detects the flashes, would count them only once. Thus, this possibility cannot be ruled out because it is consistent with the observed improvement in flash rate correlations when the sub-ms ITF flashes are excluded.

If the sub-ms ITF flashes are in fact true short-duration discharges with electrostatic field changes lasting less than 1 ms, then the FCM could not detect them. Thus, when they are removed from the ITF/FCM intercomparison, correlations should improve, as is observed. Thus, this hypothesis is consistent with the data analysis results as well.

So there are two possible hypotheses consistent with the observed increase in correlations when the sub-ms ITF flashes are excluded from analysis. Note, however, that the hypothesis that these sub-ms flashes are parts of longer, detected and classified ITF flashes does not explain the large number of observed sub-ms flashes which are isolated in both time and space. These isolated flashes probably can be interpreted only as true individual short-duration IC flashes. Non-isolated flashes could be explained by either hypothesis, or perhaps a combination of both.

3.4 How the ITF data will be interpreted in this study

There are two issues to consider when interpreting the ITF data in terms of flash rates. The first is the IC/CG classification problem discussed in Section 3.1. The second is the sub-ms ITF flashes which were examined in Section 3.3.

The NLDN is reported to have close to a 90% detection efficiency in northeastern Colorado (Cummins et al., 1996). Additionally, no positive CGs with peak currents less than 7 kA were observed, so all NLDN CGs from both days are likely true CGs and not mis-classified ICs. In addition, the NLDN is generally accepted by most researchers to be the current "industry standard", having been used in a large number of published research studies which are too numerous to mention here.

In contrast, the ITF to a certain extent is still under development, particularly its flash classification algorithm. The algorithm used to classify a given flash as a CG is essentially an altitude threshold on a leader process. Recall that the CG leader stroke resembles a spider lightning discharge to a VHF interferometer like the ITF. Spider discharges, being IC flashes, typically have higher mean altitudes than CG leaders. Thus, an altitude threshold would work to distinguish the two provided the ITF does a good job in resolving altitude differences. However, as discussed in Chapter 2, the ITF had unusually poor elevational resolution during STERAO-A. Compounding this problem is the generally poor low-elevation angle resolution of the ITF, regardless of any additional problems. Thus, it is best to suspect the ITF of error in classifying CGs rather than the NLDN.

The sub-ms ITF flashes, as stated before, are probably either components of longer, detected and classified ITF flashes, or they are individual short-duration flashes in their own right, or perhaps some combination of the two. In any case, eliminating them from consideration reduces the possibility of counting the same flash twice (or more), and reduces the possibility of counting short-duration flashes as part of the standard (i.e., long-duration) IC flash rate. Given the large uncertainty regarding the nature of these short-duration discharges, it is probably best to disregard them for the purposes of this study since it is geared toward using the ITF data to compute IC flash rates, not looking at the physics of the lightning discharge itself, or exploring the natures of the different types of lightning discharges. Also, removing these discharges from consideration leaves a flash duration spectrum more in accord with past studies involving IC lightning (e.g., Uman, 1987), so flash rates are more comparable to previous studies.

These short-duration flashes, if they exist in reality, are certainly worth studying in their own right, though they will not be the focus of this thesis. However, in order to better examine the implications of removing them from consideration, Figure 3.8 was developed using the latest version of the ITF data, the version used in the radar/lightning case studies (though not the same version used in the lightning sensor intercomparisons in this chapter). It shows IC and sub-ms 5-minute flash rates for 10 July 1996. No editing of the flashes has occurred (except for removing from consideration those flashes classified by the ITF as CGs); they have merely been categorized by flash type. The sub-ms category contains all flashes lasting less than 1 ms, and the IC flash category contains all IC flashes lasting 1 ms or more. Note that all sub-ms flashes were classified as ICs by the ITF. *In general, the sub-ms flash rate trends the IC flash rate fairly well.* The square of the correlation coefficient for these flash rates is 0.610. This is consistent with the sub-ms flashes being, at least in part, components of longer detected flashes, as they would be very related then. However, if the sub-ms flashes are, at least in part, individual short-duration IC discharges, this result is still consistent provided the short- and long-duration flashes are related somehow. Thus, the truth of either possible explanation for the sub-ms ITF flashes cannot be discerned completely. However, it is apparent that the relatively high correlation between the sub-ms and regular IC flash rates implies that removing the sub-ms flashes from consideration will not change IC flash rate trends significantly, though absolute flash rates will change. As this study is most interested in flash rate trends, removing the short-duration discharges from consideration will not make a major impact on results.

Thus, based on this chapter's analyses and discussion, the following method will be used in this study to determine IC and CG flash rates. *Flashes lasting less than 1 ms will be removed from the processed ITF flash data. Then, NLDN CGs will be individually matched to remaining ITF flashes, regardless of whether the ITF classified them as CGs or ICs, following the method outlined in Section 3.1. Those ITF flashes matching NLDN CGs in time will be removed from the ITF data as well. The remaining ITF flashes will be considered ICs, and the NLDN CGs will form the CG data set.*

This algorithm thus removes the sub-ms flashes from any further consideration. Though this eliminates the ability to consider any possible individual short-duration ICs, it also avoids the problem of possibly overcounting ICs because some of the sub-ms ITF flashes may be components of longer, detected flashes. This algorithm also avoids relying on the suspect CG flash classification method of the ITF. Another problem that the algorithm avoids is cases where CGs are detected and classified by the NLDN, but are not detected at all by the ITF. The algorithm ensures that these NLDN-only CGs will remain in the CG data set.

One possible source of error in this algorithm is the fact that the NLDN's detection efficiency is not 100% in northeastern Colorado. Thus, the NLDN may fail to detect a CG, but that CG may be detected by the ITF. Such a flash, by this algorithm, would be falsely considered an IC. However, the NLDN's detection efficiency in northeastern Colorado is around 90% or more (Cummins et al., 1996), so it is quite high. However, this estimate has never been independently verified in this specific region, so any possible error in this estimate, or whether such an estimate is storm-dependent, is unknown.

However, there is no other estimate available, and there is no reason – beyond healthy skepticism – to suspect this estimate to be in error. Hence, it must be used.

Based on this detection efficiency estimate, the error associated with this algorithm is not likely to be much more than 10% of the CG population, which should not seriously impact CG flash rate trends. Because both storms in question were very poor producers of CGs in the first place, this should not impact the (often high) IC flash rates significantly. Any error associated with this algorithm is probably minuscule compared to the error associated with applying the ITF CG classification method used by ONERA. Figures 3.1 through 3.4 show that fact very clearly.

This approach is different than that of Lang et al. (1997), who computed total flash rate for the 10 July 1996 storm by editing out of the ITF data only those flashes that were not associated with the storm of interest. Sub-ms flashes and ITF "CGs" were included in the total flash rate. However, as will be seen in Chapter 4, the flash rates computed by Lang et al. trend the results of this study quite well, mainly because the sub-ms flashes trend the long-duration ICs so well, and because NLDN CG rates were not high enough to impact total flash rates significantly.

ITF Flash Filtering Distance (km)	ρ^2
20	0.935
25	0.912
30	0.853
35	0.786
40	0.774

Table 3.1: Square of the correlation coefficient, ρ^2, between one-minute ITF and CHILL FCM flash rates for the 12 July 1996 storm as a function of the filtering distance (from CHILL) applied to the ITF data. Flashes outside this distance are not considered in the ITF flash rate calculations.

ITF Flash Filtering Distance (km)	ρ^2
20	0.952
25	0.934
30	0.897
35	0.856
40	0.851

Table 3.2: Same as Table 3.1 except that ITF flashes lasting less than 1 ms have been excluded from flash rate calculations.

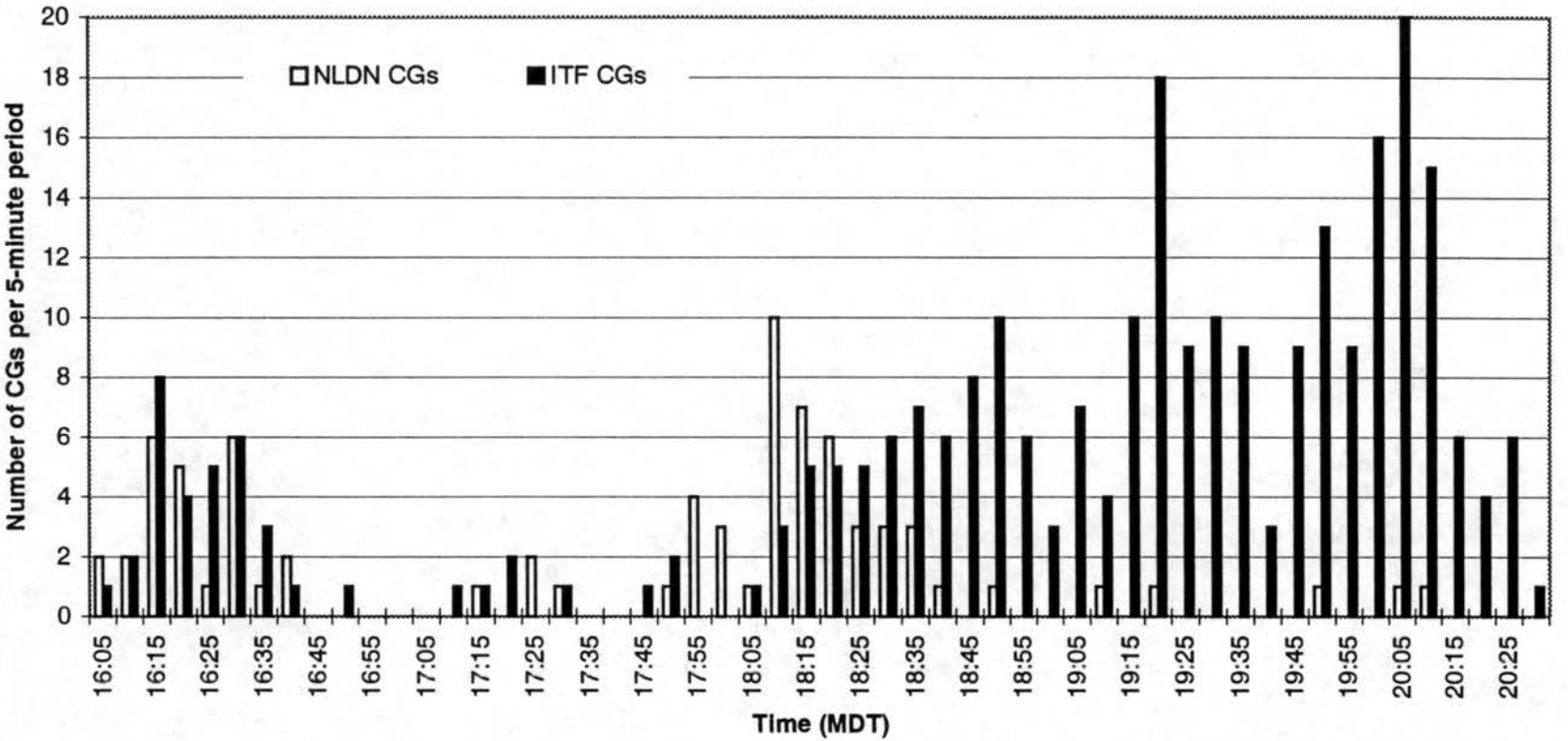

Figure 3.1: Five-minute NLDN and ITF CG rates as a function of time for the 10 July 1996 storm.

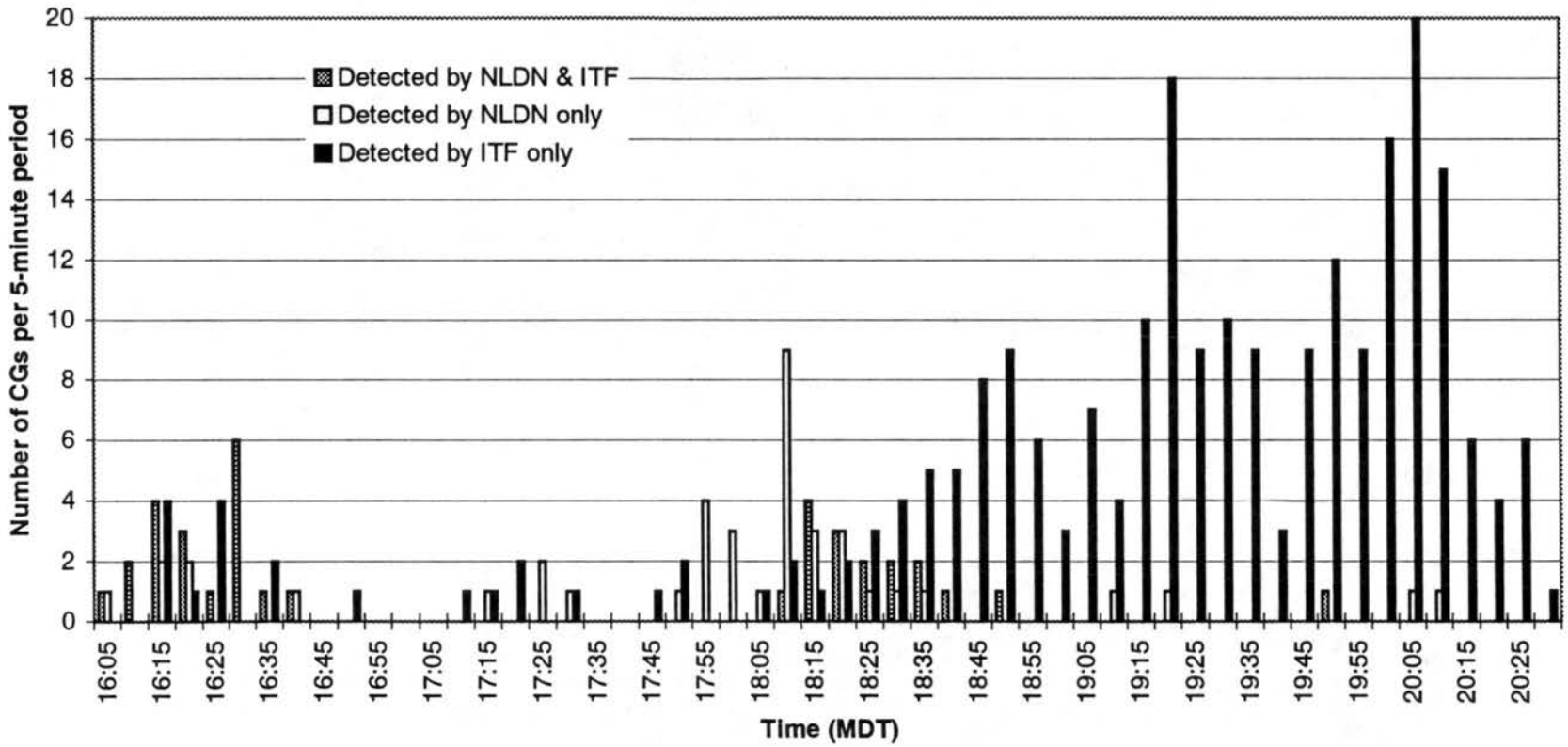

Figure 3.2: Five-minute CG rates as a function of time for the 10 July storm. CGs are split into three categories: those detected and classified by both the ITF and NLDN, those detected and classified by only the ITF, and those detected and classified by only the NLDN.

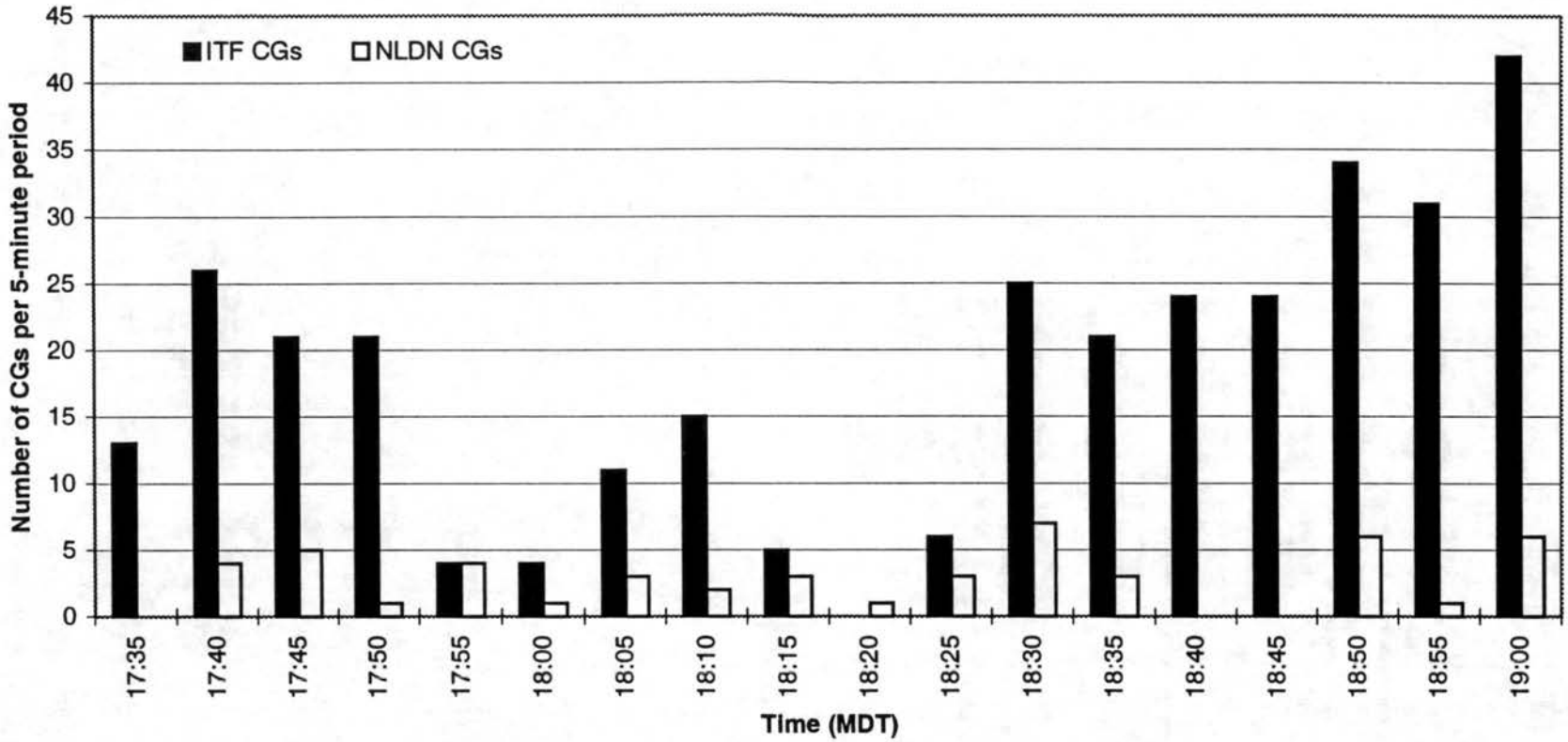

Figure 3.3: Same as Figure 3.1 except for the 12 July 1996 storm.

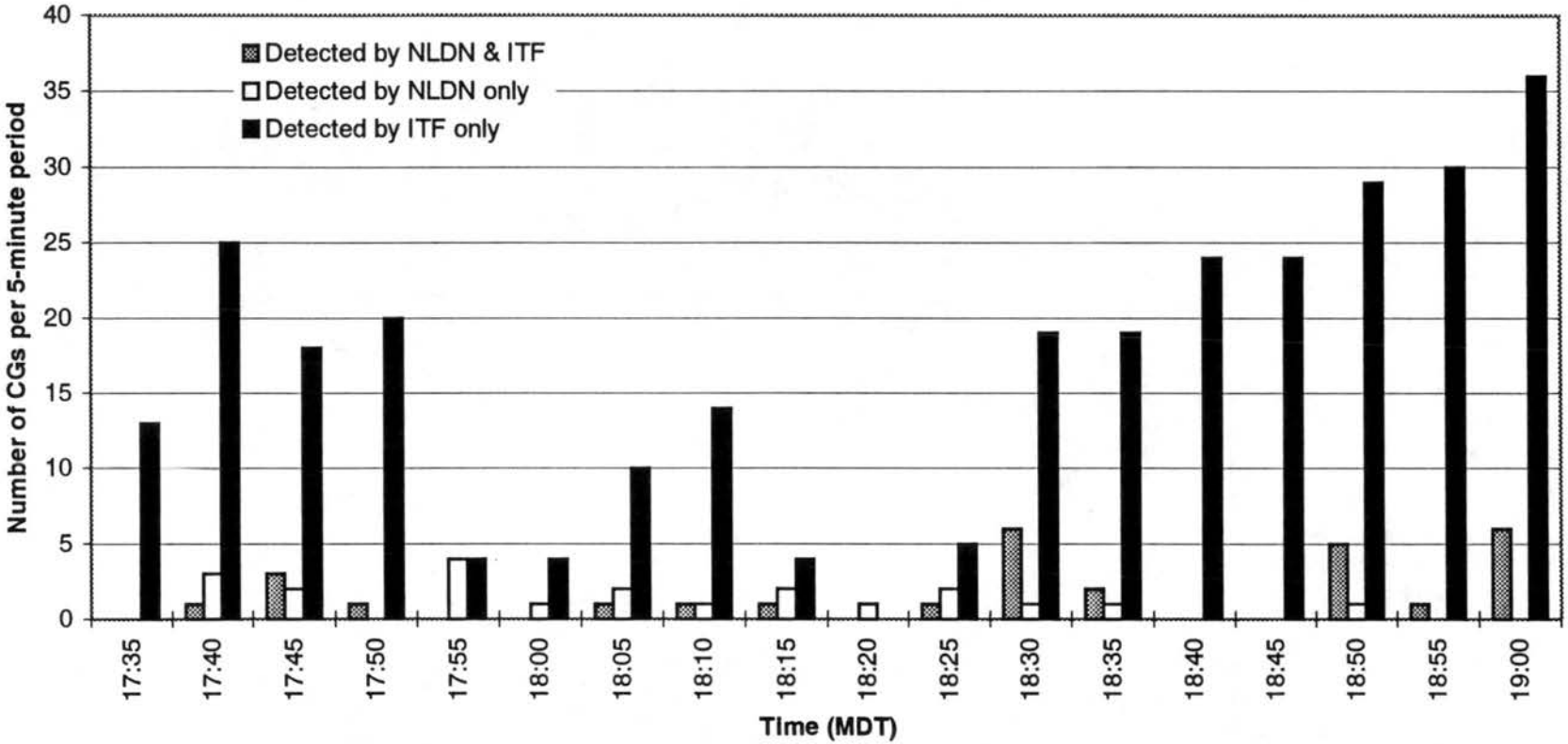

Figure 3.4: Same as Figure 3.2 except for the 12 July 1996 storm.

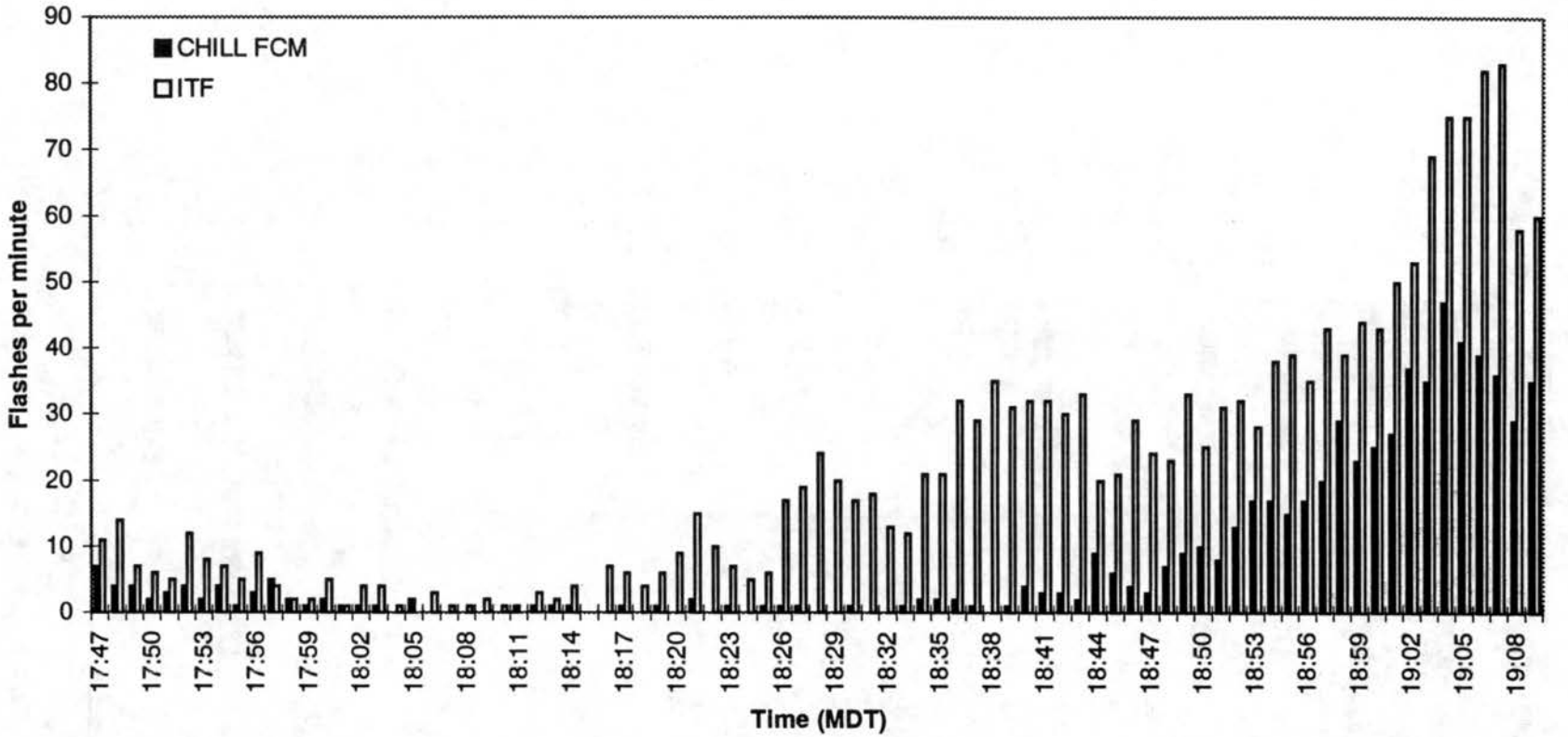

Figure 3.5: One-minute ITF and CHILL FCM total flash rates as a function of time for the 12 July 1996 storm. ITF flashes farther than 35 km from the CHILL radar have been excluded from ITF flash rate calculations.

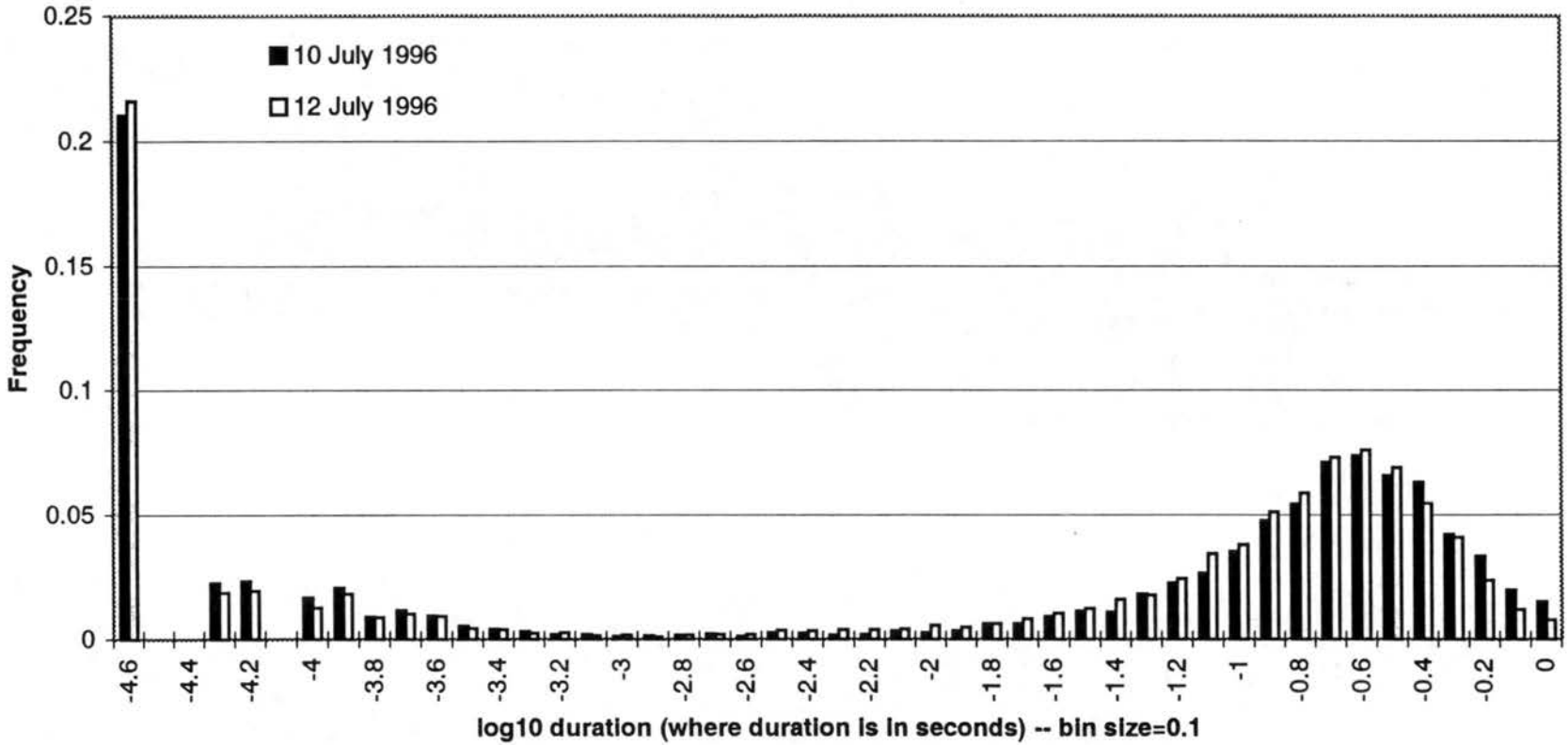

Figure 3.6: Normalized ITF flash duration frequency spectra for two different storms: 10 July 1996 and 12 July 1996. The spectra are normalized by dividing the number in each bin by the total number of flashes on the respective day. Note that the abscissa of this plot is logarithmic.

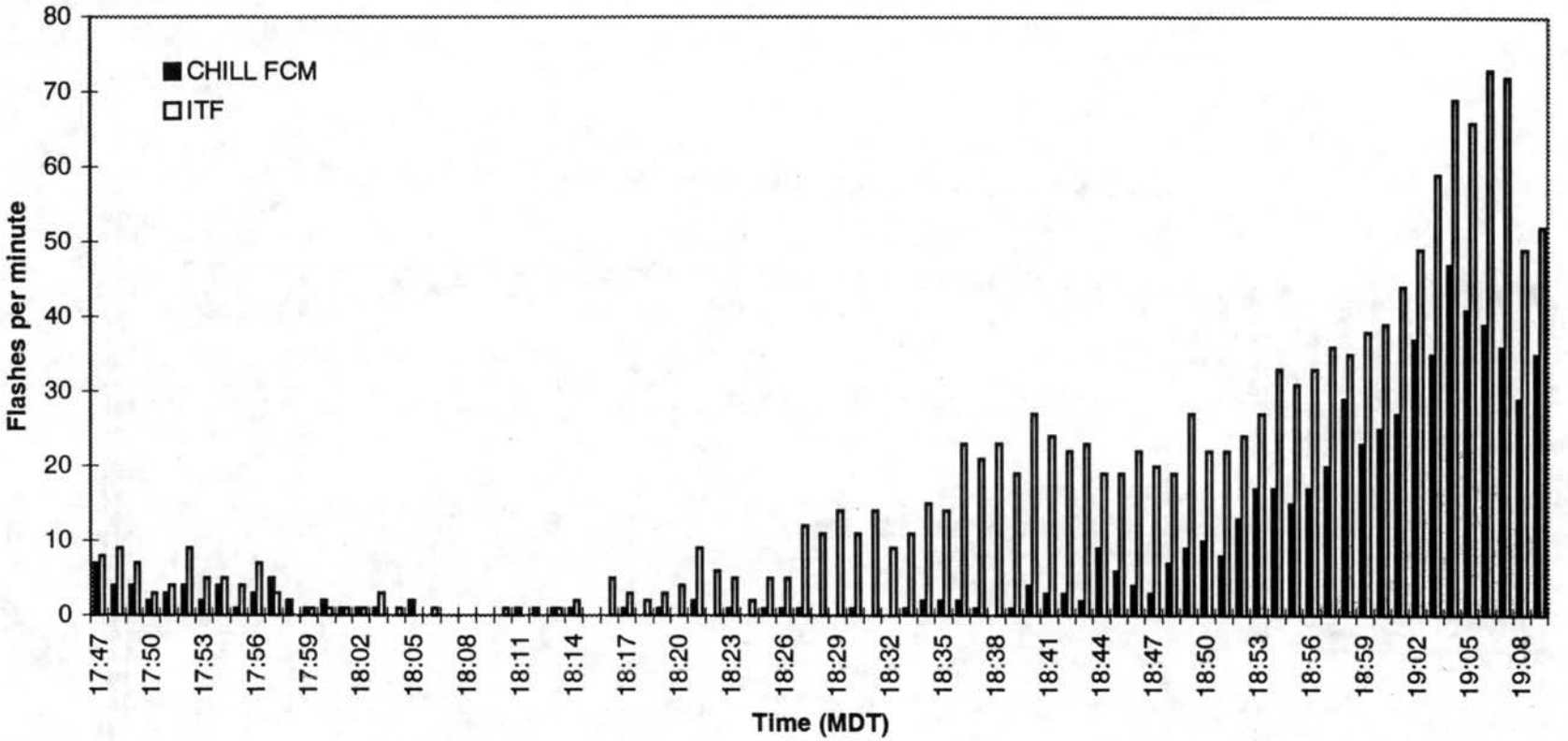

Figure 3.7: Same as Figure 3.5 except that ITF flashes lasting less than 1 ms have been excluded as well.

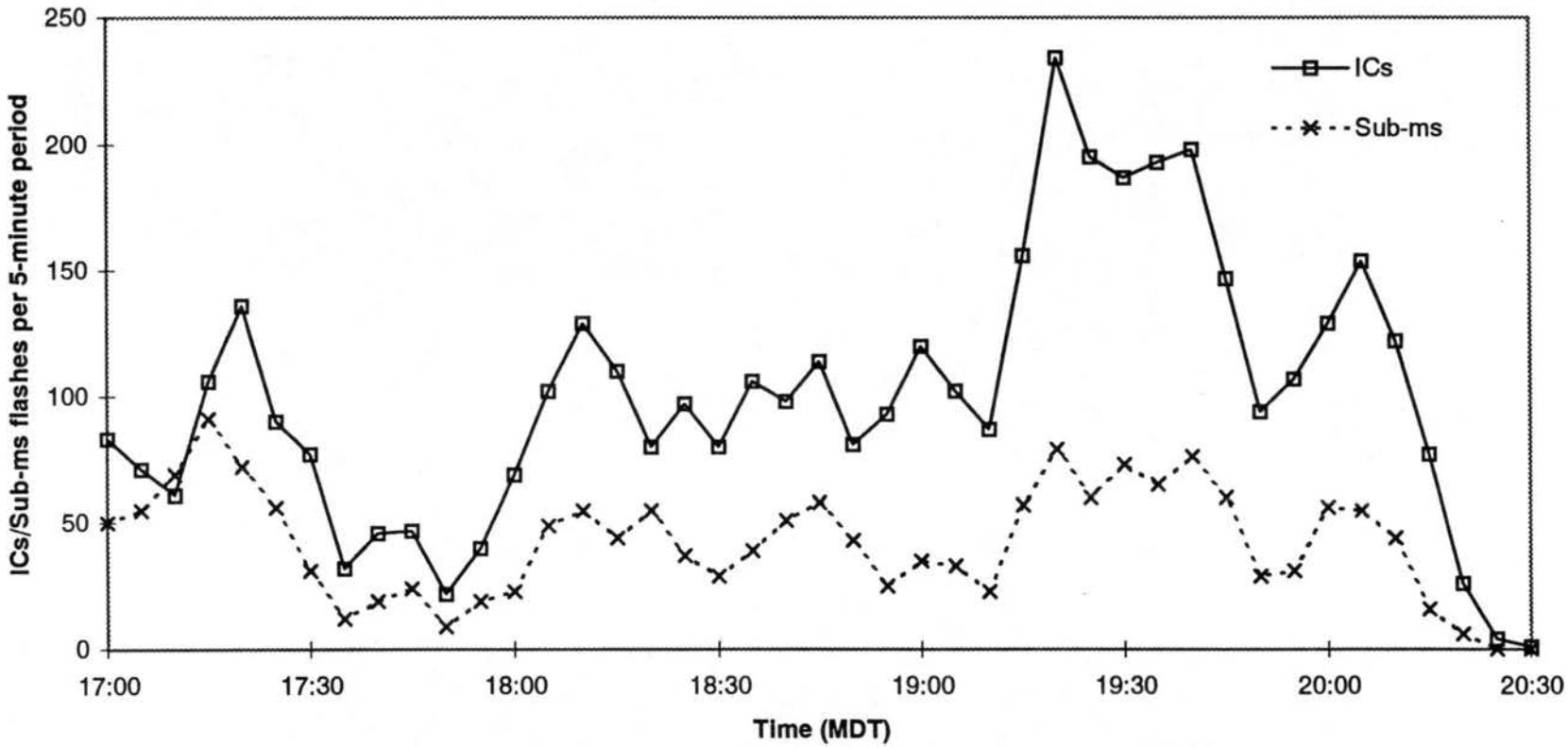

Figure 3.8: Five-minute ITF IC and sub-ms flash rates for 10 July 1996. Sub-ms flashes are defined as flashes lasting less than 1 ms. ICs are IC flashes lasting 1 ms or longer.

CHAPTER 4

ANALYSIS OF THE 10 JULY 1996 STORM

The storm of 10 July 1996 represents an excellent example of a major transition in storm structure, as the storm evolved from a multicellular line, to a single-cellular storm with characteristics common to supercells. Cloud-to-ground (CG) lightning rates were low throughout its lifetime, making it a good case for which to study low CG production by intense storms.

4.1 Atmospheric conditions

Figure 4.1 shows data from a mobile CLASS sounding launched from the Fort Morgan Airport at 1450 MDT on 10 July 1996. Plotted on the Skew-T/Log-p diagram are vertical profiles of temperature, dewpoint, and winds. The sounding appears to be relatively dry. The CAPE is 792 J kg^{-1}, the shear over the lowest 6 km is 14.4 m s^{-1}, and the Bulk Richardson Number (BNR) is 7.7. The BNR is very low but is suggestive of possible supercellular development (Weisman and Klemp, 1982). It is so low because the CAPE is also low. The ambient wind shear is weak as well. However, the Lifted Index is -2.8, which implies that convection was at least possible. But overall, the atmospheric environment did not appear conducive to the development of intense convection. However, this sounding may not have been entirely representative of the storm's environment, since the storm initially developed on the order of 80-90 km north of the

sounding launch location. Also, conditions could have changed between the time of the sounding and the time of storm development (i.e., a short wave may have propagated through the region after the sounding was taken). Note the relatively weak northwesterly winds at mid-levels. These may have been responsible for the storm's slow propagation to the south and east after it developed.

4.2 Overview of storm evolution and major transition

Figure 4.2 (a-i) shows a series of horizontal cross-sections of reflectivity (dBZ) obtained from the CSU-CHILL radar at 0.5 km AGL for the 10 July 1996 storm. The cross-sections are spaced approximately 30 minutes apart. When full-volume coverage of the storm began at 1629 MDT, the storm consisted of three cells, arranged in a line from northwest to southeast. At this point the storm was in southwestern Nebraska, near the town of Kimball. Because of its initial proximity to this town, the storm also shall be referred to as the Kimball storm. At 1629 (Figure 4.2a), the northwest cell (Cell 1) is separated from the other two cells by approximately 20 km. The other two cells (Cells 2 and 3) are enclosed by a common border of 30-40 dBZ reflectivity. However, the strongest cell is Cell 2, with low-level reflectivities peaking at greater than 50 dBZ. By 1701 MDT (Figure 4.2b), the Cell 1 was nearly gone, and Cell 2 had absorbed Cell 3. At this time, another cell had developed between Cells 1 and 2. This cell (Cell 4) had reached over 40 dBZ in low-level reflectivity at this time. Cell 2 was quite intense, with greater than 50 dBZ reflectivities encompassing a relatively large area, as well as a well-defined low-level notch in the core. Thirty minutes later, at 1731 MDT (Figure 4.2c), Cell 1 was completely absent, and Cell 4 had developed to greater than 50 dBZ reflectivity at 0.5 km

AGL. Cell 2 was still strong, though the reflectivity notch was gone. Both cores (Cells 2 and 4) were enveloped by a common 40-50 dBZ border, giving the appearance of a short, but intense squall line segment.

By 1803 MDT (Figure 4.2d), significant growth of new cells had occurred on the northwestern flank of the aggregate storm, and the azimuthal boundary of the radar scan was increased to scan these developing cells. Thus, Cells 2 and 4 from 1731 now comprised the southeasternmost cells of the line. Here there were still two separate reflectivity cores, but of these two cells, Cell 4 had decreased in intensity, while Cell 2 was still intense, and had elongated to a length of approximately 20 km. The developing cells (Cells 5 and 6) comprised the northwestern flank of the storm, and of these cells Cell 6 was the most intense in terms of low-level reflectivity at this time. Note the weak echo well to the southeast of the main line. This is a manifestation of the huge (radar-detected) anvil of this storm, which was advected to the south and east of the main line. This anvil was present in many low-elevation scans, indicating the presence of a significant area of stratiform rain/virga.

By 1834 MDT (Figure 4.2e), major changes had occurred in the storm complex. Cell 2 in the line from 1803, which at that time seemed quite intense, had dissipated, and the strongest reflectivity core was now Cell 4, which at 1803 seemed rather weak The northernmost cells (Cells 5 and 6) had weakened as well, with Cell 6 absorbing 5. Another cell, Cell 7, formed behind Cell 6.

At 1900 MDT (Figure 4.2f), the storm complex had redeveloped on its northern flank, and the strongest cell at 1834, Cell 4, was now quite weak Cell 6 was the most intense in terms of low-level reflectivity. By 1932 MDT (Figure 4.2g), the radar scan continued to

scan a larger sector to the west, in order to obtain data for a weak cell, Cell 8, that formed on the northern flank after 1900. The strongest cell complex from 1900, Cell 6, now had a large area of greater than 50 dBZ reflectivity at 0.5 km AGL. There was also a well-defined notch on its eastern flank, suggesting strong near-surface inflow. It was around this time that the storm exhibited characteristics of a supercell, including being single-cellular, having mid-level rotation (as indicated by Doppler velocity data), having a low-level reflectivity notch, and having a Weak Echo Region (WER). This similarity to a supercell will be discussed in more detail later.

Between 1932 and 2001 MDT, the weak northern cell (Cell 8) dissipated, and the main cell (Cell 6) split into two main reflectivity cores, a northern one (Cell 9) and a southern one (Cell 6). Because the storm was moving mostly southward during this period, the southernmost cell would be considered the "right-mover", and the northernmost offshoot the "left-mover". This kind of storm splitting is typical of supercells (Weisman and Klemp, 1982, 1984), and usually the right-mover survives because the storm dynamics forced by the ambient shear profile favors the development of the right-mover and the dissipation of the left-mover. Similar behavior was observed in this case. By 2001 MDT (Figure 4.2h), the right-mover (Cell 6) was still above 50 dBZ at 0.5 km AGL, but the left-mover (Cell 9) was dissipating. Cell 6 redevelops one last time, but by 2030 MDT (Figure 4.2i) it was well into its dissipating stage. In fact, this storm, which appeared supercellular only a few minutes earlier, dissipated so quickly that radar coverage was terminated after the 2039 MDT volume scan due to a lack of ITF-inferred lightning and because maximum near-surface reflectivities were under 40 dBZ.

Figure 4.3 (a-b) shows a vertical cross-section of reflectivity (Figure 4.3a) and single-Doppler velocity (Figure 4.3b) constructed from the radar volume begun at 1932 MDT. The cross-section is taken along the 45° azimuth. In Figure 4.3a, a Weak Echo Region (WER) is clearly visible at approximately 80 km from CHILL and 2 km AGL. The high reflectivities above this WER are suggestive of a strong updraft in this region suspending large precipitation particles aloft. From Figure 4.3b, strong convergence along this radial exists in the vicinity of the main precipitation shaft. (Negative velocities are toward the radar and positive velocities are away.) The low-level outbound velocities on the radar side of this shaft are suggestive of significant inflow to the WER/updraft region. Note the significant divergence aloft, above the core. The zero velocities in the areas of deleted reflectivity data are a consequence of the K_{dp} calculation program used on the radar data after it has been edited. The program unfortunately sets missing or deleted velocity data values to zero. Note, however, that in Figure 4.3a, the white pixels in the reflectivity core are not due to missing data but instead due to the reflectivities being higher than the given scale can represent. The existence of a WER and the significant mid-level convergence are suggestive of a supercell.

Figure 4.4 (a-b) show a horizontal cross-section of reflectivity (Figure 4.4a) and single-Doppler velocity (Figure 4.4b) at an elevation angle of 3.5° for the radar volume starting at 1932 MDT. As can be seen from Figure 4.3a, the main core of the storm resides along the 45° azimuth, justifying the choice of this azimuth in Figure 4.3. Note that Figure 4.4 uses the same magnification as Figure 4.3, and distances are in km. In the velocity data, there appears to be a pair of cyclonic couplets in the general vicinity of the core. The first resides at a distance of approximately 80 km, at an azimuth just less than 45°. The second

exists at about the same distance, but further to the west along the 40° azimuth, and is more sharply defined than the first. These velocity couplets are suggestive of mid-level (approximately 5 km AGL at this distance and elevation angle) rotation. Such mid-level rotation, known as a mesocyclone, is present in all supercells by definition.

To summarize storm evolution, this storm complex began as a multicellular line, but late in its life it became single-cellular, and even displayed aspects common to supercells. However, this "supercellular" stage was very short-lived, and thus could not be described as quasi-steady. Since longevity and steadiness of strength are requirements for storms to be identified as supercells, this storm probably was not a true supercell during this stage. Thus, it shall be called a "quasi-supercell" at this time. This type of ambiguity in storm classification has been noted by other researchers (e.g., Burgess and Lemon, 1990). In fact, Foote and Frank (1983) have suggested the creation of an intermediate category between multicell and supercell: the Westplains storm. Regardless of what it should be classified as, it is clear that this storm underwent a major transition during its long lifetime, which makes it a prime candidate for study in this thesis.

4.3 Comparison of lightning and bulk precipitation rates

Five-minute IC flash rates from the ITF were calculated following the method outlined in Chapter 3. Five-minute NLDN CG rates also were calculated for this storm complex. The result is Figure 4.5, which shows these rates as functions of time. There are several notable features in this plot. The first is that the entire storm complex, throughout its lifetime, produced relatively few CGs (and the overwhelming majority of these were of negative polarity, so CG rates were not separated into positive and negative CG

components). The peak flash rate was 9 in a 5-minute period, which is not very high (Uman, 1987), especially given the magnitude of this storm as viewed by radar. This peak flash rate occurred near 1805 MDT. Before and after this time, CG rates were quite low, generally varying between 0 and 2 per 5-minute period. After 1835 MDT, CGs were almost nonexistent. Throughout the storm's lifetime, there were several time periods, lasting anywhere from 10 to 30 minutes, where CGs were not produced at all. The most striking examples of these are the periods of 1640-1710 MDT and 1920-1945 MDT. Turning to the ITF data, this second time period coincided with a maximum in the IC flash rate, with IC flash rates during this time often 200 or more per 5-minute period. This is also the time when the storm exhibited the most supercellular characteristics, with mid-level rotation and a Weak Echo Region (WER). Before this time, when the storm complex was more multicellular, IC flash rates were approximately half these peak values. Indeed, between 1810 and 1910 MDT, IC flash rates were remarkably steady, averaging near 20 per minute throughout the hour, with only minor fluctuations. Before 1810, IC rates were much less steady, undergoing two major peaks with a major lull in between. After the IC flash rates reached their maximum values around 1930, they fell off rapidly and then underwent another major surge, centered on 2005 MDT. After this time the IC rates decreased quickly as the final cell in the storm complex (based on radar observations) collapses.

Figure 4.6a shows NLDN CG ground strike locations overlaid on low-level reflectivity for the 1803 MDT volume scan. CGs shown are those that occurred during the volume scan period (approximately 6 minutes in duration). Note that from Fig. 4.5, this time period nearly coincided with the CG rate peak for the storm. It is apparent that most of

the CGs were not associated with the most intense cells along the line. Instead, the northernmost cells, which were approaching maturation as their cores descended toward the ground, were producing the most CGs during this time. The southernmost cells are associated with a single positive CG. Figure 4.6b is the same as Fig 4.6a, except for the 1809 MDT volume scan, also a time representative of the storm's peak CG output. The cores of the northernmost cells appeared to have reached the ground, as low-level reflectivities had risen in these cells. The southernmost cells were still intense. Again, most CGs were associated with the weaker cells (in terms of low-level reflectivity), while a single positive CG was associated with the southernmost cells. So it appears that even during the peak CG production period of this storm, CGs were associated with cells just reaching maturation, not with the most intense cells along the line.

Figures 4.7a and 4.7b are similar to Figures 4.6a and 4.6b, respectively, except that mean horizontal positions of ITF ICs are plotted instead of NLDN ground strike locations. It is clear that the more intense southern cells are producing more ICs than the maturing northern cells.

To gain a better sense of the vertical extent of each cell around this time, Figure 4.8 (a-d) was created. Each plot is a vertical cross-section of reflectivity for the 1809 MDT volume taken along the given distance north of the CHILL radar. Figure 4.8a is for the northernmost cell in the line from Figure 4.7, Figure 4.8b is for the next cell to the south, and so on through Figure 4.8d, which is for the southernmost cell along the line. From Figure 4.8 it is apparent that, although the vertical extents of the 30 dBZ contours for all cells are similar (approximately 10.5 km AGL or slightly greater), the vertical extents of the 50 dBZ contours for the two southernmost cells, the ones which produced very few

CGs around this time, are much greater than the northern two cells, which accounted for most of the CGs. The low-CG cells show 50 dBZ up to 6 km AGL or more, whereas the CG-producing cells either lack 50 dBZ altogether (as in Figure 4.8b), or it extends to a significantly lower altitude (4 km in Figure 4.8a). This is strong evidence that the low-CG cells were much more intense than CG-producing ones, and that the internal structures of the two types of cells were different, even though both cell types extended to similar heights. Thus, throughout the lifetime of this storm, very few CGs can be attributed to the most intense cell(s) at any specific time.

Using the methods detailed in Chapter 2, low-level (0.5 km AGL) rain and hail mass fluxes were calculated for each CHILL radar volume obtained during this storm. Total radar-inferred precipitation mass fluxes, along with 5-minute ITF IC flash rates, are plotted versus time in Figure 4.9. Note that these values are for the entire storm *complex*, not any individual cell. ITF IC rates are plotted at the start of each 5-minute period, and total mass fluxes are plotted at the start of each volume scan. Note that this mass flux includes both rain and hail. Following the method of Chapter 2, these rates were determined separately for each precipitation type, then were added together to create Figure 4.9. Recall that the ITF IC flash rates exclude all flashes lasting less than 1 ms.

Before any trends are inferred from this figure, it is important to note two times when radar volume scan coverage was opened up to the west to include more storm-associated cells that were in their developing stages. These times were 1751 MDT and 1907 MDT. For several minutes before these times, precipitation rates are artificially low because the radar was not scanning the entire storm complex, but not excessively low since the excluded cells were still in their developing stages and probably would not have made

major contributions to the total precipitation flux. Thus, the trends around these times are not necessarily corrupted, but the magnitudes of the trends may be misleading. The dip in precipitation flux around 1745 probably is somewhat more severe than it was in reality, because the developing cells to the northwest were not being scanned at this time. Also, the peak that occurs at 1907 is more sharply defined than it should be, because the immediately previous volumes excluded another developing cell to the northwest. Despite these issues, the overall trends should be correct, and there probably is little risk in interpreting them more in terms of storm-related phenomena, rather than the effects of radar scanning strategies.

From Figure 4.9, IC flash rates and near-surface precipitation mass fluxes appear to be highly correlated at times, and at other times the low-level precipitation flux appears to lag the IC flash rate by up to several minutes. The most notable example of the precipitation flux lagging IC flash rate occurs early in the analysis period, when IC flash rate peaks near 1720 MDT and precipitation flux doesn't peak until just before 1730 MDT. Subsequent peaks in IC flash rate and precipitation flux – around 1810, 1825, and 1840 MDT – appear to line up roughly in time. Precipitation flux again lags IC flash rate from roughly 1915 MDT through the end of the observational period. Note, however, that the final peak in the storm's IC flash rate, around 2005 MDT, is associated with a very small peak in the precipitation mass flux. At this time the storm consisted of a single cell, so it is perhaps not surprising that the peak should be smaller than earlier times when there were more cells. Recall that flash rates and precipitation fluxes are for the entire storm *complex*, not just individual cells. The minima in both IC flash rates and precipitation mass flux that occur between 1930 and 2000 MST coincide with the storm splitting, which

was discussed earlier. The final peak in the precipitation flux and flash rate coincides with the right-mover redeveloping while the left-mover dissipated.

Figure 4.10 shows the storm's separate rain and hail mass fluxes as functions of time. This plot was created by separating the contributions of the two classes of hydrometeors to the total precipitation mass flux, as detailed in Chapter 2. By comparing Figures 4.9 and 4.10, it is obvious (and not surprising) that the rain flux contributes the most to the total precipitation mass flux, with the hail contribution approximately one-tenth the rain contribution. Thus, no further discussion of the rain flux trends will be presented since these trends are nearly identical to the total precipitation flux trends, which have already been discussed. Turning to the hail flux trends, it is apparent that they are more variable than the rain (and hence total precipitation flux) trends. However, the hail fluxes are still relatively well-correlated with the rain fluxes, with some exceptions. The major exception occurs just after 2000 MDT, when the rain flux achieves its last major peak, but the hail flux is at a minimum. Also, the relative amplitudes of the hail and rain maxima and minima do not match well. For example, a minor, perhaps insignificant (in terms of radar estimation error) peak in rain flux at1827 MDT is coincident with a relatively sharp peak in hail flux.

By comparing Figures 4.9 and 4.10, it can be seen that IC flash rates and low-level hail fluxes are well correlated, though there is a tendency for the low-level hail flux to lag the IC flash rate at times, especially near the beginning and end of radar coverage.

Recall, however, that rainfall estimates are subject to at least a 10-20% error, and hail rate estimates are subject to errors on the order of 50%, possibly more. Thus, some of the

smaller peaks and troughs in the flux plots are likely within the error bars of this analysis, though it is interesting that the variations still trend the IC flash rate well.

This precipitation flux calculation algorithm was compared with the one described by Carey and Rutledge (1997), to gain a better sense of how it compares to that technique. The method of Carey and Rutledge (1997) was applied to flux calculations for all volumes from the Kimball storm and compared to the present study's method in Figure 4.11, which shows the time history of total precipitation flux at 0.5 km AGL according to each method. Note that both algorithms use the same methods to calculate hail fluxes, but their rain flux calculation techniques differ. Carey and Rutledge (1997) utilize Z_{dr} as well as K_{dp} and reflectivity, whereas our method uses only the latter two. It is apparent that Carey's and Rutledge's method almost always produced higher rain (and hence higher precipitation) fluxes than this method. Going back to Figure 4.10, the periods of greatest disagreement tend to coincide with the periods of greatest hail flux. In addition, during the approximately 20-minute period after 1900 MDT when agreement between the two methods is best, hail fluxes are low. This is consistent with hail contamination if the reflectivity field, upon which rain rate calculations based on Z_h and Z_{dr} critically depend, is affected by the presence of hail. Carey and Rutledge (1997) used the results of Golestani et al. (1989) to correct these calculations for hail contamination, but based on this simple comparison, it appears that this method still may be subject to significant hail contamination in certain cases.

4.4 Identification of bulk precipitation types

Following the method outlined in Chapter 2, bulk hydrometeor identification was performed on each radar volume from this storm. To review, the following categories of bulk hydrometeors below the freezing level are identified by the algorithm: small (< 2 cm) wet (i.e., melting) hail, small wet hail mixed with rain, large (≥ 2 cm) wet hail, large wet hail mixed with rain, and rain alone. See Table 2.3 for a synopsis of the hydrometeor identification matrix.

Based on the afternoon (1450 MDT) CLASS sounding launched from the Fort Morgan airport on this day, the freezing level was determined to be 3.29 km AGL (where AGL is defined from the elevation of the CHILL radar - 1432 m MSL).

As mentioned in Chapter 2, the algorithm makes use of a reflectivity gradient threshold to avoid the possibility of Z_{dr} bias in the gridded data. This threshold eliminates from consideration those grid points that have excessive reflectivity gradients. This threshold was set at some typical reflectivity gradients values - 10, 15, and 20 dBZ km^{-1}. Additionally, sensitivity tests were performed in order to better estimate the proper threshold setting. For this storm, it was found that the most grid points (below the freezing level) fell under the category of small hail. Figure 4.12 shows the time history of the volume of small hail below the freezing level, as determined using the three different thresholds, for the 10 July storm. Clearly, agreement is superb between the different runs, except for some minor discrepancies at a few times. However, due to the possible errors in this estimation method, these differences are probably insignificant. Regardless, the most restrictive reflectivity gradient, 10 dBZ km^{-1}, was used in further analysis. This more restrictive threshold is also appropriate because of the long range to the storm throughout

the observational period, as estimation errors caused by reflectivity gradients are more likely to occur at farther ranges.

Figure 4.13 shows the volume of small wet (i.e., melting) hail alone (i.e., not mixed with rain) below the freezing level as a function of time for this storm. Note that, although the relative magnitudes of the minima and maxima are different, the volume of small hail below the freezing level very closely trends the low-level radar-inferred hail flux in Figure 4.10. Figure 4.14 shows time histories of the volumes of small hail mixed with rain and rain only, below the freezing level. These volumes are much lower than the volumes of small hail only, suggesting that most of the significant precipitation below the freezing level is small hail. Large hail, and large hail mixed with rain, were not detected by the algorithm. Again, although the relative magnitudes are different, in general the peaks and troughs in small hail mixed with rain match up well with the peaks and troughs in small hail only. The rain-only volume trend does not line up well with either of these trends, but the rain-only volume is quite low, so whether any significance should be given to its trend is uncertain.

Figure 4.15 shows radar-inferred areal coverage at 0.5 km AGL for small hail, small hail mixed with rain, and rain. Interestingly, here the overall trends in the areas of small hail only and rain only match up better than the trends in small hail only and small hail mixed with rain.

In order to better understand the sensitivity of this precipitation identification algorithm to changes in category requirements, some tests were performed on a single volume, 1726 MDT. At this time the small hail category is at its peak, both in volume below the freezing level (167 km^3) and areal coverage at 0.5 km AGL (19.5 km^2). The K_{dp} threshold

to determine between regions of hail only, and regions of hail and rain, is 0.5 ° km^{-1}. This threshold was lowered to 0.25 ° km^{-1}. The result was that a significant portion of the small hail category was shifted over to the small hail and rain category. The volume of small hail below the freezing level dropped to 123 km^3, while the volume of small hail mixed with rain grew from 20.5 to 52.5 km^3. A similar trend was seen in the areal coverage of the two categories at 0.5 km AGL. This suggests that a significant portion of the small hail category may be more properly placed in the small hail and rain category. This would tend to increase agreement between this precipitation identification method and the precipitation flux method of Section 4.3, since the precipitation identification method found most classifiable precipitation areas to be small hail, even though the flux method found significant rain fluxes. However, the precipitation identification algorithm was not rerun for the entire storm using this lower specific differential phase threshold, mainly because it would have not changed the result that there was little or no radar-detectable large hail in this storm, so that small hail accounted for most of the hail fall. This is perhaps the most important result of this precipitation identification study. Due to the subjective nature of the precipitation identification matrix, the strongest trends are probably real, but absolute values should be taken with less faith, as the preceding sensitivity study and comparison with the more quantitative flux method show.

According to the results of Saunders et al. (1991) and Saunders and Brooks (1992), extensive charge separation should not occur during collisions in a wet growth regime, since the rebounding efficiency goes to zero. If one accepts these results, then charge separation may not be very active in the cloud region above the freezing level but below the level of charge reversal (found to range from approximately -10 °C to -20 °C

depending on the laboratory study). This could suppress the development of a lower positive charge region that normally could provoke CG lightning.

The radar data were examined in order to determine whether or not wet growth may have occurred over an extensive region in this storm. Based on several studies (Bringi et al., 1986; Holler et al., 1994; Waterman, 1969), it is believed that LDR values in excess of approximately -26 to -25 dB (at S-band frequencies) above the freezing level may be indications of hail; in particular, hail in a wet growth mode. Note that these enhanced LDR values should be co-located with an extended region of high radar reflectivity (~ 40-50 dBZ or greater) in order to avoid artifacts caused by low signal-to-noise ratios and large reflectivity gradients. These results have been used by researchers (e.g., Kennedy et al., 1997) to identify probable regions of wet growth hail above the freezing level.

In the present study, mid-level elevation angle scans from radar volumes preceding each major peak in the hail flux (1726, 1809, 1827, 1925, and 2019 MDT) were examined for extended regions of enhanced LDR values that could be signatures of wet growth hail. In particular, since the radar volumes were spaced typically on the order of 6 minutes apart, the second to last radar volume before each major flux peak was examined since the high-elevation scans from this volume were spaced on the order of convective time scales (6-10 minutes) from the low-elevation scans (which were the most influential in the hail flux calculations) from the volume occuring during the hail flux peak.

In general, few extended regions of enhanced (i.e., $\geq$ -25 dB) LDR above the freezing level (3.29 km AGL in this case, though it may have been slightly higher inside the storm itself) were found. Sometimes there were a handful of contiguous gates of enhanced LDR that were coincident with a high reflectivity region, but overall no significant signatures

were found, save for the radar volume beginning at 2357 MDT (which preceded the second major hail flux peak at 1809 MDT).

Figure 4.16 (a-b) shows a vertical cross-section of radar reflectivity in dBZ (Figure 4.16a) and LDR in dB (Figure 4.16b) taken along the 50° azimuth in the 2357 MDT volume. This cross-section passes through the northern end of Cell 2 in Figure 4.2. Approximately 95 km from the radar, at a height of approximately 5 km AGL, an elevated high-reflectivity core is centered (indicated by the arrow in Figure 4.16). Co-located with this core is a an extended region of enhanced (-25 dB and greater) LDR. Note that the LDR scale is set such that values less than -26 dB are not displayed. The other regions of enhanced LDR are likely due to low signal-to-noise ratio or reflectivity gradients, but the region of interest probably is real since it is situated in an area of high reflectivity which extended significantly in both the vertical (as seen here) and horizontal (not shown) directions. Peak LDR values approach -21 dB here, though most values range between -25 and -22 dB. Since this core is centered at 5 km, according to the sounding in Figure 4.1 much of it exists above the freezing level, and below the lower limit for the charge revesal temperature (-20 °C). Thus, it appears that, at least at this time, significant wet growth could have been occuring, which may have led to reduced charge separation in the vicinity of the usual location of the lower positive charge region (Williams, 1989).

4.5 Discussion and summary

Given the uncertain and possibly large errors in hail estimation using multiparameter radars like the CHILL, care needs to be taken when interpreting any trends seen in the precipitation data. This is especially true because the storm was far from the radar (> 50

km throughout its lifetime) and multiparameter observations are less reliable at this distance. However, some general observations can be made about this case.

When this storm was in its most supercell-like stage, around 1930 MDT, its IC flash rate was maximum and CGs were not detected by the NLDN. In addition, even when CG rates were modest, after 1800 MDT, the CGs were almost exclusively associated with maturing cells along the multicellular line, not with the most intense cells.

Based on data obtained from the National Weather Service, there was one report of 1 inch (2.5 cm) hail around 2010 MDT. This is near the time the storm complex reached its peak in low-level reflectivity. However, based on the radar data, large hail was likely not present in great quantity with this storm, and most of the precipitation could be described as being small hail, small hail mixed with rain, or rain. Small hail and small hail mixed with rain were present throughout the storm's lifetime, though amounts fluctuated with the growth and decay of individual cells. The trends in the output of small hail, whether alone or mixed with rain, tended to follow the low-level hail flux relatively well - which along with the lack of detected large hail suggests that, when the storm produced hail, it was almost exclusively small (< 2 cm) hail.

IC flash rates and low-level precipitation fluxes (either rain or hail, or both) are well-correlated, though sometimes there is a tendency for the low-level precipitation flux to lag IC flash rate by up to several minutes. Lags between IC flash rates and low-level precipitation fluxes is what would be expected from precipitation-based charging theories. According to these theories, as precipitation develops aloft, charge separation occurs which would lead to IC discharges. As the cores descend, IC discharges should decrease (due to increased distance between the upper positive and lower negative charge centers -

Williams, 1989) and low-level precipitation flux should increase. This is seen in the Kimball storm at certain times, but normally the IC flash rates and low-level precipitation fluxes trend well, with little or no lag. Due to errors in the precipitation estimation method, as well as the IC flash rate calculations, it is unclear how much significance should be placed on the changes in the existence or non-existence of lag between these two trends. Also, these changes in lag times to some extent may be artifacts of the superposition of many cells, all in differing states of growth and decay, since precipitation fluxes and flash rates were for the entire storm complex. What is clear, however, is that correlation between the two trends exists, which is expected based on precipitation-based charging theories.

This correlation also is consistent with the convective theory of cloud electrification (Vonnegut, 1963, 1982; Moore, 1977). According to this theory, strong updrafts should enhance the entrainment and mixing of ambient space charge, while also enhancing precipitation development. Thus, charge separation and subsequent IC flashing still should be correlated to precipitation development in some way, even though according to this theory charge separation need not occur during collisions between precipitation particles.

Thus, to summarize, it is clear that this storm had at least one intense, active cell throughout almost its entire lifetime. It also featured strong enough updrafts to produce at least small hail throughout its lifetime, though such hail production was clearly highly variable. Very low production of CGs occurred throughout this storm's lifetime, but when CGs did occur in (modest) numbers, they were associated with cells of less intensity (based on comparisons of vertical cross-sections of reflectivity), while the most intense

cells favored IC discharges. In addition, at this storm's most intense stage, the quasi-supercellular stage, IC flash rates were maximum and CGs were non-existent. All of these facts are consistent with the elevated dipole hypothesis of MacGorman and Nielsen (1991). The apparently strong updrafts of this storm were perhaps enough to loft the negatively charged core to a higher altitude, so that ICs were preferred over CGs.

However, this does not explain why, when cell updrafts collapsed and the cores approached ground, CGs were not favored over ICs. This is perhaps where the observed high IC flash rates could become important.

The IC flash rate for this storm was relatively high, averaging near 100 flashes or more per 5-minute period for much of the storm's lifetime. It could be possible that these high IC flash rates neutralized most of the charge before it began to descend, so that CGs were not favored even as the cores approached ground.

It appears that, at least around 2357 MDT, significant wet growth of hail and graupel may have occurred. According to the results of Saunders et al. (1991) and Saunders and Brooks (1992), this could have reduced charge separation and suppressed the development (or maintenance) of a lower positive charge region, and thus may have suppressed CG lightning. However, extended regions of possible wet growth were not found at other times. Also, based on the available data, it appears that dry growth (corresponding to reduced LDR values) probably occurred more often than wet growth, due to the paucity of enhanced LDR signatures. Thus, it seems doubtful that wet growth could have significantly affected the charge distribution within this storm.

Radar-inferred precipitation fluxes for this storm are not especially high, considering that all cells in the grid are included in the calculations, and that other severe storms have

exhibited higher fluxes (Carey and Rutledge, 1997). However, for precipitation current to substitute for lightning current, instantaneous precipitation rates may be more important, rather than the area- and time- averaged rates used to calculate the fluxes. However, throughout the storm's lifetime, peak rain rates for each radar volume are almost always below 60 mm hr^{-1}, and do not even exceed 40 mm hr^{-1} in many volumes. Hail rates are similarly low (especially when compared to other severe storms - Carey and Rutledge, 1997). Though these estimates are made from gridded and averaged radar data, it seems likely that, because of the predominance of relatively low precipitation rates throughout the storm's area and lifetime, instantaneous precipitation rates probably were not much higher than the peak values observed in the gridded data. Furthermore, similar precipitation rates can be observed in different storms which produce more CGs. So the precipitation current hypothesis, too, seems unlikely based on the available data.

Thus, based on the available data, a reasonable explanation of the low CG production by this storm would be the following. For many cells in the Kimball storm, strong updrafts loft the negative-charge region to higher altitudes than normal. This tends to favor ICs over CGs. In addition, the strong updrafts also enhance charging and subsequent IC flash rates. The high IC flash rates act to neutralize the separated charge, so that when the updrafts weaken and the cores descend, little charge is available to force CG flashing. This hypothesis appears to be consistent with the available data. However, because the other hypotheses have not been adequately tested, they cannot be ruled out completely.

The implications of these results and inferences will be examined in light of the results of Chapter 5 (the case study of the 12 July storm), and explored further in Chapter 6.

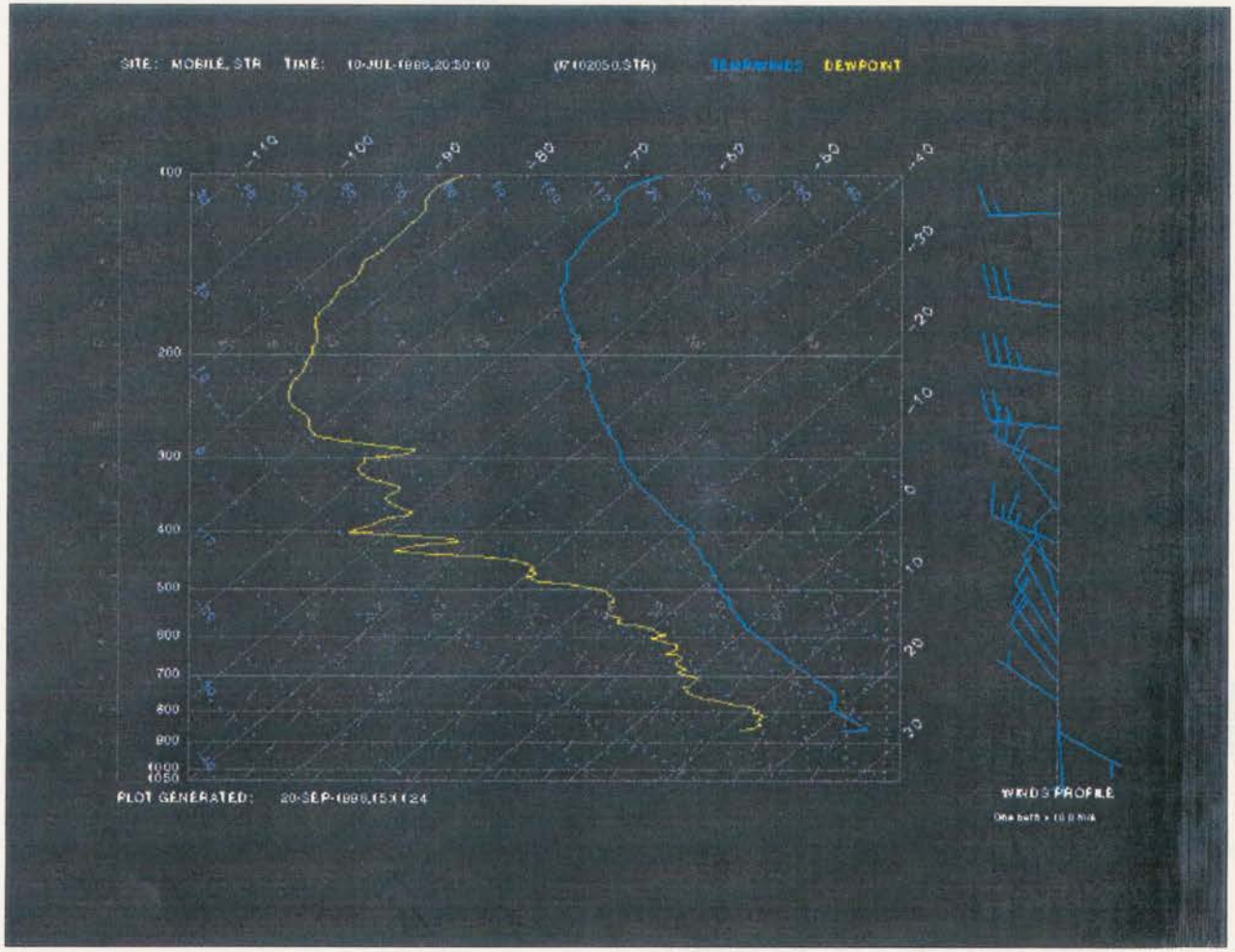

Figure 4.1: Data from the mobile CLASS sounding launched from the Fort Morgan, CO, Airport at 1450 MDT on 10 July 1996. Plotted in skew-T/Log-p format are vertical profiles of temperature, dewpoint, and winds.

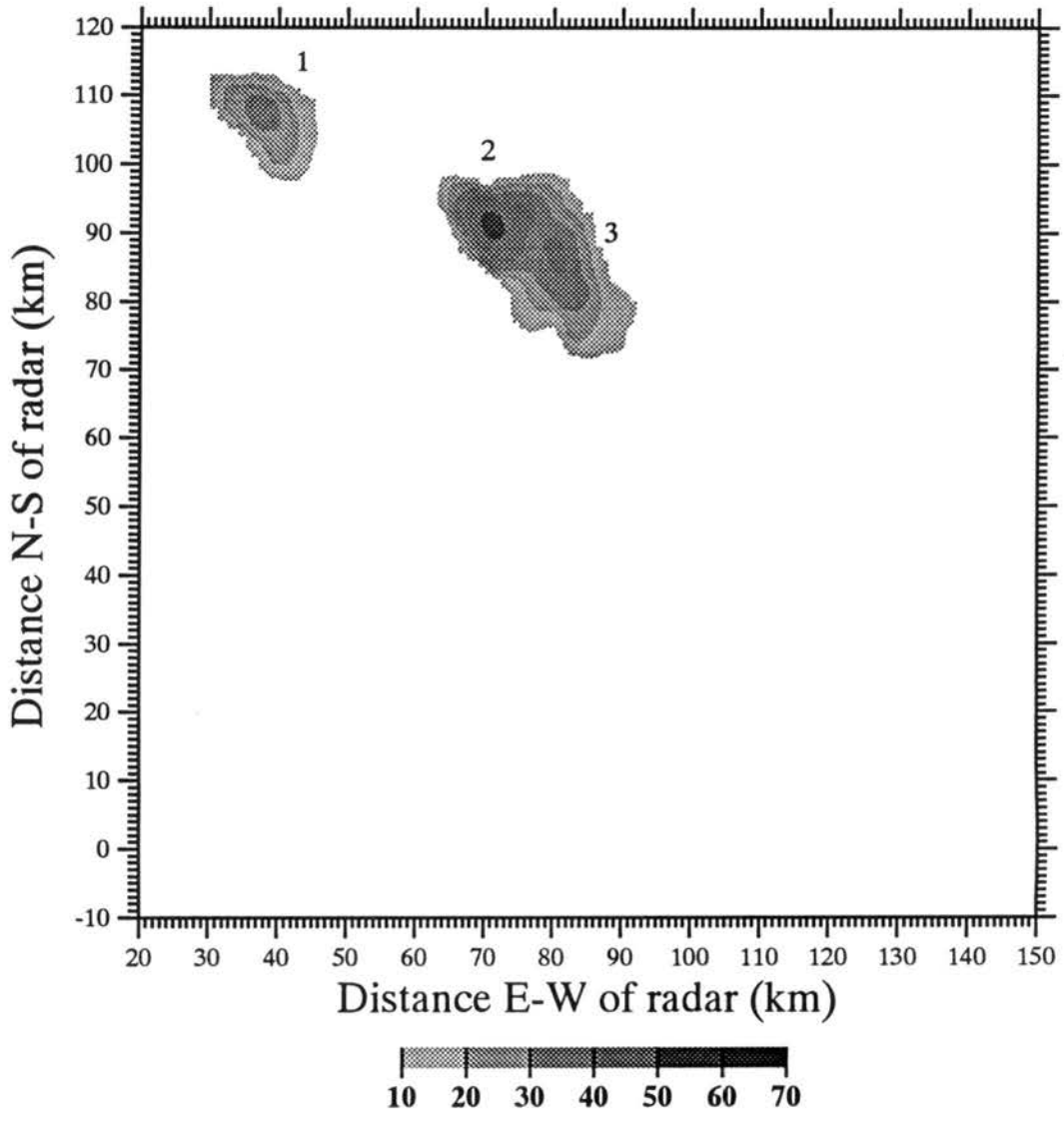

Figure 4.2a: Horizontal cross-section of radar reflectivity (dBZ) at 0.5 km AGL, for 1629 MDT on 10 July 1996.

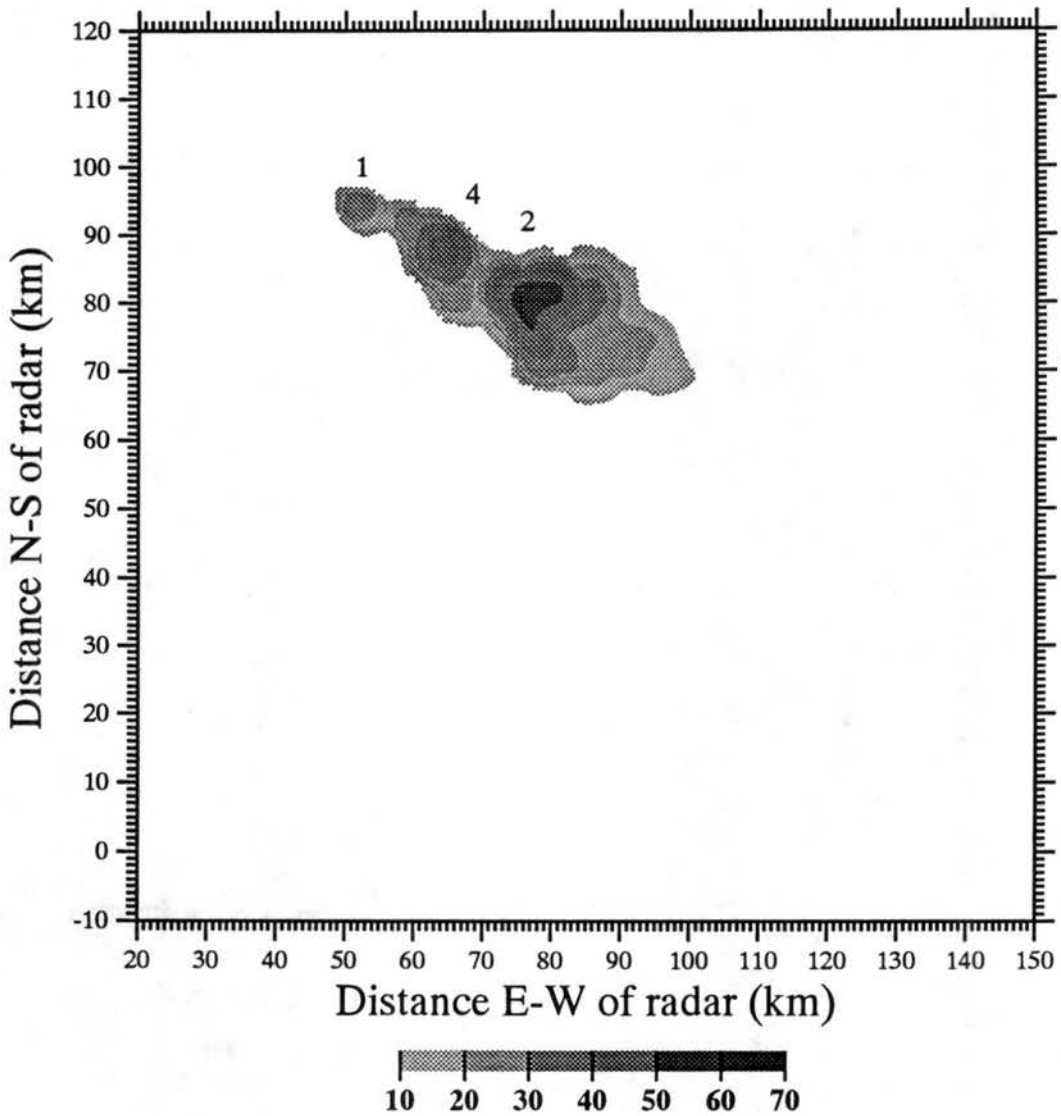

Figure 4.2b: Same as Figure 4.2a except for 1701 MDT.

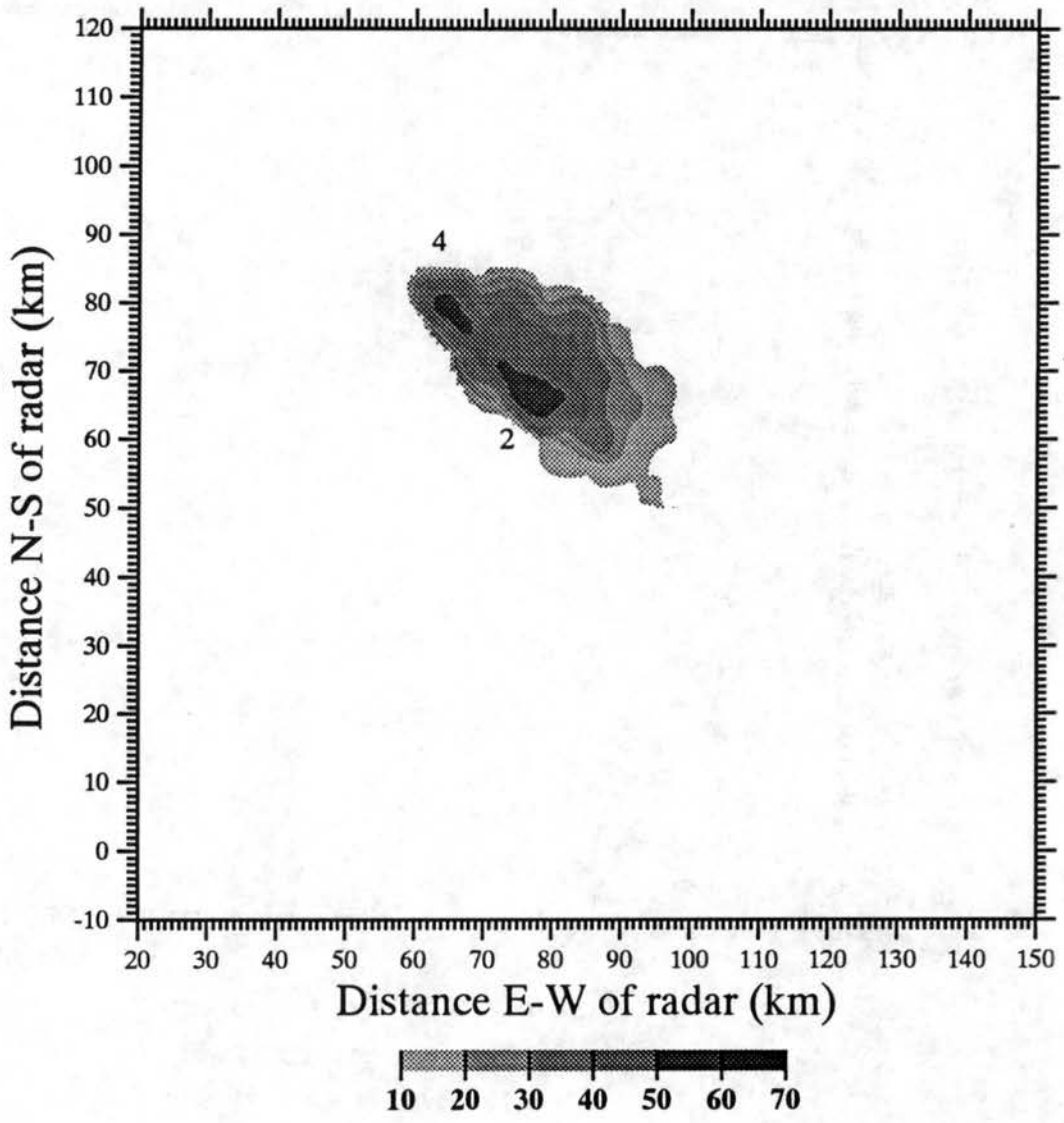

Figure 4.2c: Same as Figure 4.2b except for 1731 MDT.

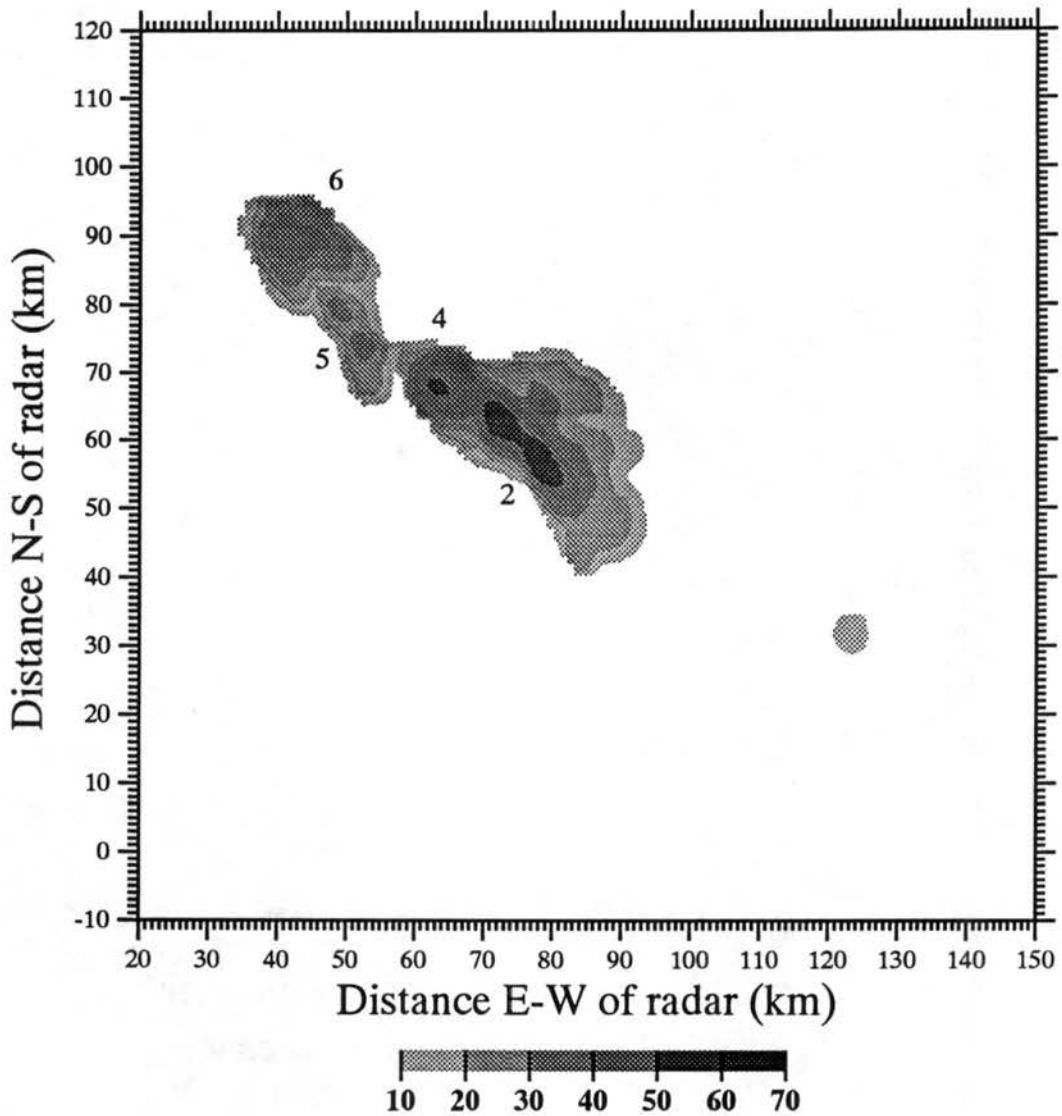

Figure 4.2d: Same as Figure 4.2c except for 1803 MDT.

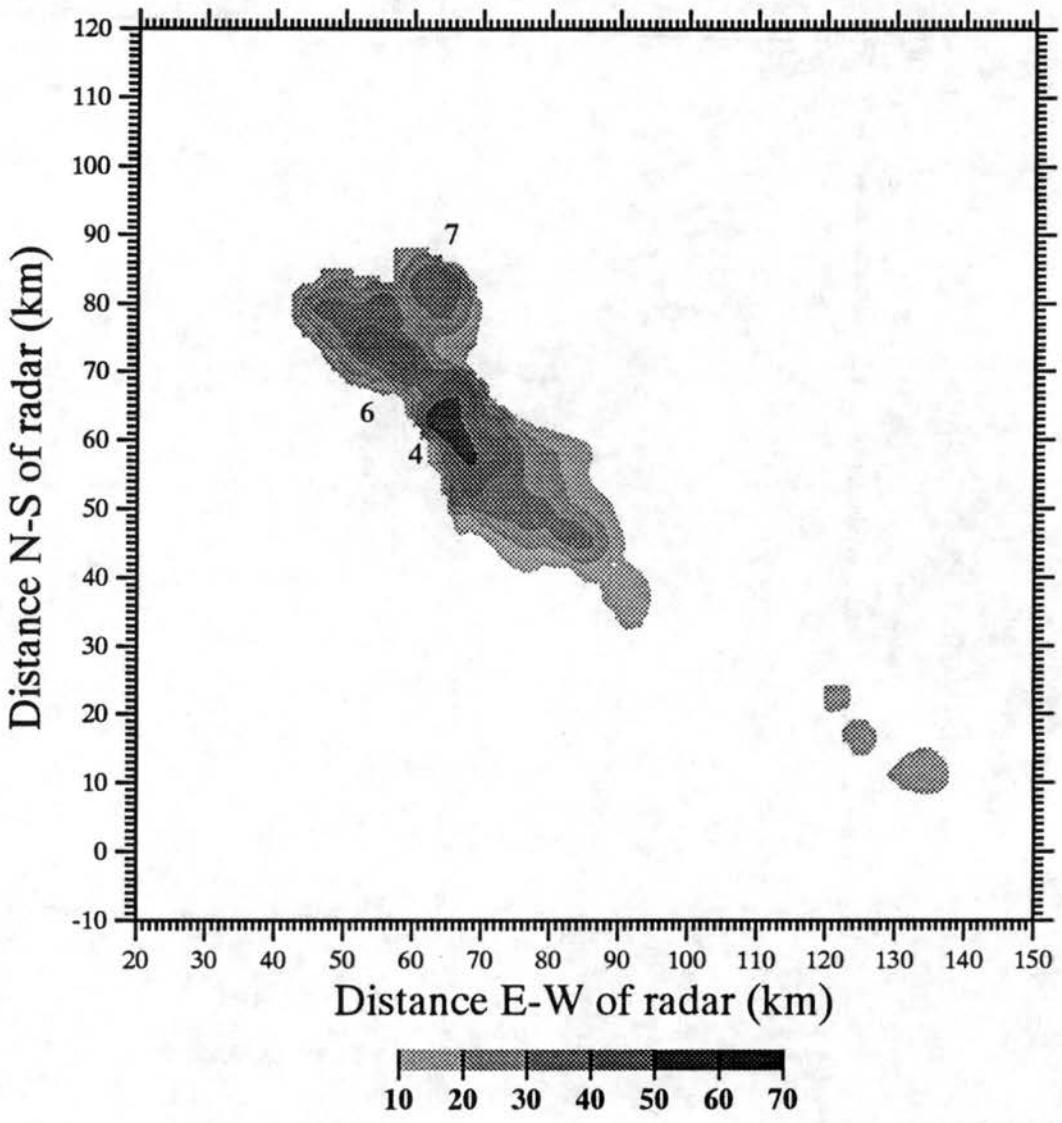

Figure 4.2e: Same as Figure 4.2d except for 1834 MDT.

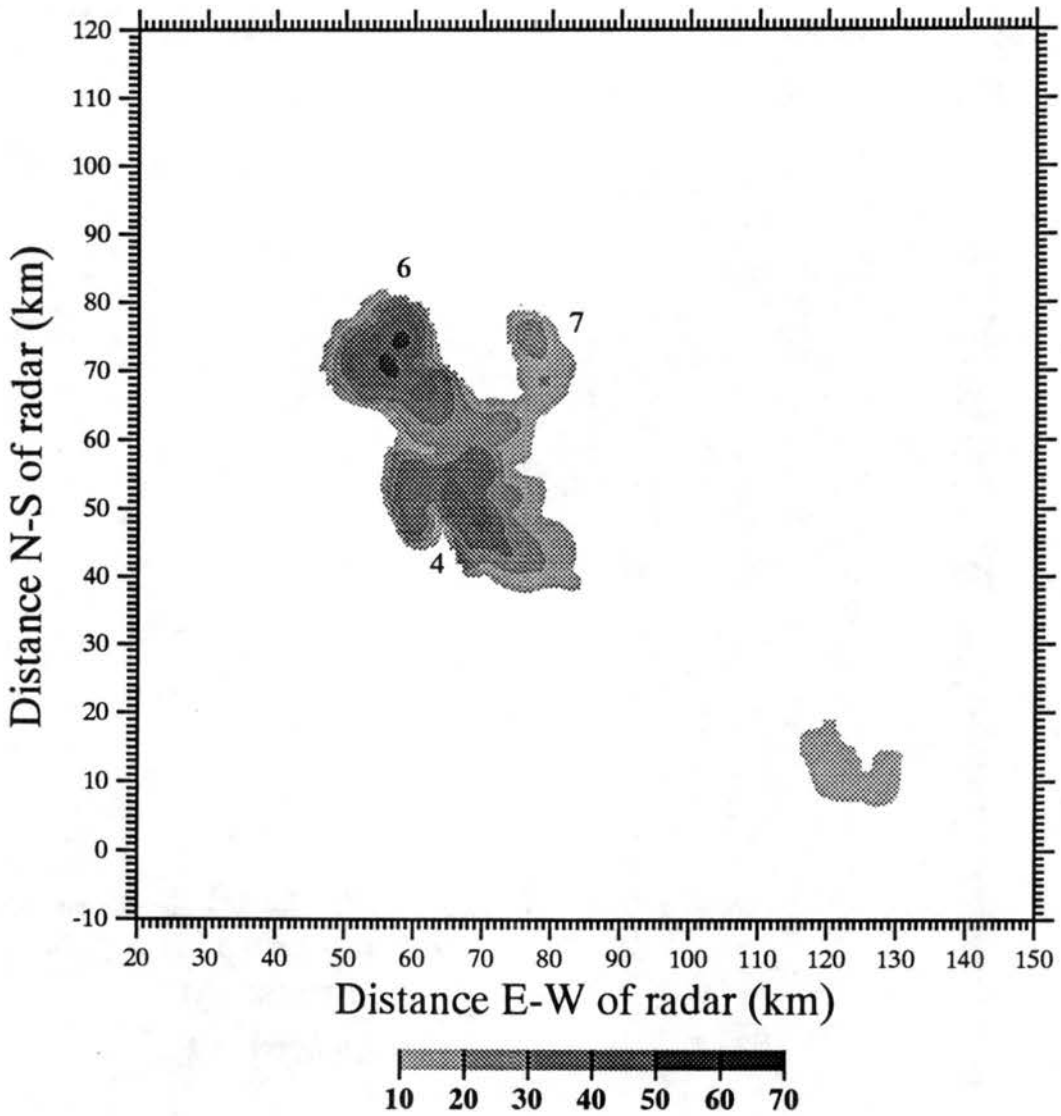

Figure 4.2f: Same as Figure 4.2e except for 1900 MDT.

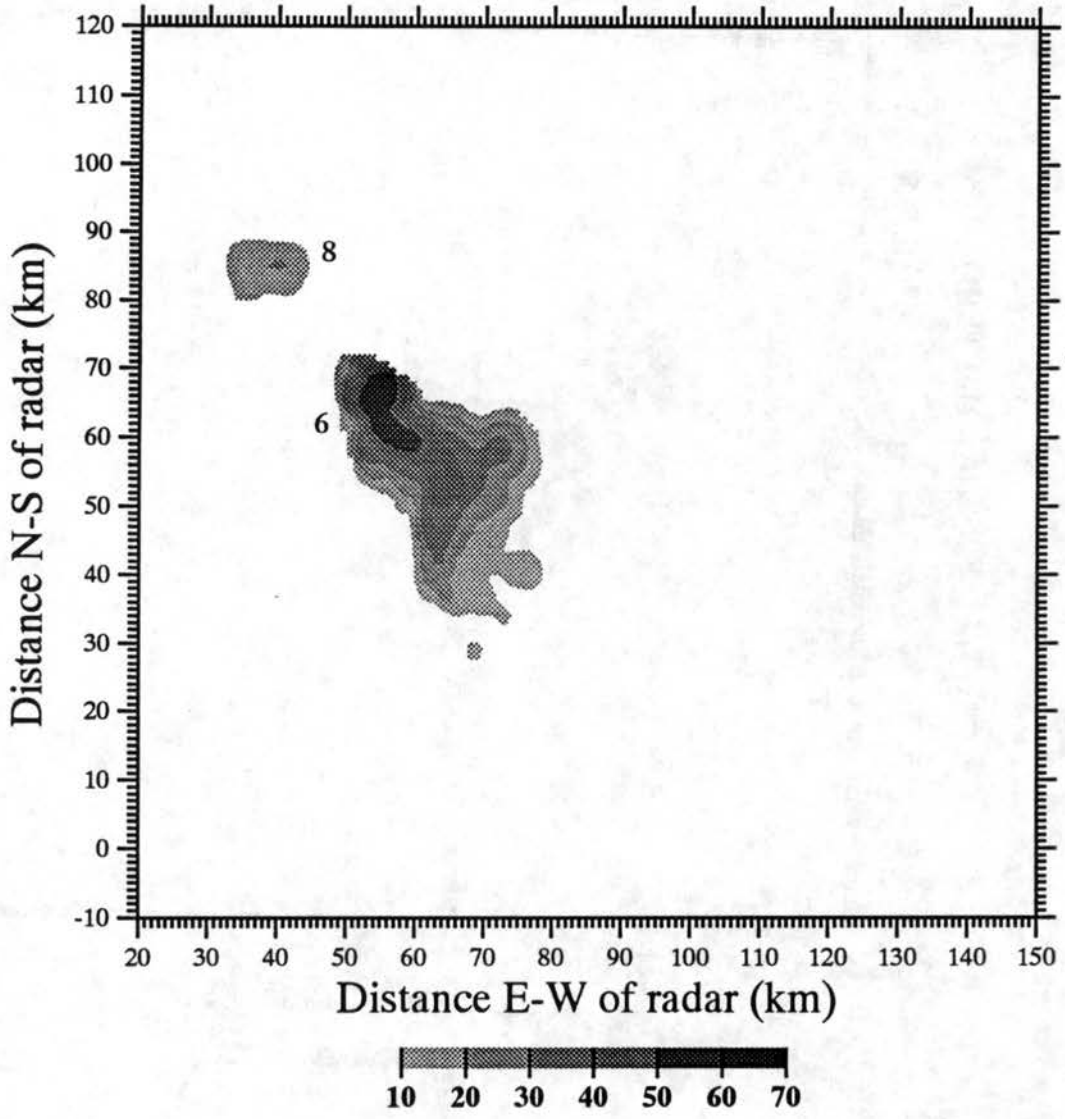

Figure 4.2g: Same as Figure 4.2f except for 1932 MDT.

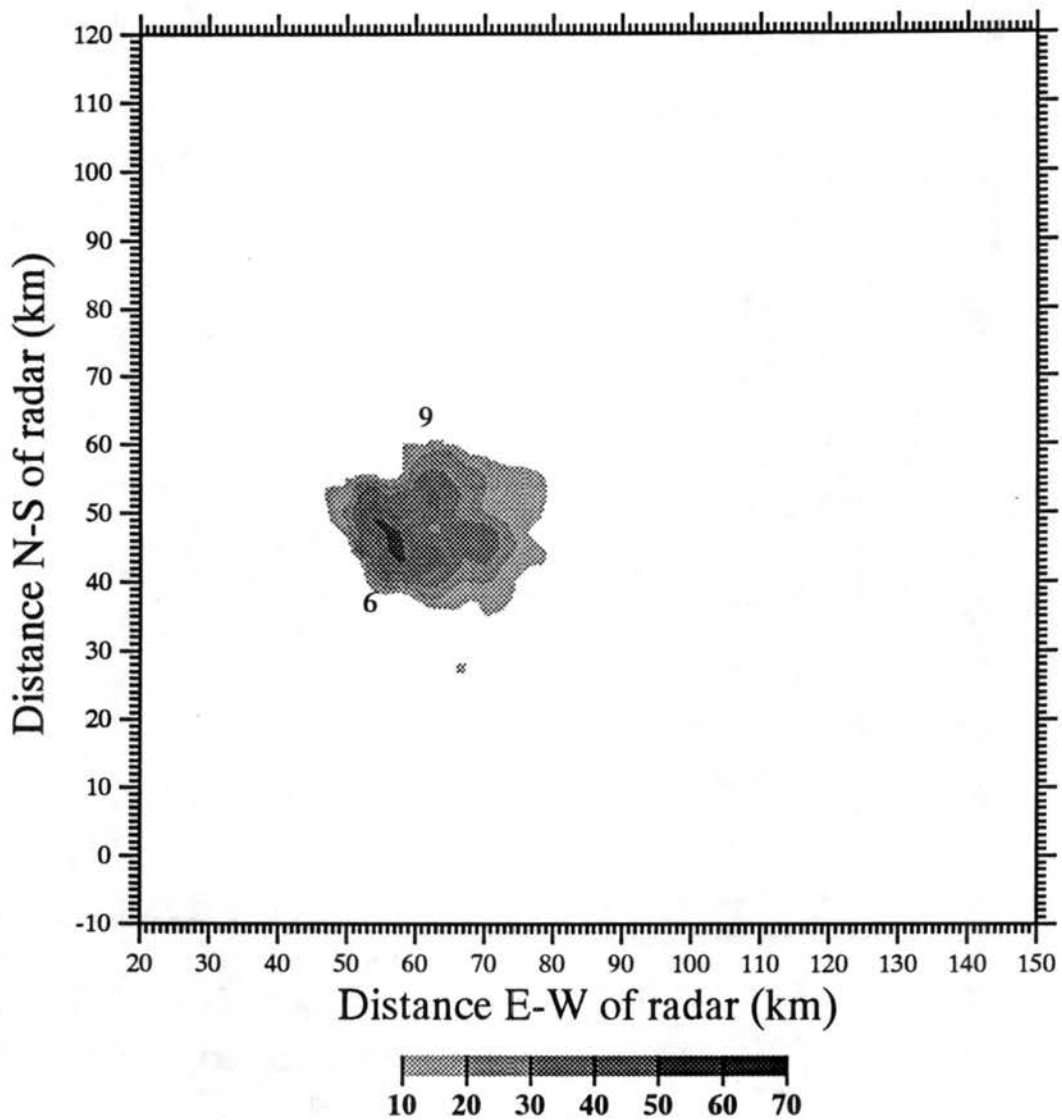

Figure 4.2h: Same as Figure 4.2g except for 2001 MDT.

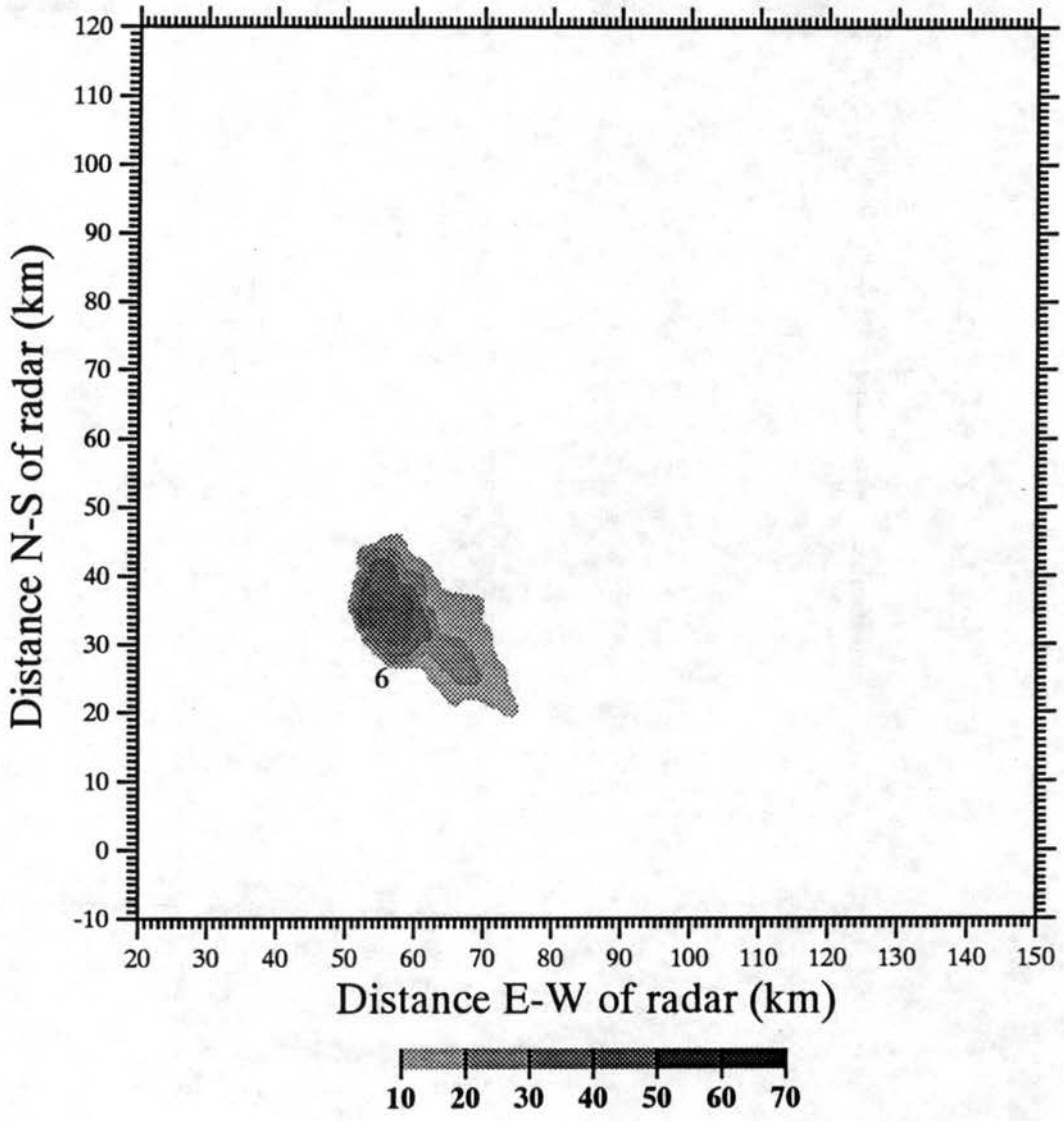

Figure 4.2i: Same as Figure 4.2h except for 2030 MDT.

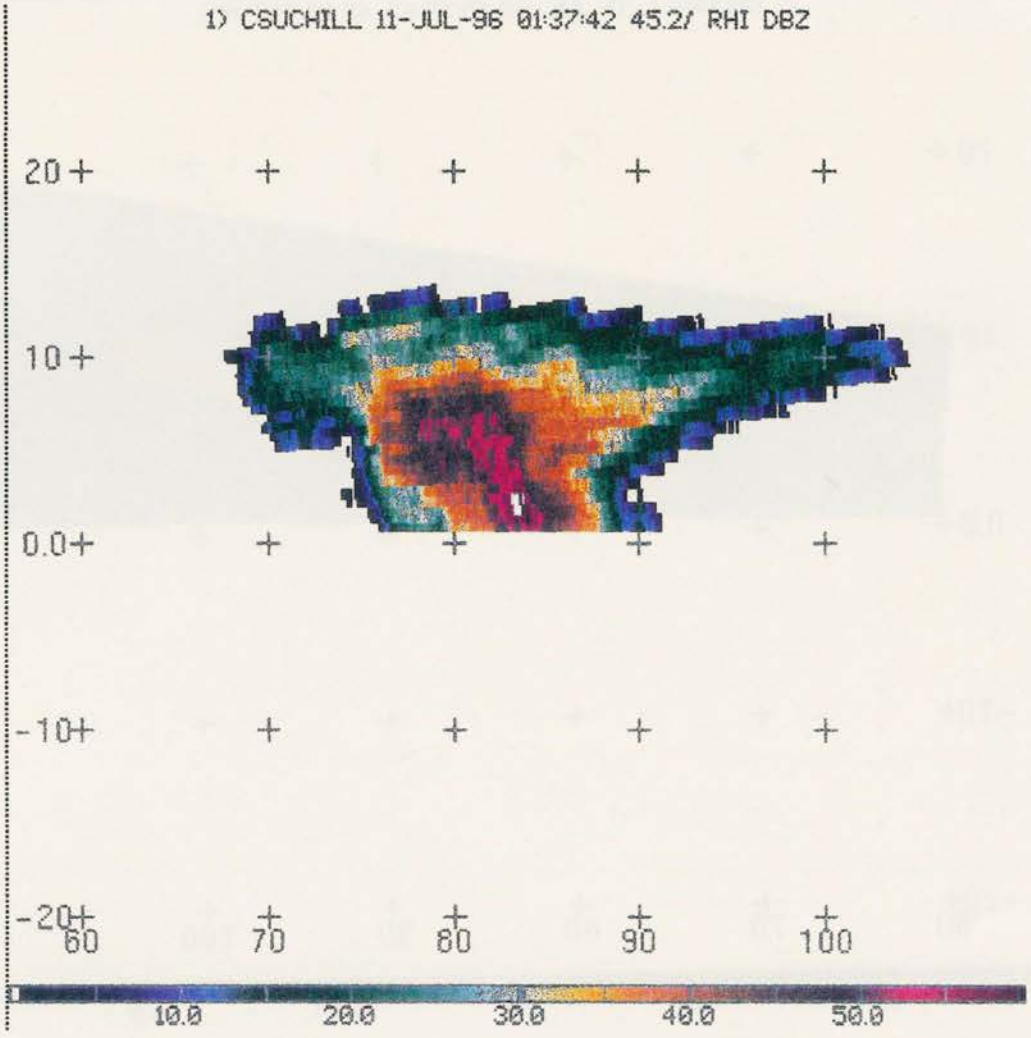

Figure 4.3a: Vertical cross-section of radar reflectivity (dBZ) at 45.2° azimuth, for the radar volume beginning at 1932 MDT. Vertical scale is in km AGL; horizontal scale is in km from the radar.

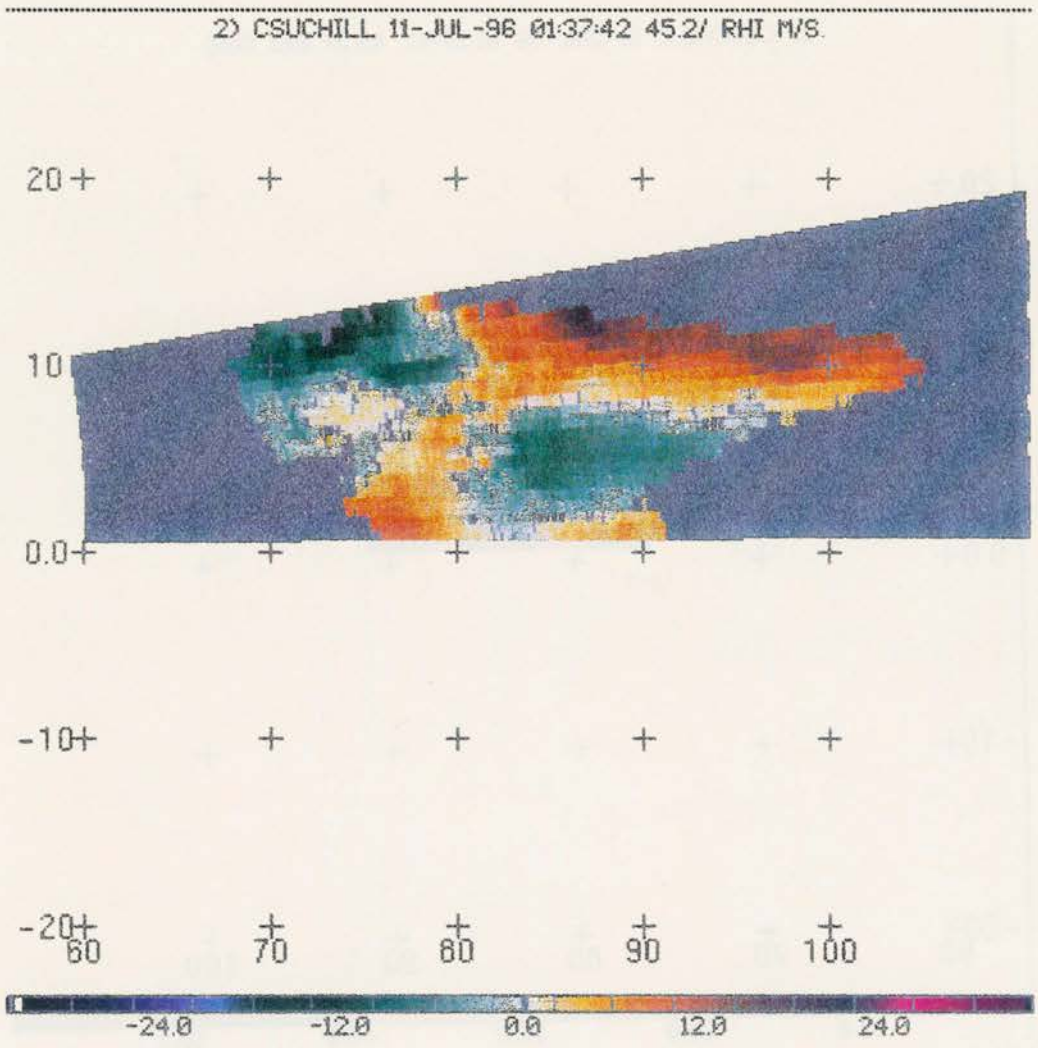

Figure 4.3b: Same as Figure 4.3a except the plotted field is Doppler velocity (m s^{-1}). Negative velocities are toward the radar, positive are away.

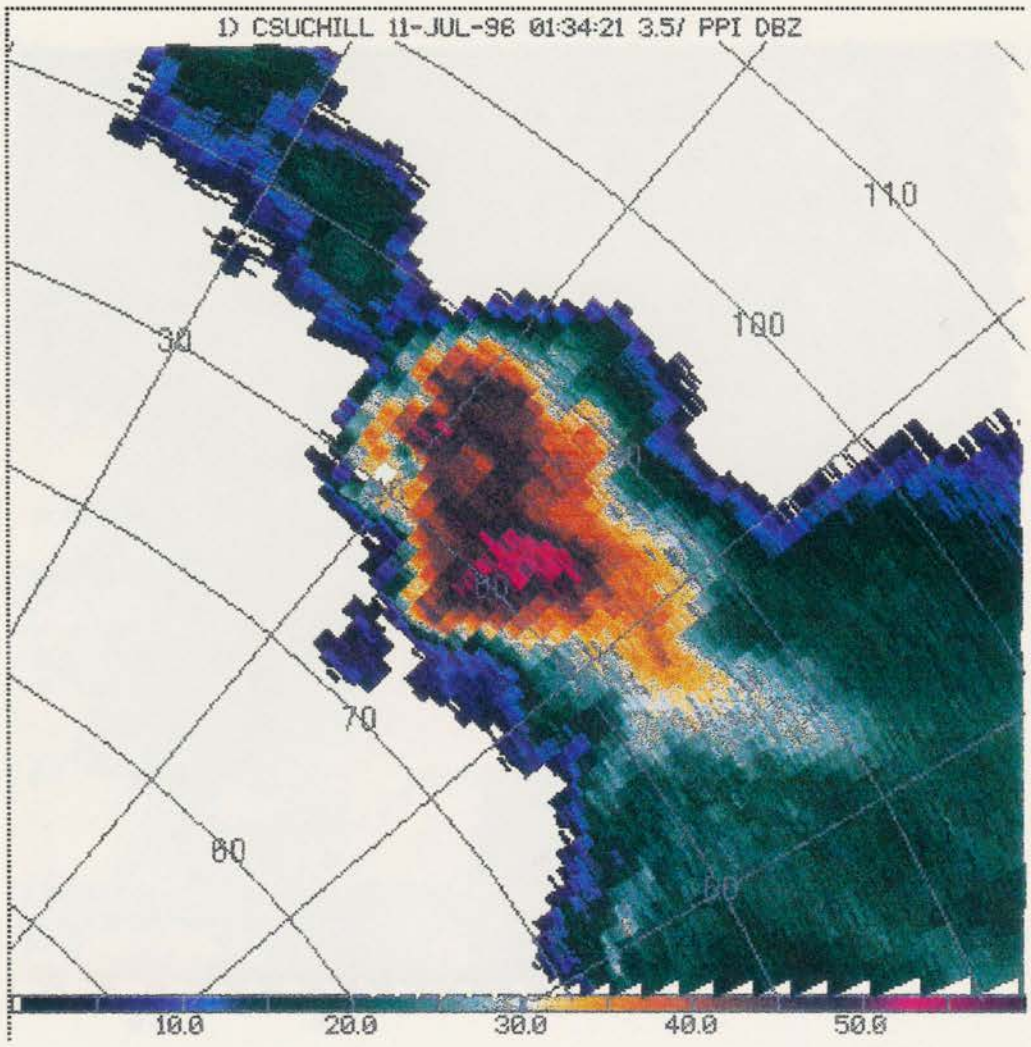

Figure 4.4a: Horizontal sweep of radar reflectivity (dBZ) at 3.5° elevation, from the radar volume beginning at 1932 MDT. Distances are in km and azimuthal angles are in degrees.

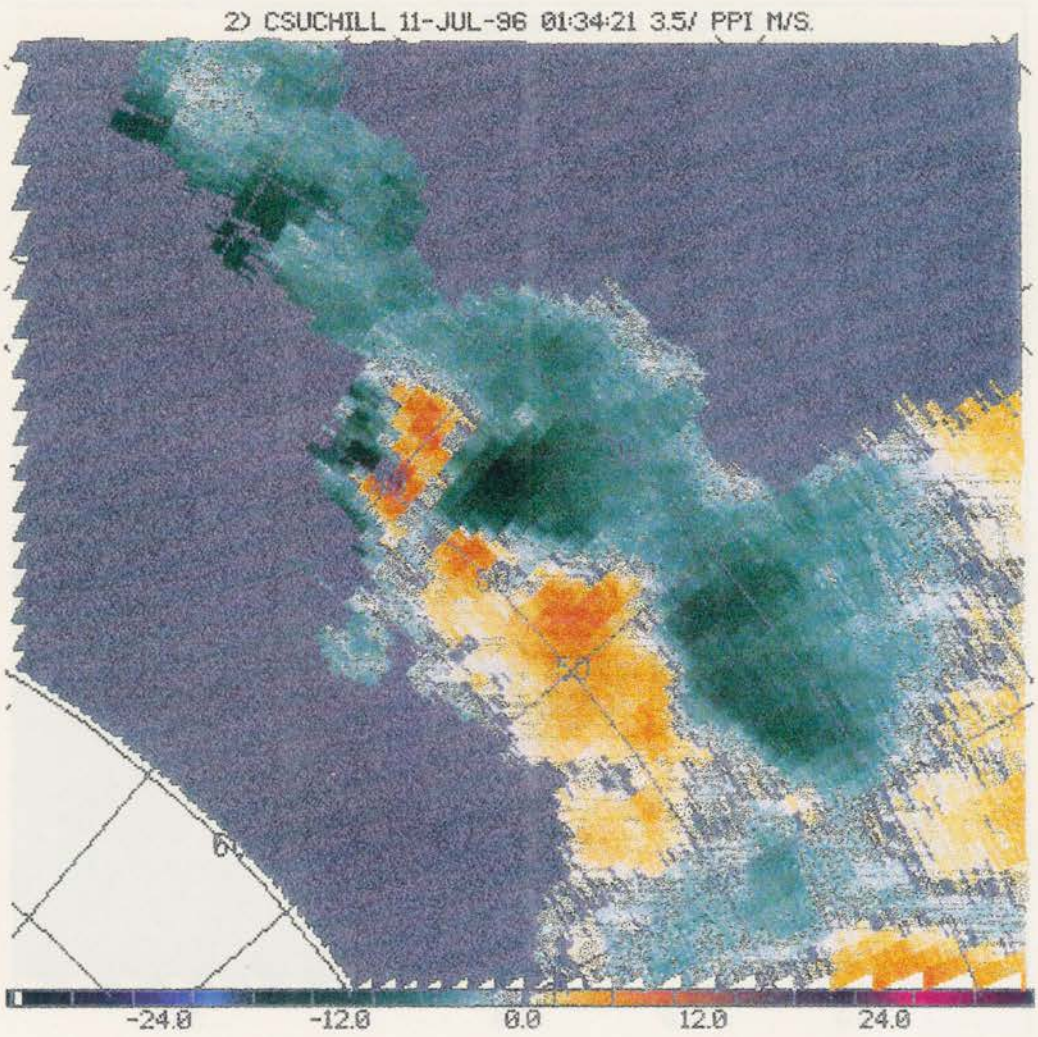

Figure 4.4b: Same as Figure 4.4a except for Doppler velocity (m s^{-1}).

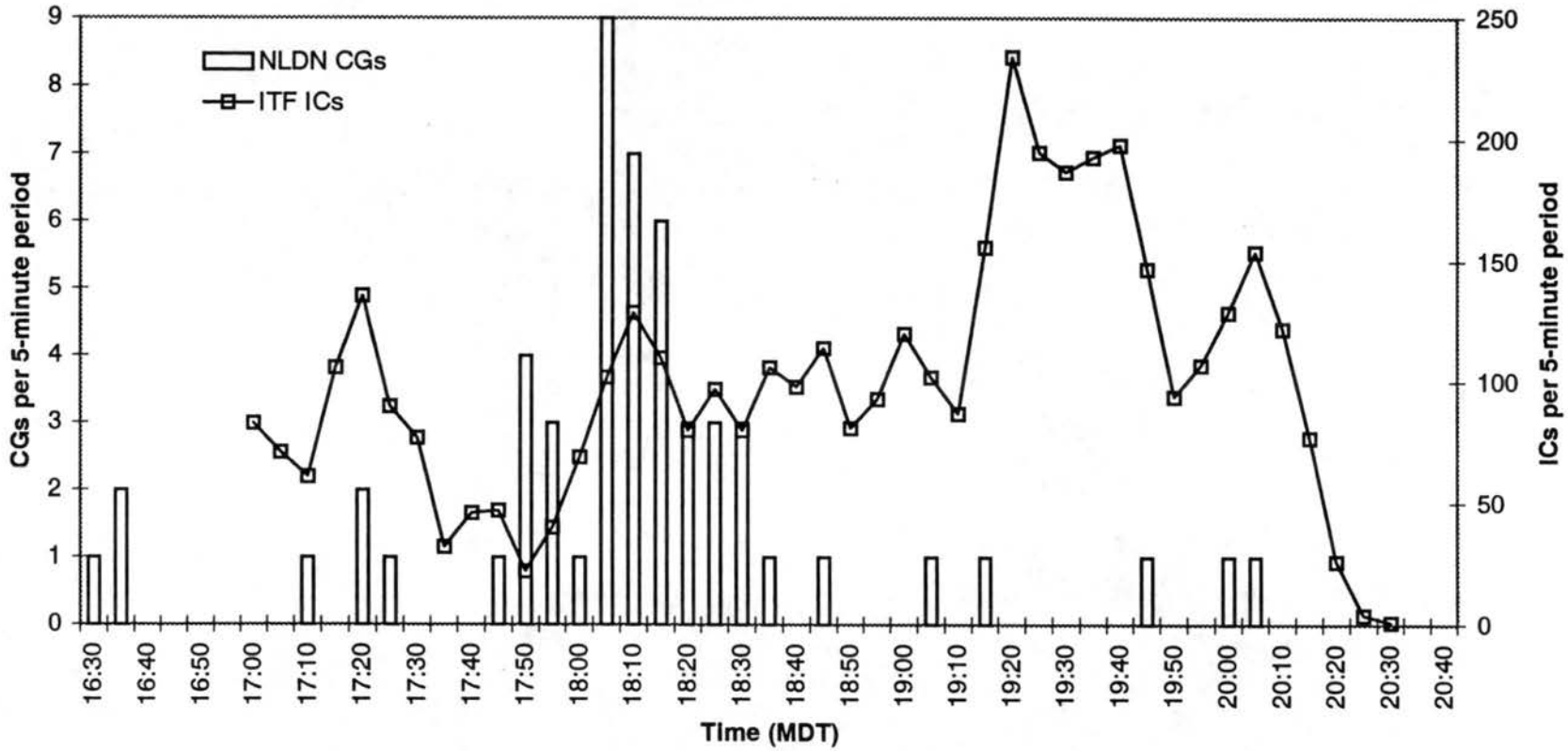

Figure 4.5: 5-minute NLDN CG rates and 5-minute ITF IC rates for the 10 July 1996 storm. Data points are plotted at the start of each 5-minute period.

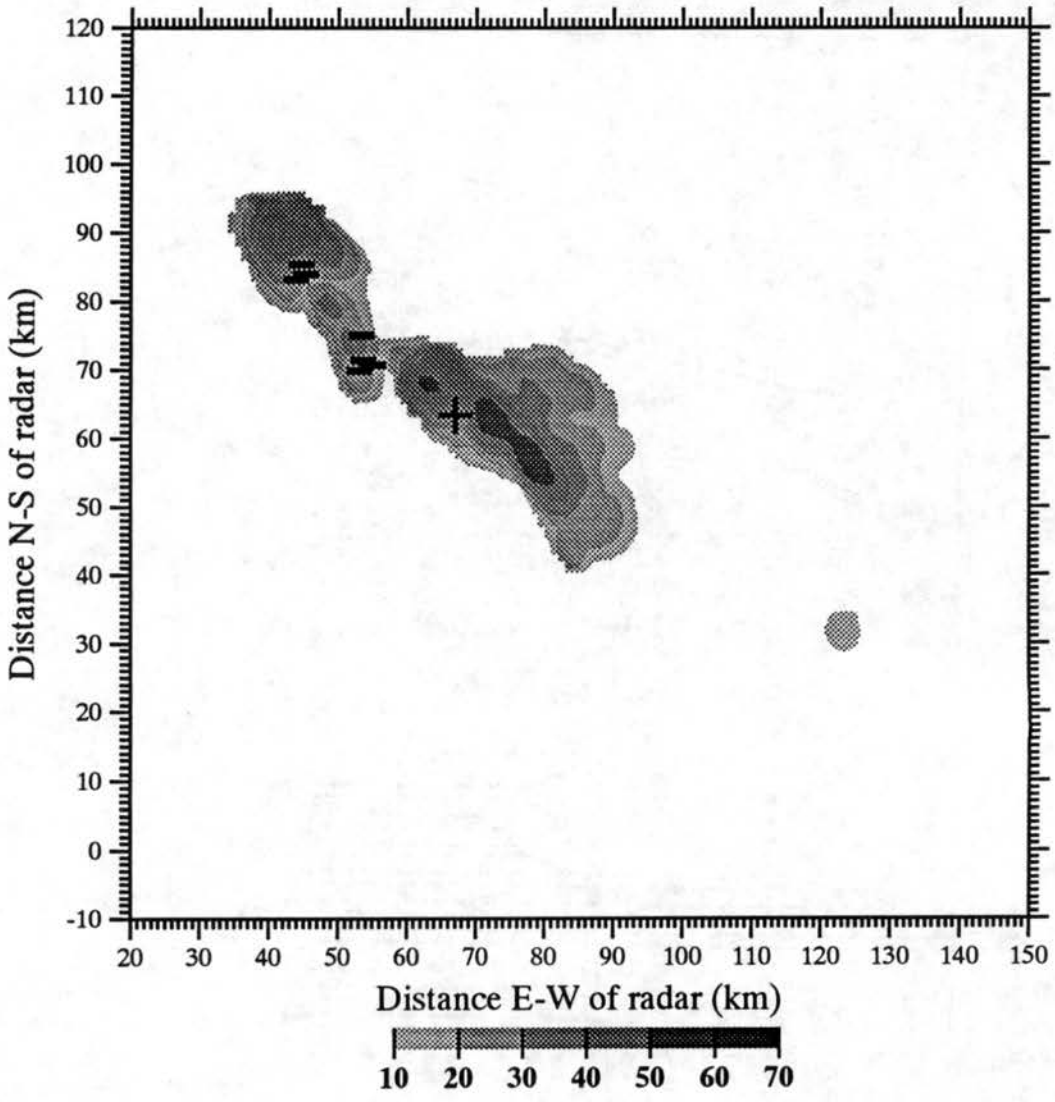

Figure 4.6a: Horizontal cross-section of radar reflectivity (dBZ) at 0.5 km AGL for the 1803 MDT radar volume. Also shown are ground strike locations of all NLDN-detected CG lightning that occurred during the duration of the volume scan. Negative CGs are marked with a minus sign, and positive CGs are marked with a plus sign.

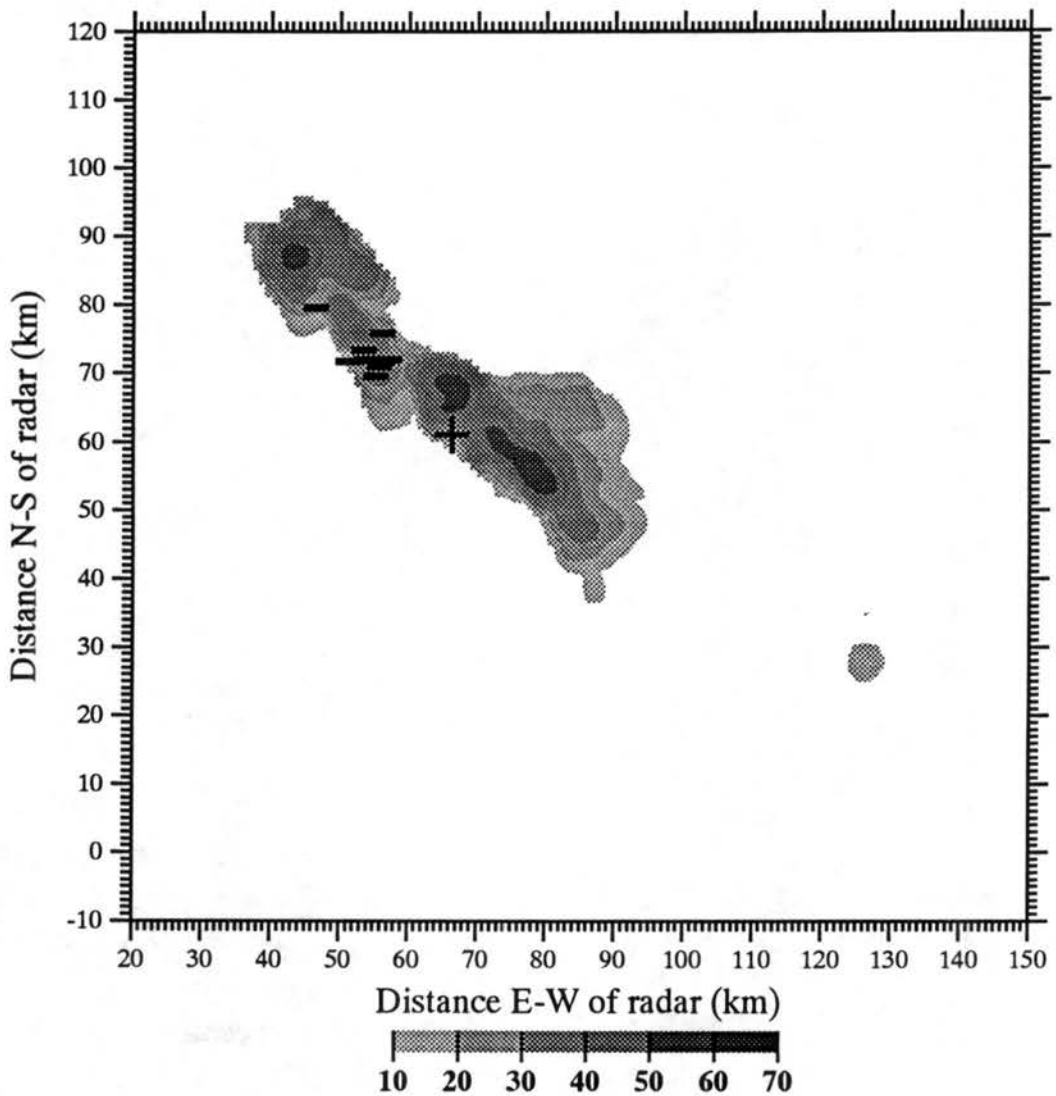

Figure 4.6b: Same as Figure 4.6a except for the 1809 MDT volume scan.

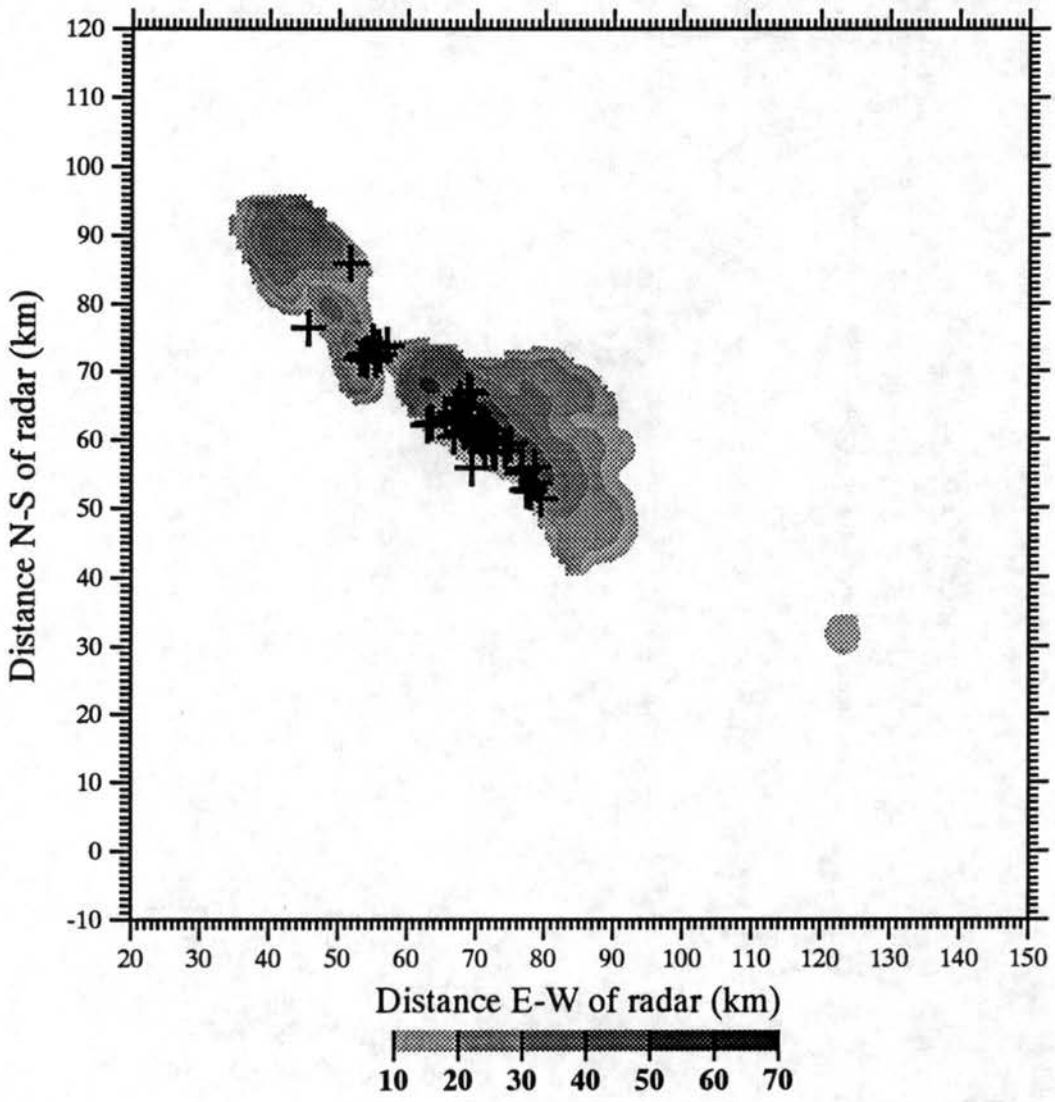

Figure 4.7a: Horizontal cross-section of radar reflectivity (dBZ) at 0.5 km AGL for the 1803 MDT radar volume. Also shown are mean horizontal positions (marked by plus signs) of all ITF-detected IC lightning that occurred during the duration of the volume scan.

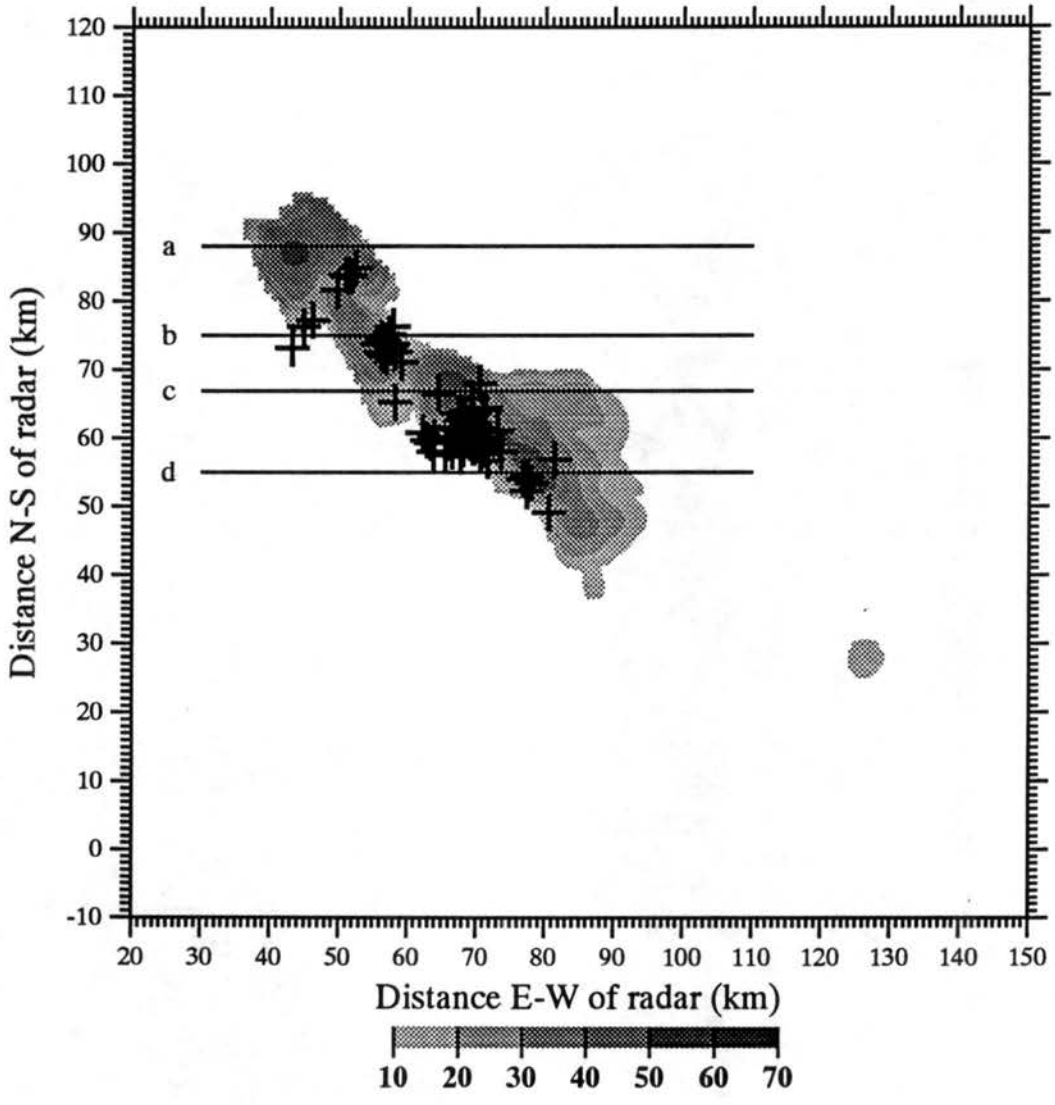

Figure 4.7b: Same as Figure 4.7a except for the 1809 MDT volume scan. Marked by solid lines are the positions of the vertical cross-sections in Figure 4.8 (a-d, respectively).

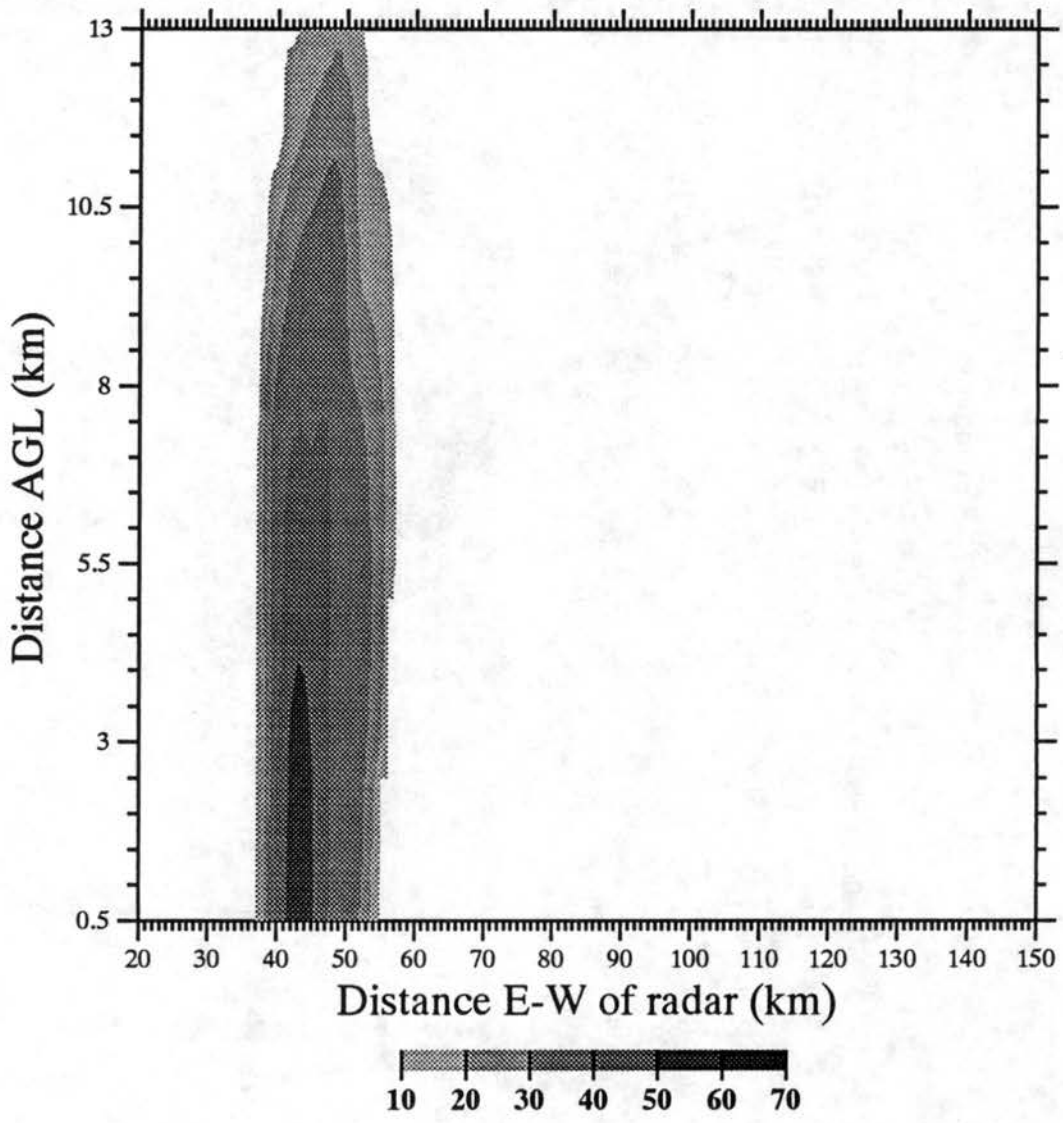

Figure 4.8a: Vertical cross-sections of radar reflectivity (dBZ) at 88 km north of the CHILL radar, for the 1809 MDT volume scan.

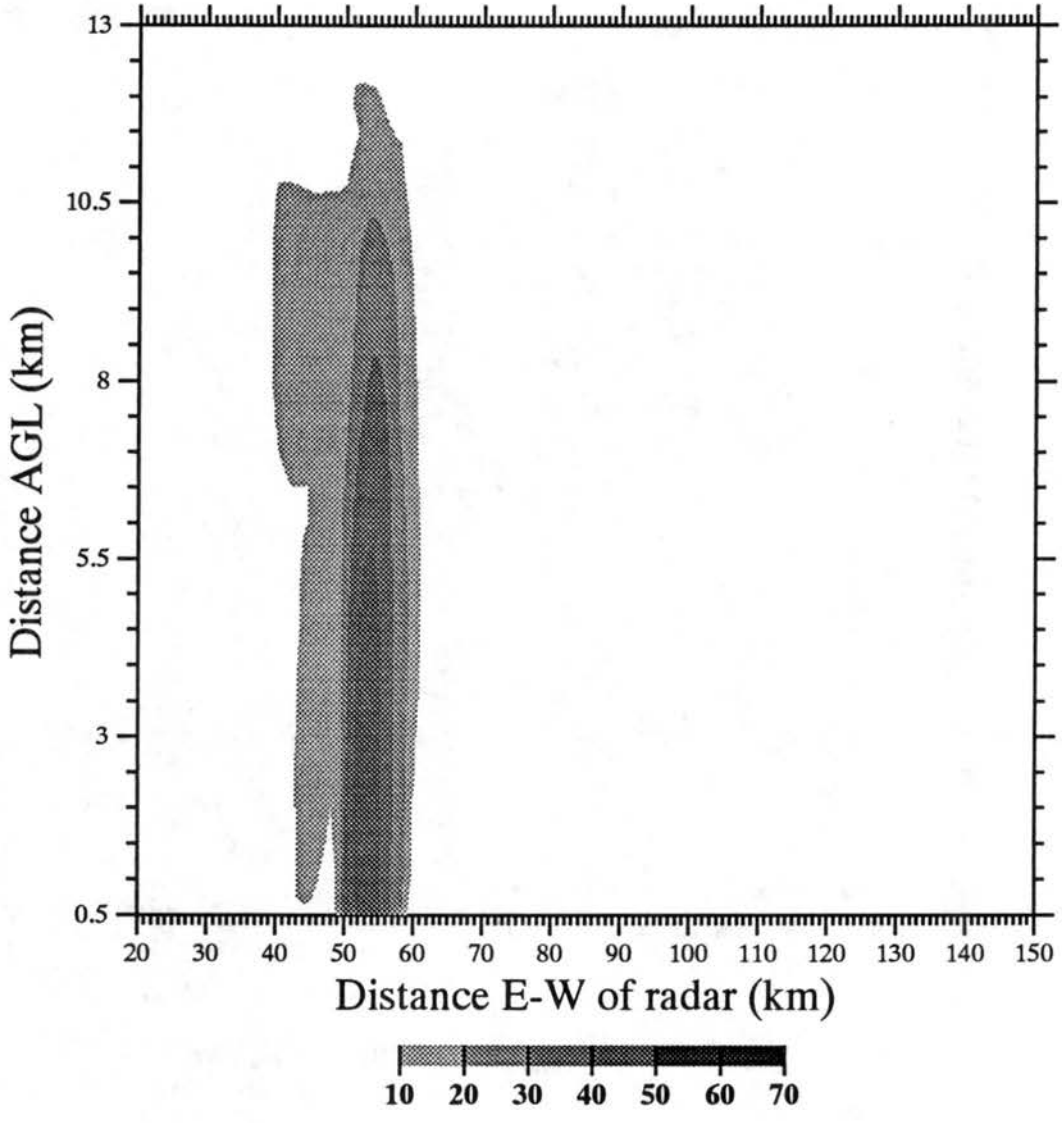

Figure 4.8b: Same as Figure 4.8a except at 75 km north of CHILL.

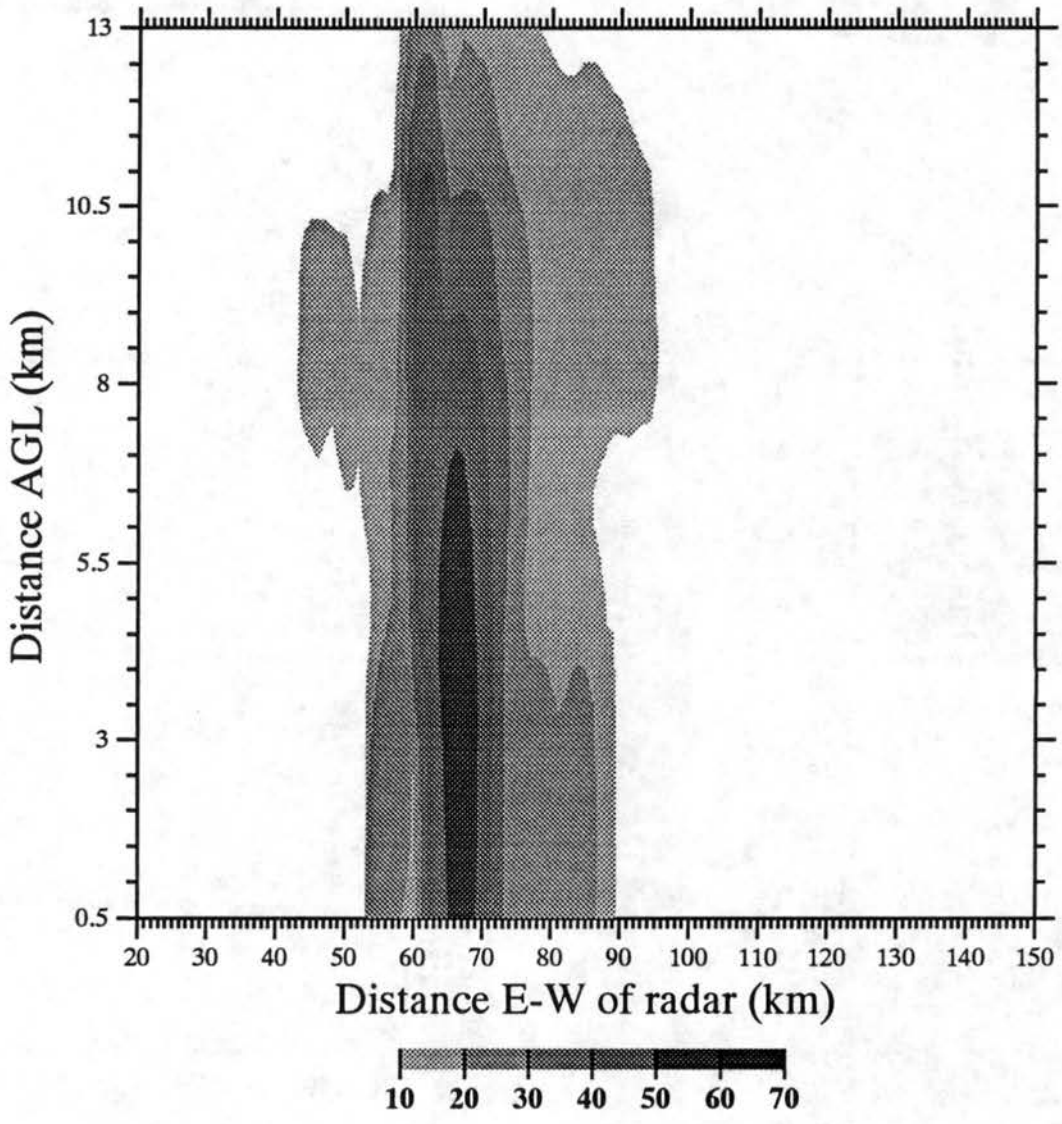

Figure 4.8c: Same as Figure 4.8b except at 67 km north of CHILL.

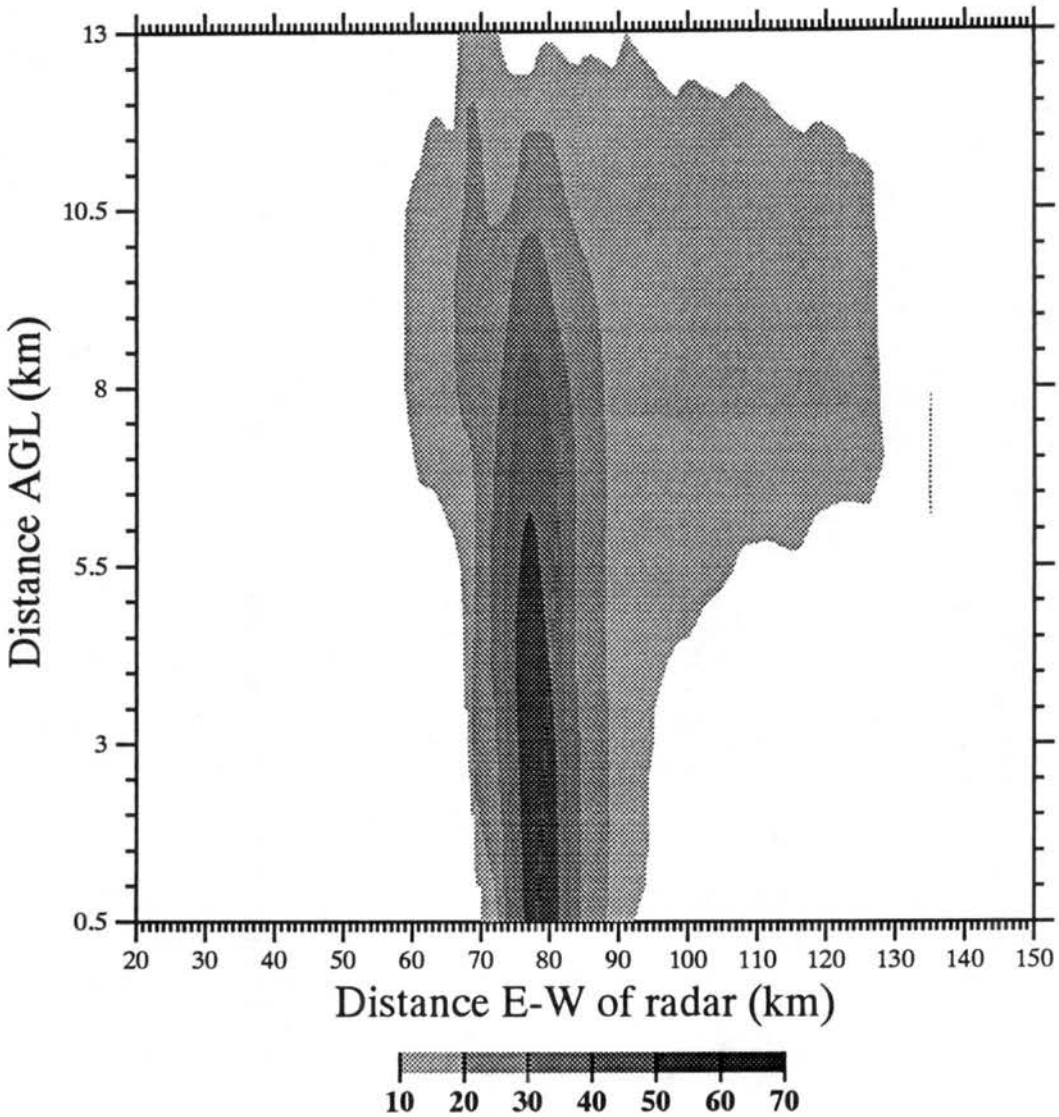

Figure 4.8d: Same as Figure 4.8c except at 55 km north of CHILL.

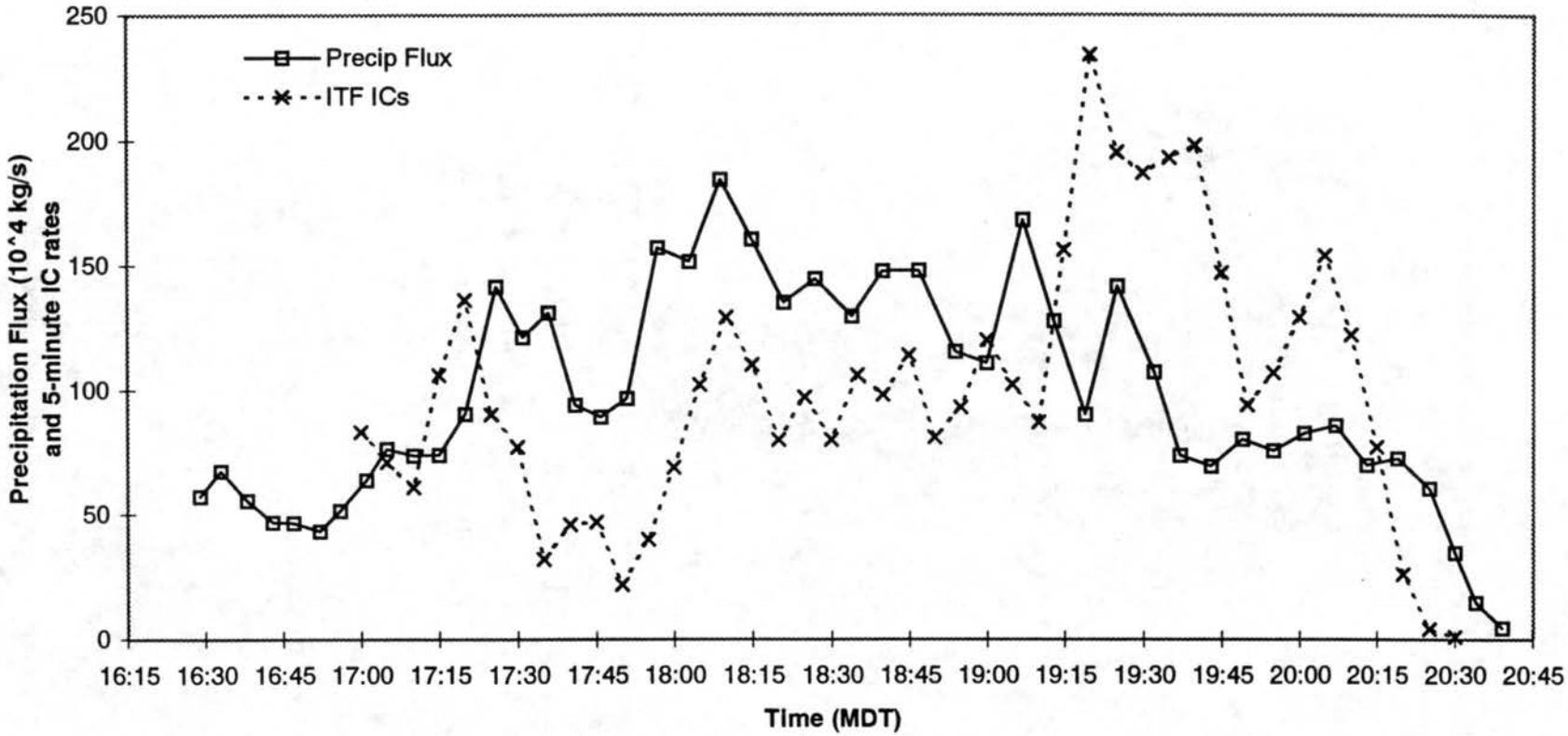

Figure 4.9: Time histories of radar-inferred storm complex total precipitation mass flux (rain + hail) at 0.5 km AGL and 5-minute IC flash rates. Fluxes are plotted at the start of each radar volume, and flash rates are plotted at the start of each 5-minute period.

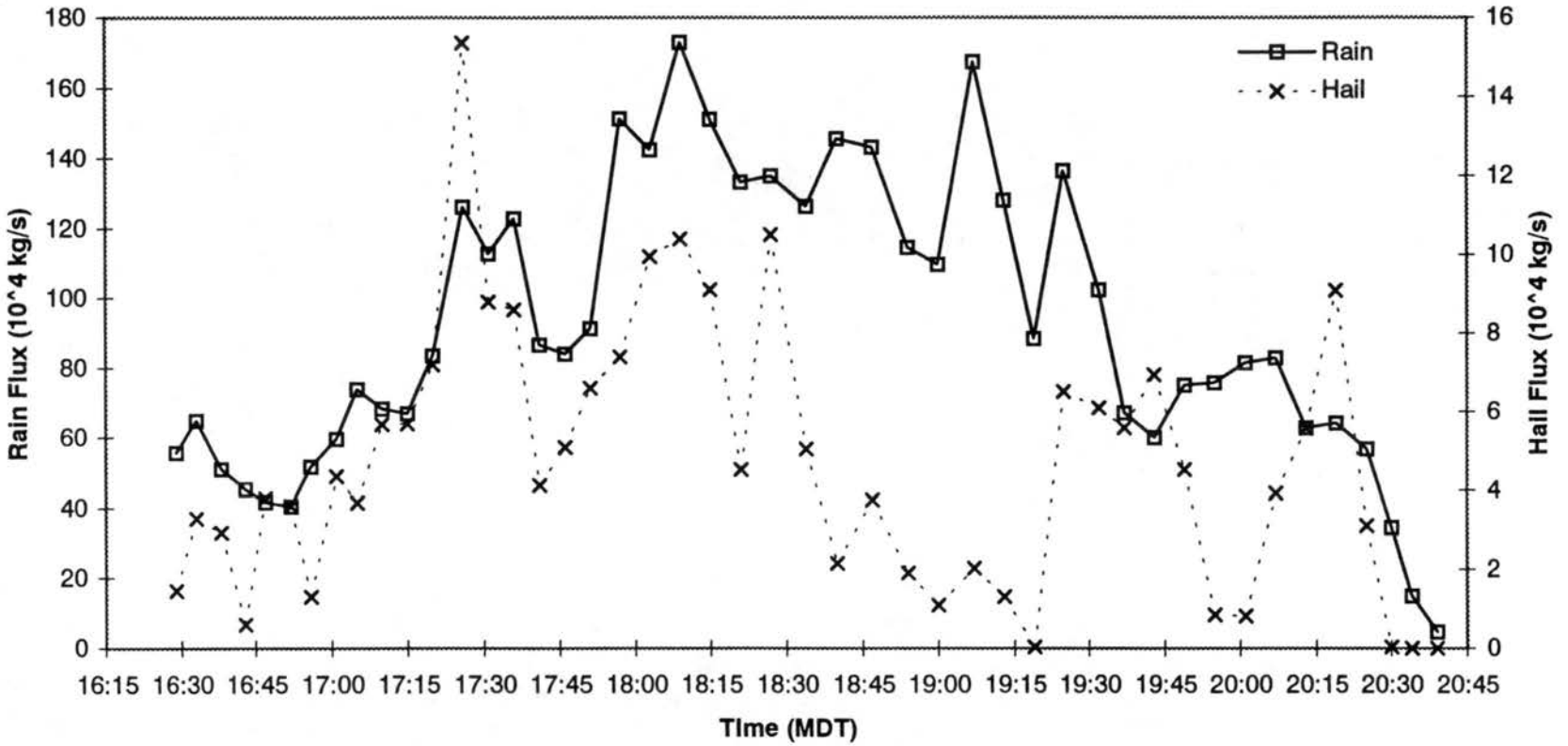

Figure 4.10: Time histories of radar-inferred storm complex total rain and hail mass fluxes at 0.5 km AGL. Fluxes are plotted at the start of each radar volume.

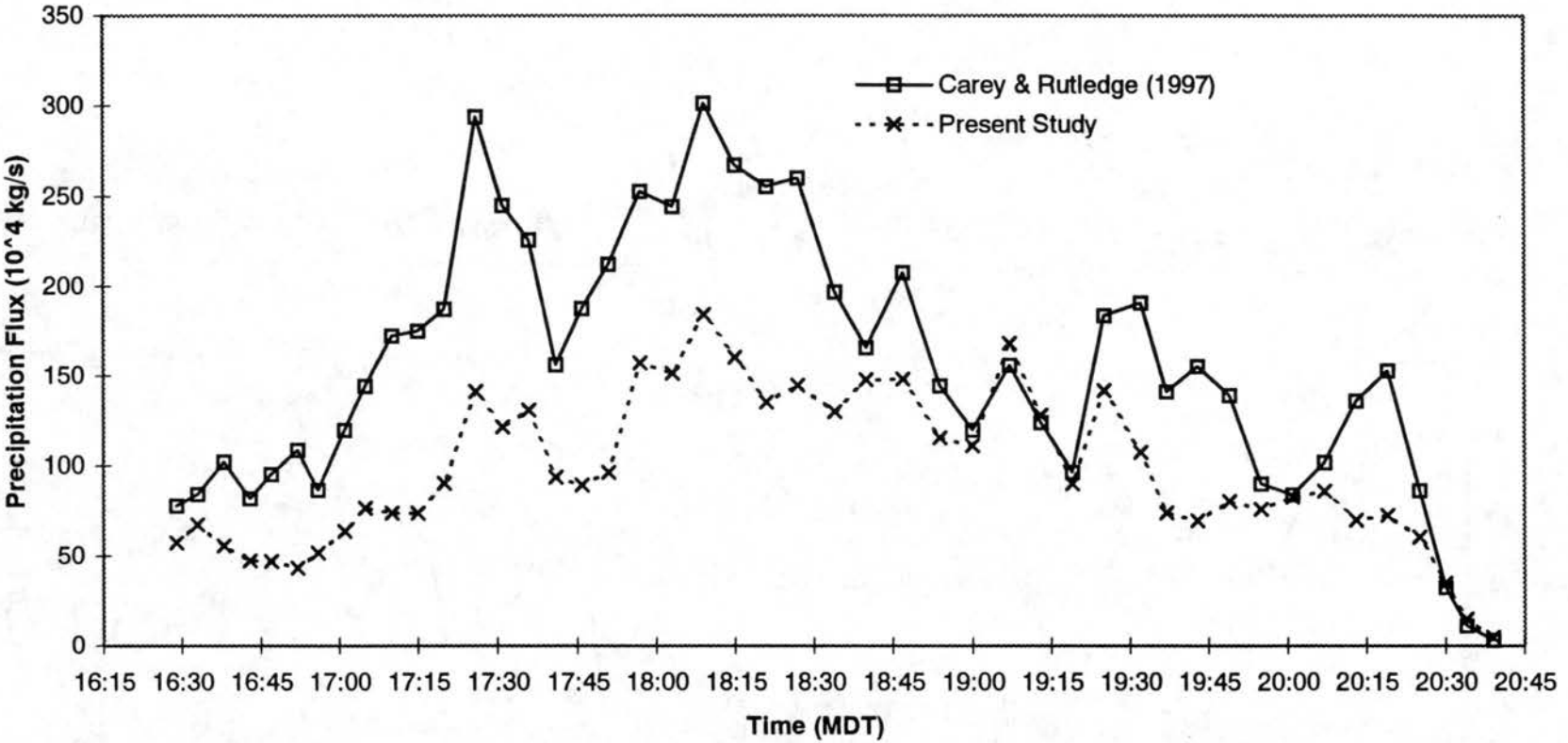

Figure 4.11: Comparison between radar-inferred storm complex total precipitation fluxes at 0.5 km AGL, calculated via the method of the present study and via the method of Carey and Rutledge (1997).

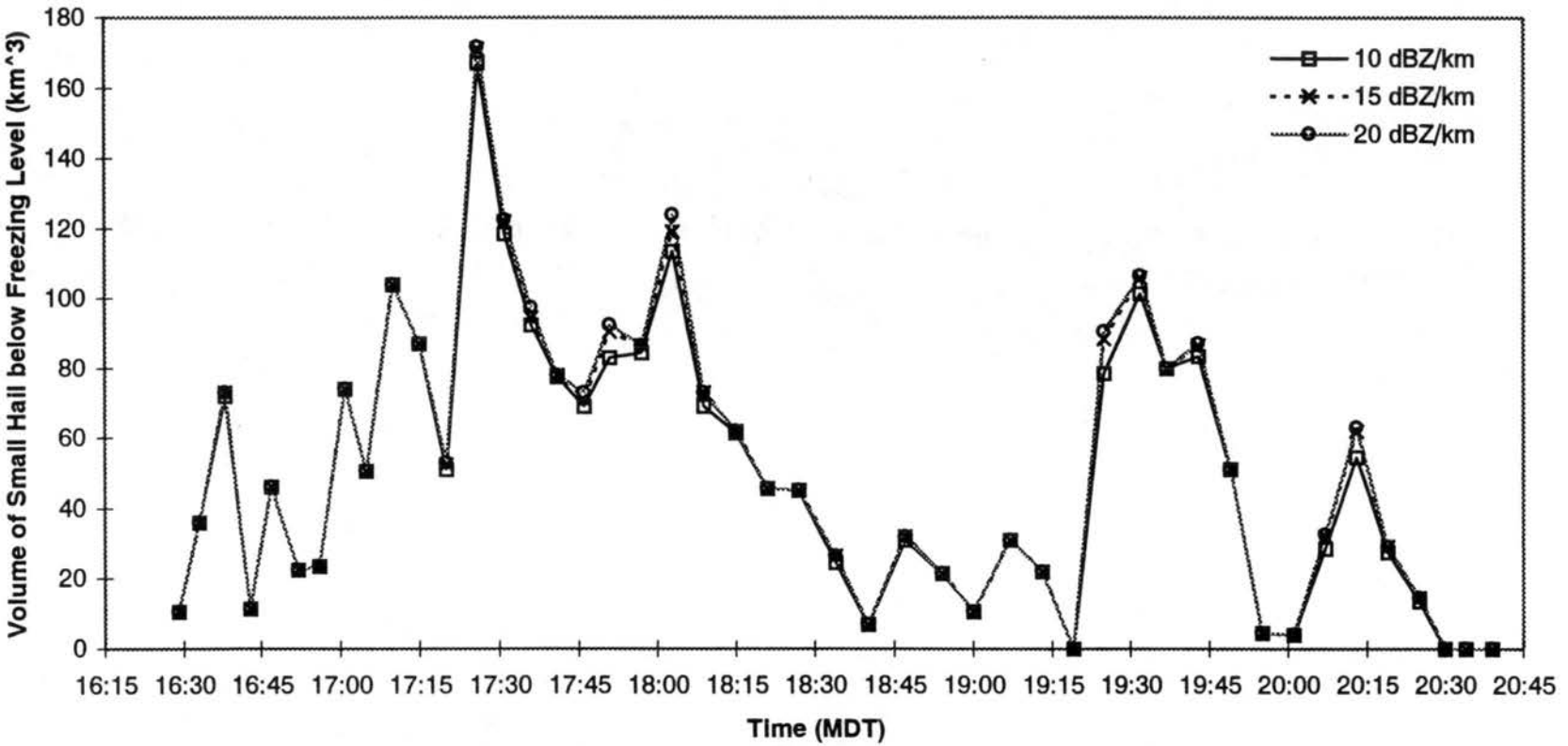

Figure 4.12: Comparison of radar-inferred volumes of small (< 2 cm) hail below the freezing level, for three different reflectivity gradient filtering thresholds.

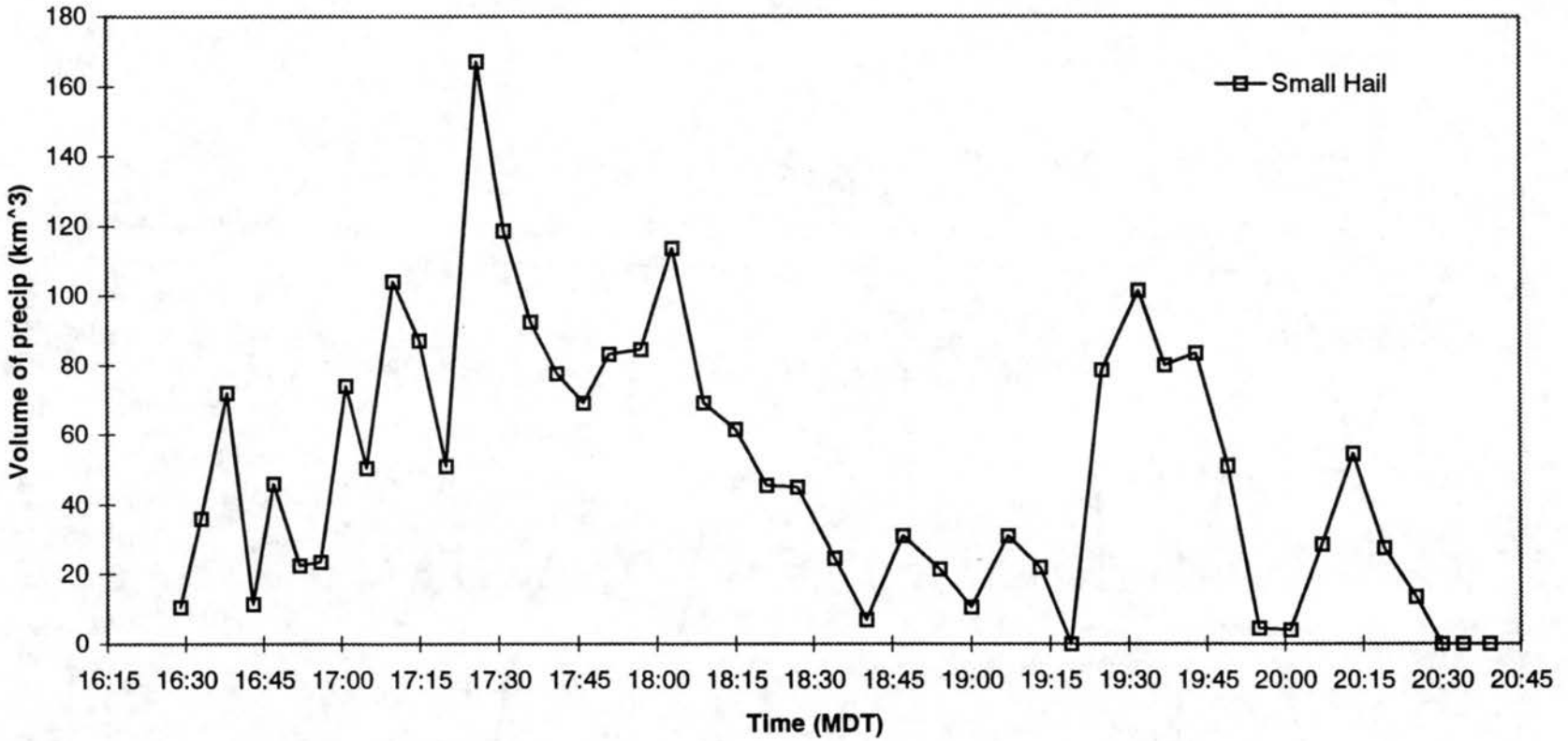

Figure 4.13: Time histories of radar-inferred volume of small, wet hail below the freezing level for the 10 July 1996 storm.

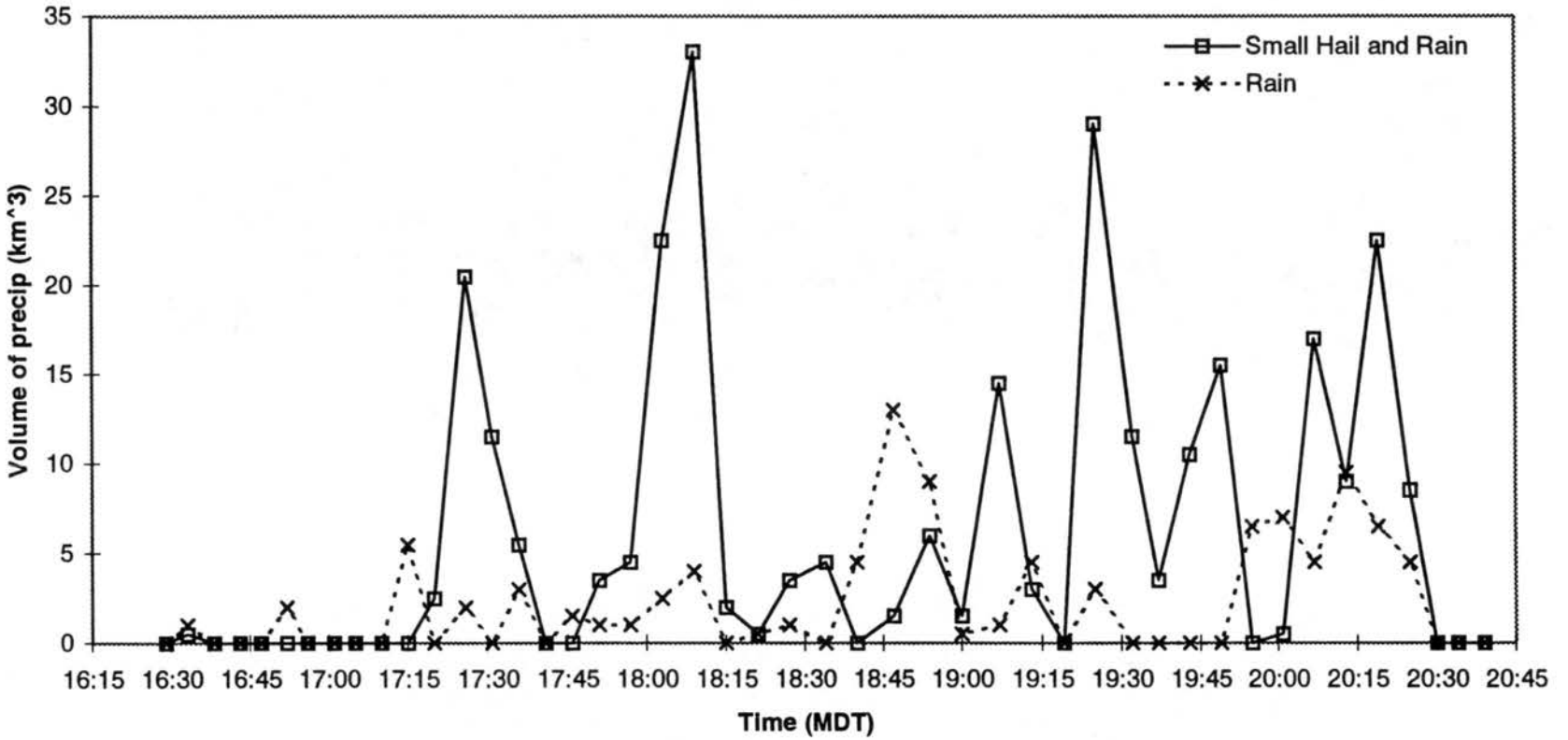

Figure 4.14: Time histories of radar-inferred volumes of small hail mixed with rain and rain only, below the freezing level.

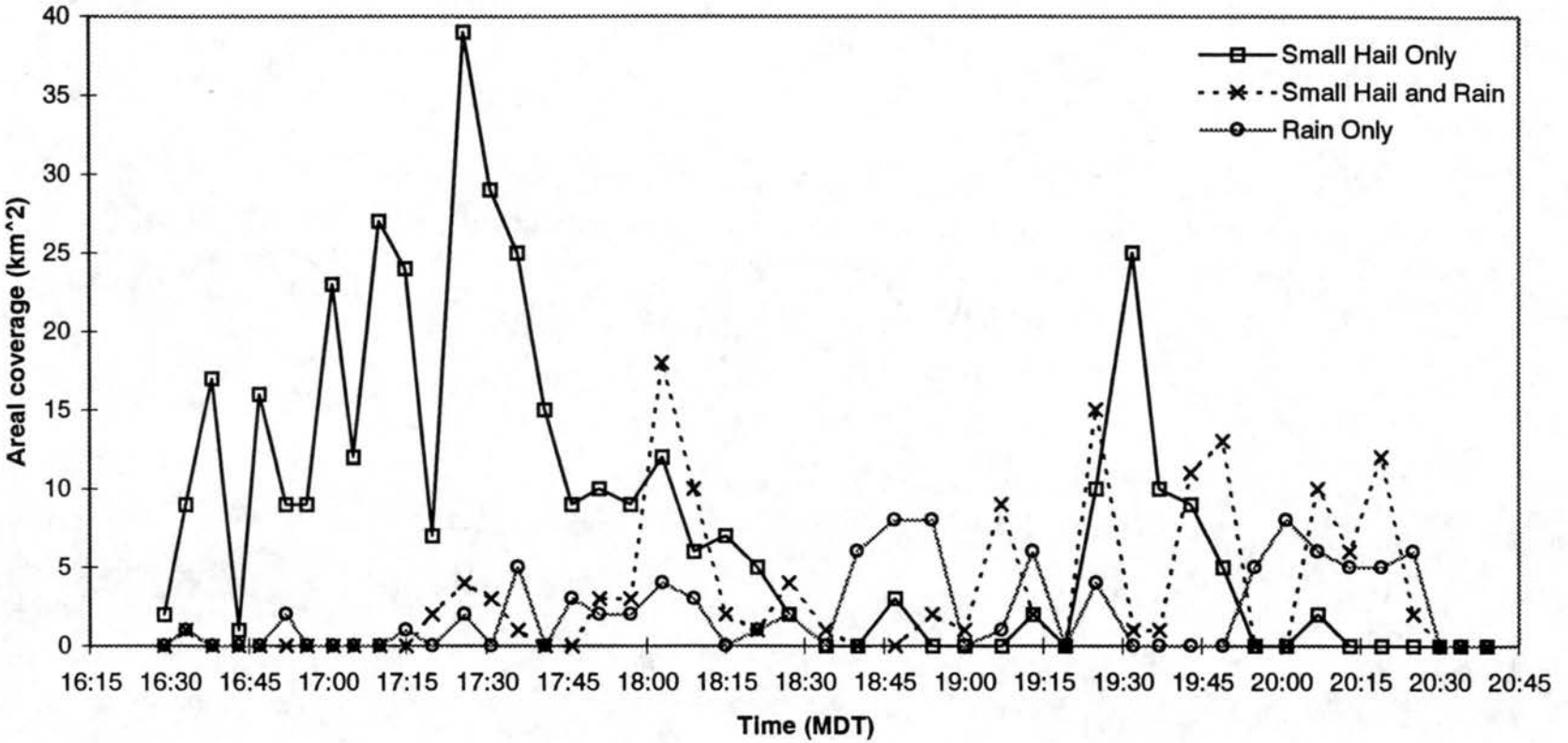

Figure 4.15: Time histories of the areal coverage at 0.5 km AGL of small hail only, small hail mixed with rain, and rain only.

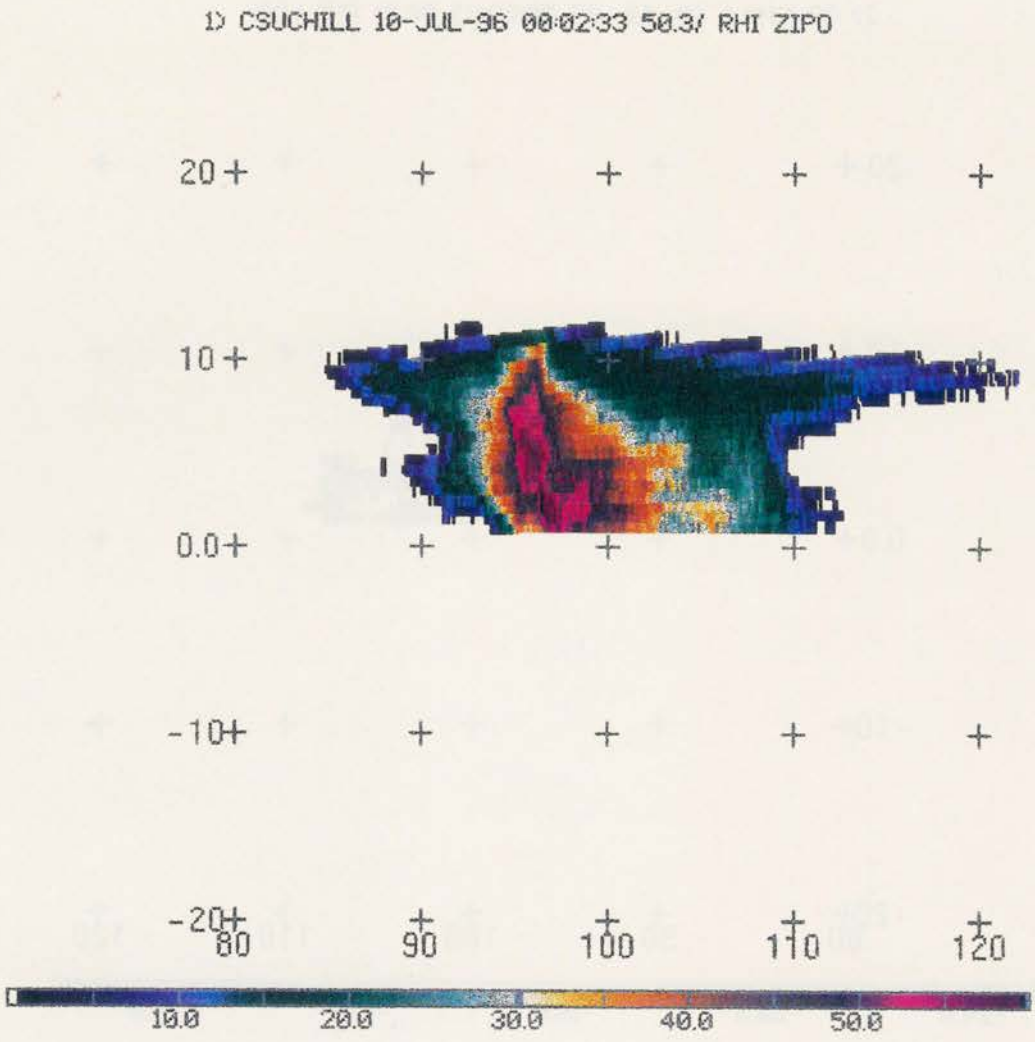

Figure 4.16a: Vertical cross-section of radar reflectivity (dBZ) along the 50° azimuth for the volume beginning at 2357 MDT. The horizontal scale (distance from the radar) is in km, and the vertical scale (distance AGL) is in km. The arrow denotes the region of probable wet growth.

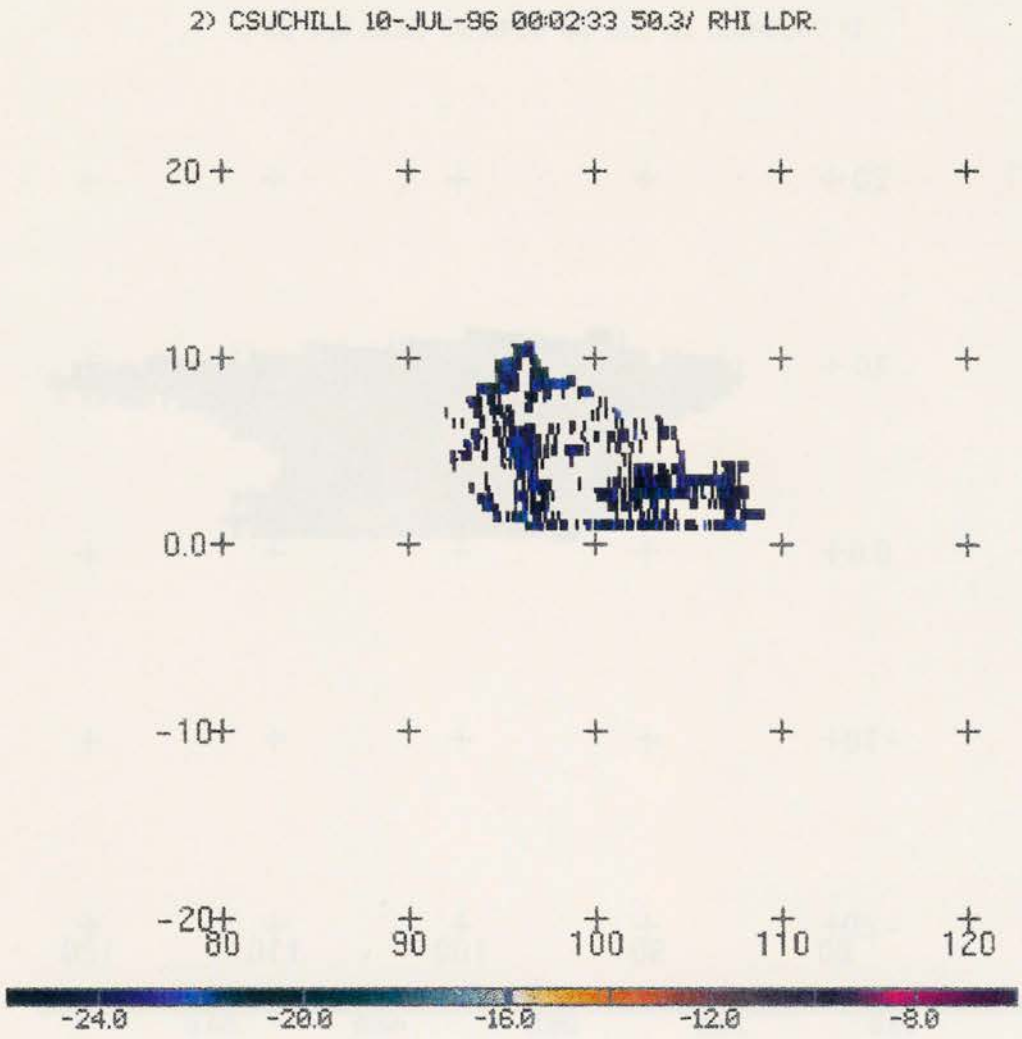

Figure 4.16b: Same as Figure 4.16a except for LDR (dB). Note that LDR values below -26 dB are not displayed.

CHAPTER 5

ANALYSIS OF THE 12 JULY 1996 STORM

The storm of 12 July 1996 provides another example of a major transition in storm structure, as the storm evolved from an intense, multicell, hail-producing storm to a weak rainstorm, and eventually to stratiform precipitation. This transition was also clearly distinguishable in the cloud-to-ground (CG) lightning data, with CG flash rates rising sharply after the storm transitioned to the less intense form. Before this, CG flash rates were low, and comparable to the 10 July 1996 storm.

5.1 Atmospheric conditions

Figure 5.1 shows data from a mobile CLASS sounding launched from the Fort Morgan Airport at 1356 MDT on 12 July 1996. Plotted on the Skew-T/Log-p diagram are vertical profiles of temperature, dewpoint, and winds. The sounding appears to be somewhat more moist than the 10 July 1996 sounding. The CAPE is only 441 J kg^{-1}, the shear over the lowest 6 km is 13.6 m s^{-1}, and the Bulk Richardson Number (BNR) is 4.7. The BNR is even lower than 10 July. It is suggestive of possible supercellular development (Weisman and Klemp, 1982), but again it is so low because the CAPE is also low. The ambient wind shear is weak as well. However, the Lifted Index is -3.45, which is greater than 10 July and implies that convection was at least possible. But overall, the atmospheric environment did not appear conducive to the development of intense

convection. However, this sounding may not have been entirely representative of the storm's environment, since it initially developed on the over 100 km northwest of the sounding launch location. Also, conditions could have changed between the time of the sounding and the time of storm development (e.g., a short wave may have propagated through the region after the sounding was taken). The steering winds appear to be mostly westerly, whereas the storm itself traveled to the southeast. This is perhaps further evidence that the sounding was not representative of the storm environment.

5.2 Overview of storm evolution and major transition

Figure 5.2 (a-h) shows horizontal cross-sections of radar reflectivity (dBZ) obtained from the CSU-CHILL radar at 0.5 km AGL for the 12 July 1996 storm. The cross-sections are approximately 30 minutes apart. Full radar volume coverage of the storm began at 1647 MDT. At this time the storm was over the Cheyenne Ridge in extreme southern Wyoming. It then moved to the southeast toward the CHILL radar, passing just east of the radar site, and continued moving to the southeast away from the radar. In its early stages it was relatively well-positioned in the western lobe of the interferometer (ITF). However, as it approached CHILL, its eastern extent crossed the baseline of the ITF into the eastern lobe, while the western half of the storm remained in the western lobe. After the storm passed CHILL it moved beyond the southern boundaries of either ITF lobe.

At 1658 MDT (Figure 5.2a), the storm mainly consisted of five distinct cells or groups of cells. (Cell groups will be referred to as "cells" for simplicity.) The southern central cell, Cell 1, was the most intense, in terms of the areal extent of its low-level reflectivity. The

cell immediately north of Cell 1, Cell 2, also was strong. The other cells in the storm complex - Cells 0, 3, and 4 - were much less intense.

By 1730 MDT (Figure 5.2b), Cell 4 had intensified, while Cells 1 and 2 had decreased in strength. The other cells from the 1658 MDT observation period had predominantly dissipated, or were not easily distinguishable within the large area of contiguous echo. Between this time and 1804 MDT (Figure 5.2c), Cell 4 continued to strengthen, and an additional cell, Cell 5, had developed on its forward flank (to the southeast) and began to merge with Cell 4. To the east of these cells a large contiguous echo region persisted, with maximum dimensions of approximately 40-50 km in either direction. Many weak cells continued to be embedded within this region of echo.

From this time until 1832 MDT (Figure 5.2d), Cell 5 completed its merger with Cell 4, and another cell, Cell 6, formed on the forward flank of the main cell. Within the large contiguous echo region, a weak cell - Cell 7 - began to form and dominate the area. At 1855 MDT (Figure 5.2e), the storm complex was divided into two main parts, the western and the eastern. The western region was comprised of Cells 4 and 6, which were undergoing a merger. These cells were quite intense, with extended areas of 60 dBZ and greater reflectivity at 0.5 km AGL. The eastern region was comprised mostly of stratiform echo with some embedded weak cells (Cell 7) which had not yet reached 50 dBZ in the low-level reflectivity.

By 1931 MDT (Figure 5.2f), Cells 4 and 6 had merged, and weakened. Cell complex 4, which comprised the western region of the storm, consisted of three distinct (> 50 dBZ) cores. The eastern region had continued to shrink in areal coverage, but Cell 7 had intensified and was now above 50 dBZ at 0.5 km AGL.

After this time, at 1959 MDT (Figure 5.2g) and 2031 MDT (Figure 5.2h), the storm complex (i.e., both Cells 4 and 7) weakened, though by 2031 Cell 4 had re-intensified to some degree on its western flank. The eastern region of the storm complex, the region once occupied by Cell 7, featured much weaker convection by 1959 and appeared to be comprised largely of stratiform echo with some very weak embedded convection (by 2031 MDT). After the volume scan starting at 2057 MDT radar coverage was terminated because peak low-level reflectivities were below 50 dBZ throughout the storm, and the storm was well south of the ITF lobes.

To summarize storm evolution, when full radar volume coverage was begun, the storm complex was very large and multicellular. Throughout its lifetime, the storm complex remained multicellular, usually with one cell dominating much of the reflectivity pattern, though there also were other intense cells at times. After 1900 MDT the storm complex continued to persist in some form for over 2 hours, even though it featured lower peak reflectivities, over a smaller area, than before this time. This transition in storm structure will be examined in greater detail in the next few sections.

5.3 Comparison of lightning and bulk precipitation rates

Figure 5.3 shows 5-minute CG lightning rates as functions of time for the entire storm complex, separated into positive and negative CG components. The lifetime of this storm can be separated into two relatively distinct phases of CG lightning. In the first phase, CG flash rates for either polarity were quite low, typically less than 5 per 5-minute period. During this phase a large percentage of the CGs were of positive polarity, on the order of 50% (although total CG flash rates were low). However, after 1900 MDT, positive CG

rates remained similar for less than an hour and then declined to 0 until near the end of radar coverage. Negative CG flash rates rose sharply, peaking at 25 per 5-minute period at 1935 MDT, then declined to more modest values late in the storm complex's lifetime.

Following the method of Chapter 2, hail and rain mass fluxes were calculated at 0.5 km AGL for all radar volume scans of the storm complex. However, because this storm came so close to the radar, the azimuthal boundaries of the radar volumes had to be limited, especially during 1830-1930 MDT. Thus, the entire storm was not always included in these volumes, even at low levels, so precipitation fluxes will be underestimates during this time period. However, because effort was made to include as much significant (i.e., > 30 dBZ) echo as possible, the flux trends should not be adversely affected.

In addition, following the method of Chapter 3, intra-cloud (IC) flash rates were extracted from the interferometer (ITF) data. However, this storm was not well-placed in relation to the ITF lobes. After 1800 MDT, the eastern extent crossed from the western lobe into the eastern lobe. However, until 1920 MDT, the main cell cores were well-placed in either ITF lobe, with the main western cores within the western lobe and the main eastern cores in the eastern lobe, with only weak echo actually in the vicinity of the baseline. As will be shown later, IC lightning was well-correlated in position with high reflectivity cores, so flash rates should not be affected significantly. However, the IC rates that were calculated are likely to be underestimates after 1800 MDT, though trends should not be affected appreciably because the high reflectivity cores - that is, the cores that were most likely to produce IC lightning - were still well-positioned. After 1920 MDT, the storm began moving out of the southern boundaries of both lobes, so flash rate calculations were not done for later times, nor were they computed for times prior to 1700

at which time the northern part of the storm complex extended beyond the northern ITF boundary.

Figure 5.4 shows precipitation fluxes and 5-minute IC flash rates as functions of time for the entire storm complex. Note the significant change in hail fluxes around 1900 MDT. Before this, hail fluxes were significant, though of a pulsing nature related to individual cell growth and decay. After this time, however, hail fluxes were largely insignificant. This change in storm complex hail fluxes is well-correlated with the change in storm complex negative CG rates. The drop-off in hail fluxes after 1900 MDT also seems correlated with a similar, yet not as severe, reduction in rain fluxes from a peak just before 1900.

When full radar coverage began at 1647 MDT, the low-level precipitation fluxes appeared to be declining rapidly from an earlier peak. Both the rain and hail flux trends seem in phase at first, but the rain flux recovers from its reduction earlier than the hail flux. By 1720 MDT, though, both fluxes have recovered and peaked again, albeit at much smaller values than before. ITF IC flash rates seem to peak earlier than either of the precipitation fluxes, at 1705, and actually achieved a minimum by 1720. After 1720 MDT, IC flash rates began a sharp rise, but the low-level rain and hail fluxes declined to minima at 1730 MDT. They recovered after this time, and then an interesting series of events occurred, with IC flash rate peaking at 1740 MDT, hail flux peaking after this at 1759, and then the rain flux reaching a maximum at 1812. This implies, in a total storm complex sense, that the IC rate peaks before the fallout of significant hail, which itself precedes the fallout of significant rain. The tendency for IC lightning to lead the low-level

hail fluxes is consistent with what was seen in the 10 July storm, though the lag between the hail and rain fluxes was not observed in that storm as it is in the present case.

After this time, all three variables began another decline and subsequent recovery. Once again, hail flux led the rain flux, but the IC flash rate took a much longer time to reach its next peak at 1905 MDT, which occurred after the hail peak at 1849 and the rain peak at 1855. Thus, whereas before IC flash rate led the precipitation fluxes, it now lagged both. The decline in IC rates after 1905 again continued lagging the precipitation flux reductions, though IC rate calculations were terminated after 1920 MDT. After 1900 MDT, hail fluxes remained largely negligible, while rain fluxes were lower than their peak at 1855, but continued to be fairly significant. The rain flux made a small recovery at 1918, and remained very steady until 1937 when it underwent a sharp decline. After reaching a minimum around 2000 MDT, the rain flux recovered to one final peak, around 2020. This last rain flux peak was roughly coincident with a slight increase in hail flux, though the hail flux was still very low compared to earlier times. After this time, the fluxes again declined. Radar coverage was terminated after 2057 MDT.

Note, in general, that the fluxes and IC rates are much higher than the storm of 10 July 1996. This is likely due to two causes. One is that the 12 July storm complex itself was larger, both in volume and areal extent. The second is that it appearedmore intense, based on the gridded reflectivity data seen in Figure 5.2, with higher peak reflectivities and larger areal extent of high reflectivity regions.

There are two main questions to be posed regarding Figures 5.3 and 5.4. The first is: Why do the negative CG rates and the storm complex hail fluxes seem so anti-correlated, in a bulk sense? The second is: Why did the IC flash rate lead the low-level precipitation

fluxes early in the storm's lifetime, yet lag them later? These questions will be examined in order in the following discussion.

From Figures 5.3 and 5.4, it can be seen that around 1804 MDT, CG flash rates were quite low, and storm complex hail and rain fluxes were near their maxima. Figure 5.5 shows a vertical cross-section of reflectivity at 11 km west of CHILL at this time. Referring to Figure 5.2c, this cross-section cuts through the center of Cell 4. Based on this cross-section, the cell appears intense, with the 30 dBZ contour extending to 11 km AGL, and the 50 dBZ contour extending to 7.5 km AGL. Figure 5.6 shows a horizontal cross-section of reflectivity at 0.5 km AGL for the radar volume starting at 1937 MDT. Also shown are the ground-strike positions and polarities of NLDN-detected CG lightning that occurred during this volume (approximately 6 minutes in duration). At this time the negative CG rates were at their peak, and the storm was divided into two main regions, Cell 4 and Cell 7. (Refer to the discussion of Figure 5.2.) Likewise, CG lightning around this time was divided nearly equally between the two major cell complexes. Figures 5.7a and 5.7b show vertical cross-sections of reflectivity at this time at 24 km east of CHILL and 56 km east of CHILL, respectively. These two cross-sections cut through the approximate centers of the major cells. Contrasting these vertical cross-sections with Figure 5.5, it is apparent that cell structure is radically different between the two times. The 30 dBZ contours at 1937 MDT extend to only 9.5 km AGL for either cell complex. The 50 dBZ contours extend to 4 km AGL or less. There is no region of 60 dBZ and greater reflectivity like there was at 1804 MDT, when the 60 dBZ contour extended to 4 km AGL. Overall, the storm complex at 1937 MDT appears much less intense, based on both horizontal and vertical structure, compared to the storm at 1804. Thus, marked

differences in storm intensity between the two times correspond well to the marked differences in CG rates. This is further confirmation of what was seen in the hail flux data, where significant hail fluxes - even though they underwent major fluctuations - corresponded to low CG production, but very low hail fluxes corresponded to significant production of negative CGs. It appears that, for this storm at least, storm intensity - as determined by the existence of hail and the maximum heights of the 30 and 50 dBZ reflectivity contours - is inversely correlated with negative CG lightning, at least in a bulk sense. This will be discussed further in Section 5.5.

The second question deals with why IC lightning led low-level precipitation fluxes at first, but lagged them later. The answer to this question relates to the multicellular nature of the storm complex. Figure 5.8 (a-b) shows horizontal cross-sections of reflectivity at 0.5 km AGL at 1741 and 1855 MDT, respectively. The mean horizontal positions of IC flashes occurring during each radar volume (approximately 6 minutes in duration) are overlaid on these plots of reflectivity. At both times IC lightning rates were near their maximum values, and it appears that the western half of the storm was producing the most ICs. Note, however, that especially at 1855, the storm complex is straddling the ITF baseline. However, the two main cell regions were still well-positioned in the ITF lobes. At 1741 MDT, there was mainly one cell producing IC lightning. The same was basically true at 1855 MDT, but note the large area of 50 dBZ and greater echo north of the main IC lightning centroid. This was an older cell, which due to its areal coverage and intensity likely was contributing significantly to the low-level precipitation fluxes, even though it was producing little IC lightning. At 1741 MDT there was no other major cell to contribute to the low-level precipitation fluxes. Thus at this time IC rates and

precipitation fluxes were largely dominated by one cell, but at 1855 MDT the IC lightning was still dominated by one cell, but the fluxes had an additional major cell contributing to their total values.

Thus, the apparent change in the IC flash rate trend relative to the low-level precipitation flux trend (Refer to Figure 5.4.) probably is due to the multicellular nature of the storm. The precipitation fluxes and IC rates are for the entire storm complex. Near both major IC flash rate peaks, only one cell was contributing significantly to the IC flash rate. But during the second peak, two major cells were contributing to the low-level precipitation fluxes, whereas during the earlier peak there was only one major cell. The superposition of the flux contributions from these two cells around the time of the second IC peak are probably what caused the apparent phase change between the fluxes and IC lightning. This superposition of cells also probably was causing the slow increase in IC rate toward its final peak. On an individual cell basis, based on the available data, IC lightning preceded the development of significant precipitation. This is seen with the first major IC peak, when only one major cell was in existence. The same pattern likely repeated itself in subsequent cells, but because of the superposition of two major cells this pattern is not evident.

5.4 Identification of bulk precipitation types

Following the method of Chapter 2, bulk hydrometeor identification was performed on the radar volumes from this storm. Unfortunately, unlike the storm of 10 July, this storm came extremely close to the radar. Due to its proximity to the radar for much of its lifetime, the storm was not "topped" and medium- to high-altitude data were not obtained

for the entire storm complex. Thus, trends in bulk precipitation volumes below the freezing level will not be examined in detail, as such trends will be corrupted by the lack of data from a significant percentage of the radar volumes. Instead, areal coverage of bulk precipitation types at 0.5 km AGL will be examined, as such trends will not be affected by the loss of higher altitude data.

The freezing level based on the afternoon (1356 MDT) CLASS sounding launched from the Fort Morgan airport was determined to be 3.42 km AGL, CHILL relative. The reflectivity gradient thresholds again were set to the values of 10, 15, and 20 dBZ km^{-1}. Sensitivity tests were performed to better estimate the proper threshold setting. For this storm complex, most low-level (0.5 km AGL) grid points were split between rain only and small (< 2 cm) hail mixed with rain. Small hail only, and any form of large (≥ 2 cm) hail, were not diagnosed to be present at the lowest grid level except perhaps once or twice, and at those times their areal coverage was quite small (1-2 km^2 at the most). When higher altitude small hail calculations were available, typically small hail mixed with rain was most predominant closer to the surface, and small hail only was predominant closer to the freezing level. This suggests that significant melting of hail occurred as it passed below the freezing level and approached the surface. Figure 5.9 shows the time history of the low-level areal coverage of small hail mixed with rain for all three reflectivity gradient thresholds. The general pattern is quite similar to the hail flux time history in Figure 5.4, and is independent of the reflectivity gradient criteria. In both plots, there are indications of a few major pulses of hail before 1900 MDT, and afterward there was little to no hail.

Figure 5.10 is the same as Figure 5.9, except for the low-level areal coverage of rain only. Note that for rain, all three reflectivity gradient thresholds produced the same

values. The general trends are similar to the rain flux trends in Figure 5.3 - the relative maxima around 1815, 1900, 1930, and 2020 MDT match up between the plots, though relative magnitudes do not necessarily match. Note that before 1800 MDT the areal coverage of rain at 0.5 km AGL was small, especially when its relative magnitude is compared to the relative magnitude of the rain flux at this time. However, recall that Figure 5.9 shows small hail and rain mixed together. These areas also will contribute to the rain flux to some extent.

Based on this limited precipitation identification analysis, it appears that the storm - when it produced hail - produced mostly small hail, and also had few hail-only or hail-dominated precipitation shafts. However, at 1749 MDT and again at 1759 MDT, the National Weather Service reported the occurrence of hail with a diameter of 1.75 inches (4.5 cm) near the town of Carr, Colorado, 50 km NNW of the CHILL radar. This suggests that even though the bulk of the frozen precipitation was in the form of small (< 2 cm) hail (according to the radar) this does not mean that larger hailstones did not develop and reach the surface. Based on the precipitation flux data as well as the areal coverage data, it appears that the storm produced vast quantities of rain. After 1900 MDT, nearly all the precipitation was in the form of rain.

Following the method of Chapter 4, searches for regions of probable wet growth of hail and graupel were done for the volumes preceding the major hail flux peaks at 1759 and 1832 MDT. Indications of small regions of enhanced LDR above the freezing level were found in the radar volumes starting at 1741 and 1753 MDT (which preceded the first peak), as well as 1818 MDT (which preceded the second peak). However, these regions (not shown here) were small compared to the one plotted in Figure 4.16. So, while wet

growth seems to have occurred in this storm, it probably did not occur to any significant extent.

5.5 Discussion and summary

Based on the available data, some general observations can be made about this case. The time of 1900 MDT serves as a turning point in the storm's evolution. Before this time, hail fluxes and areal coverage were significant, high-reflectivity (50 dBZ and greater) regions extended to high altitudes, and CG production (especially that of negative CGs) was at a minimum. After this time, hail was nearly non-existent, high-reflectivity regions extended to lower altitudes, and negative CG production was at a maximum.

Unfortunately, IC flash data do not extend far into this high CG production phase, but the available data show that high IC flash rates occurred during the most intense portions of the storm's lifetime, when significant precipitation was developing aloft. Following the typical pattern, the first time the IC flash rate peaked it did so before the fallout of significant precipitation. This is consistent with the observations of other researchers (Williams et al., 1989a,b; Changnon, 1992; Carey and Rutledge, 1996). Note also that, during this first major pulse, the peak in the fallout of significant hail preceded the peak in the fallout of significant rain. This is reasonable since the hail will have a larger terminal fall speed, so the hail should reach the ground in bulk before the rain. The second major IC peak occurred after the fallout of significant precipitation. However, this second pulse involves the superposition of the outputs of two distinct and strong cells, so this second peak is not necessarily inconsistent with the typical pattern. However, even though there

was a superposition of two major cells, the fallout of significant hail still led the fallout of significant rain, as was observed for the previous storm pulse.

After 1900 MDT, the storm evidently lost its ability to produce significant hail. It also featured a weaker vertical structure, in terms of radar reflectivity. This implies that, at least in an average sense, the cell updrafts after 1900 MDT were weaker than they were before this time. Thus, the increase in negative CG production after this time appears to be consistent with the elevated dipole hypothesis of MacGorman and Nielsen (1991). Because IC data only extend to 1920 MDT, corroborative evidence cannot be found in them. However, before 1920, IC flash rates - though still high - are decreasing. Thus, there is rough consistency, based on the elevated dipole hypothesis, between the decreasing IC flash rates with the rising CG flash rates after 1900 MDT - keeping in mind that these are all storm complex, and not individual cell, quantities. However, whether this is truly the collapse of the postulated elevated dipole cannot be verified.

Like the storm of 10 July, the high IC flash rate of this storm may explain why CG flash rates do not change appreciably after the first IC flash rate peak. The large number of ICs may have helped to neutralize the charged core before it began descending after this time. However, it appears that comparable flash rates did not cause a similar reduction in CGs after 1900 MDT. After this time, though, the available evidence implies that the average updraft strength in the storm complex had decreased. Perhaps this decrease in updraft strength allowed the negatively charged core to descend before it was largely neutralized by IC flashes.

Wet growth of hail and graupel probably did occur during this storm, though the available LDR data seems to indicate that, not unlike 10 July, wet growth was

overshadowed by dry growth, and thus may not have played a significant role in this thunderstorm's charge distribution.

Rain fluxes were high for this storm, especially compared to 10 July. In addition, peak rain rates were high. Peak rates in the gridded data typically exceeded 150 mm hr^{-1} from 1730 to 1930 MDT. Before and after this period, peak rates generally varied between 60 and 90 mm hr^{-1}. These averaged rates imply that instantaneous rates could have been significantly higher. High precipitation rates conceivably could allow the precipitation current to substitute for the CG lightning current, provided the rain was negatively charged. However, it does not necessarily explain why there is a dearth of CGs before 1730 and a relatively large number of CGs after 1930, even though peak rain rates and fluxes were comparable during the two different time periods.

Alternatively, the anti-correlation between the hail fluxes and the negative CG rates could imply that - if the hail were charged negatively - it may have been able to substitute for the CG lightning current. This hail current hypothesis seems to explain the CG lightning pattern better than the rain current hypothesis. Non-inductive charging theory (e.g., Takahashi, 1978) predicts that, for conditions near storm mid-levels, net negative charge is transferred to large ice particles like graupel and possibly small hail, while net positive charge is transferred to small ice crystals (if there is no charge-reversal process active). However, as the large ice (i.e., graupel and hail) falls to the ground, it should begin to melt and form rain, which would still carry net negative charge. Thus, based on non-inductive theory, both hail and rain should be carrying net negative charge. Thus, this apparent inability of the rain current hypothesis to explain the observed CG pattern seems to detract from the likelihood of the precipitation current hypothesis to be true.

Because precipitation currents were not measured during STERAO-A, the precipitation current hypothesis and the charge reversal hypothesis cannot be dismissed completely. However, the elevated dipole mechanism, acting in concert with the high IC flash rates, is an explanation most consistent with the available data.

The implications of these results and inferences will be examined in light of the results of Chapter 4 (the case study of the 10 July storm), and explored further in Chapter 6.

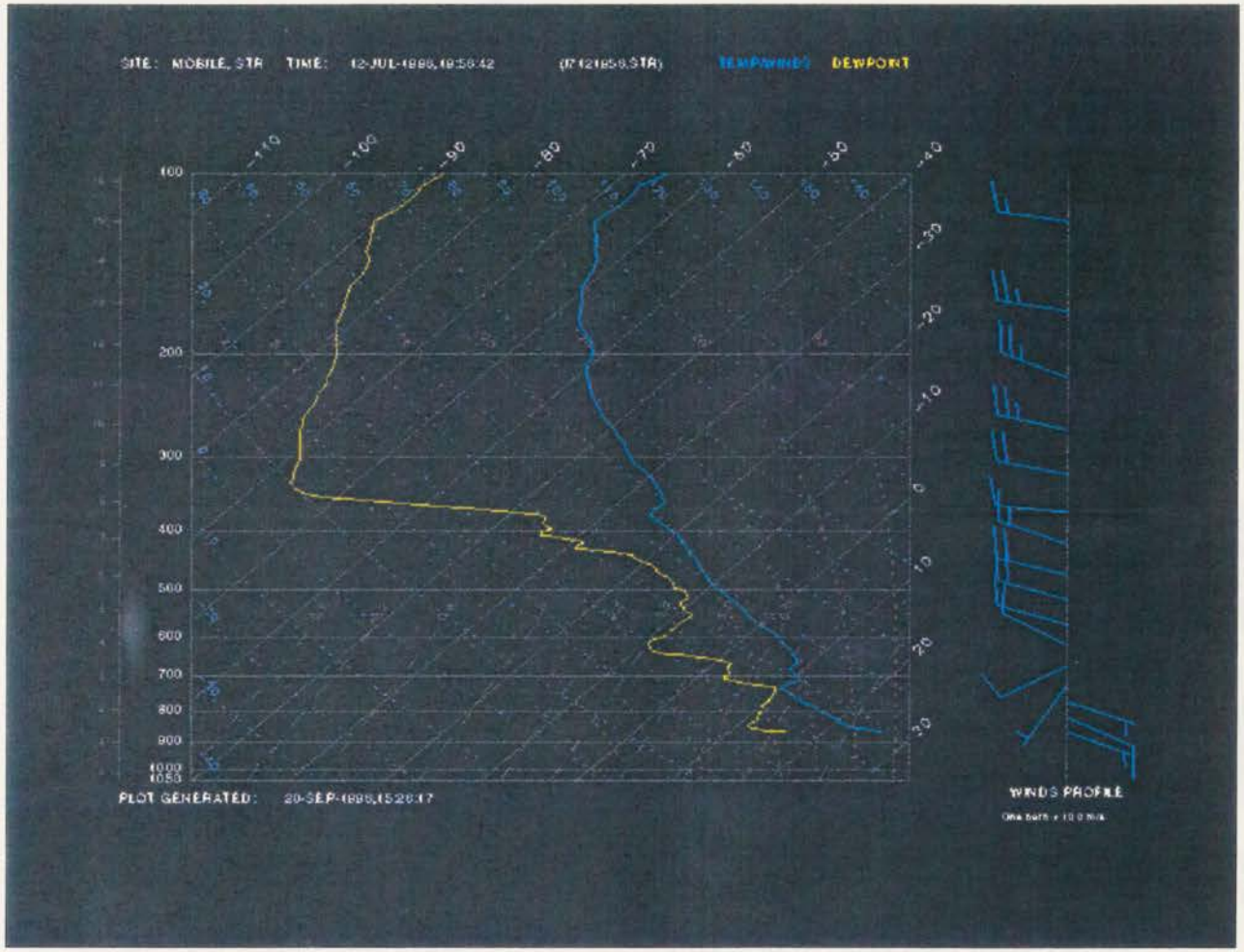

Figure 5.1: Data from the mobile CLASS sounding launched from the Fort Morgan, CO, Airport at 1356 MDT on 12 July 1996. Plotted in skew-T/Log-p format are vertical profiles of temperature, dewpoint, and winds.

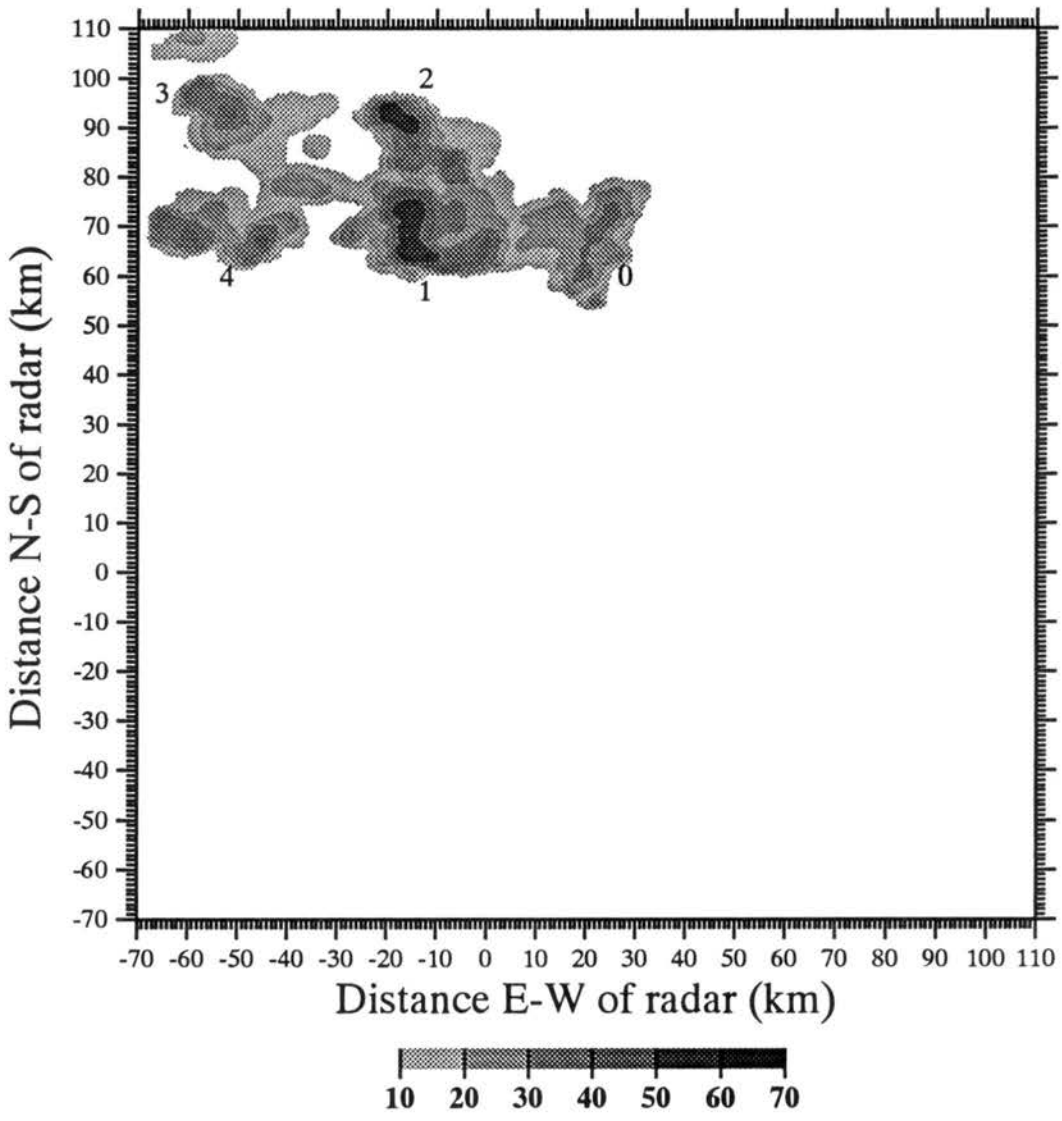

Figure 5.2a: Horizontal cross-section of radar reflectivity (dBZ) at 0.5 km AGL, for 1658 MDT on 12 July 1996.

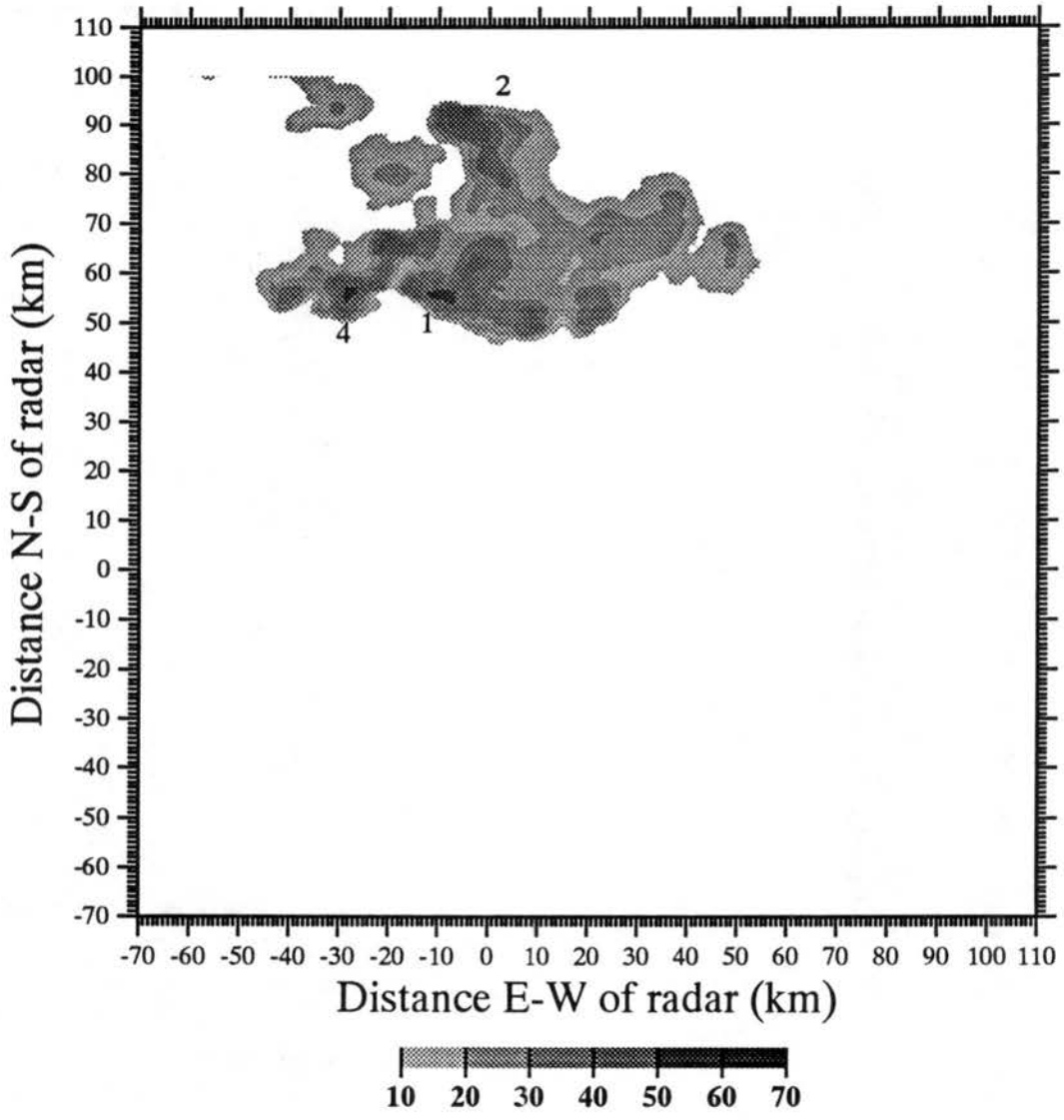

Figure 5.2b: Same as Figure 5.2a except for 1730 MDT.

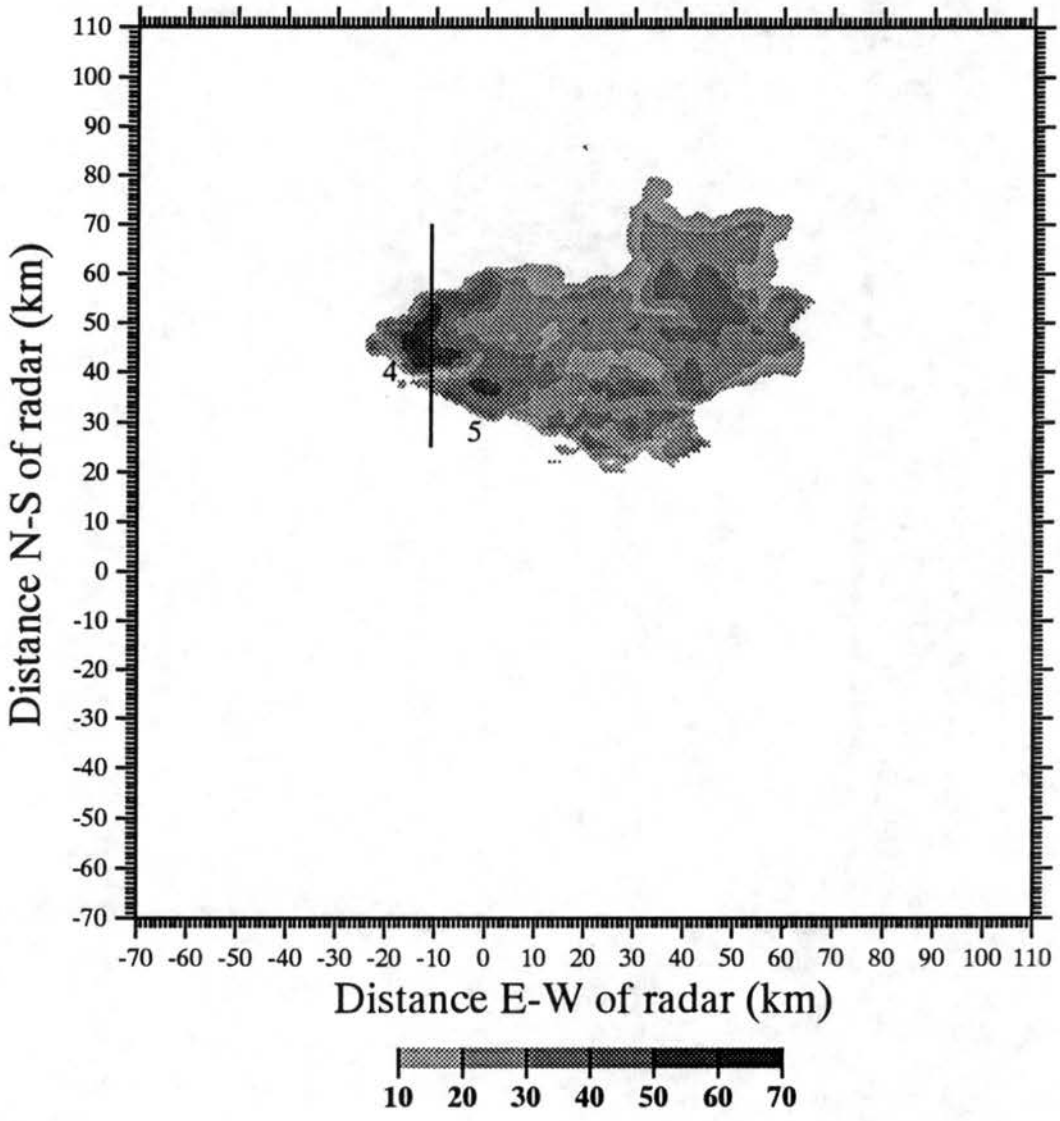

Figure 5.2c: Same as Figure 5.2b except for 1804 MDT. The line denotes the position along which the vertical cross-section in Figure 5.5 is taken.

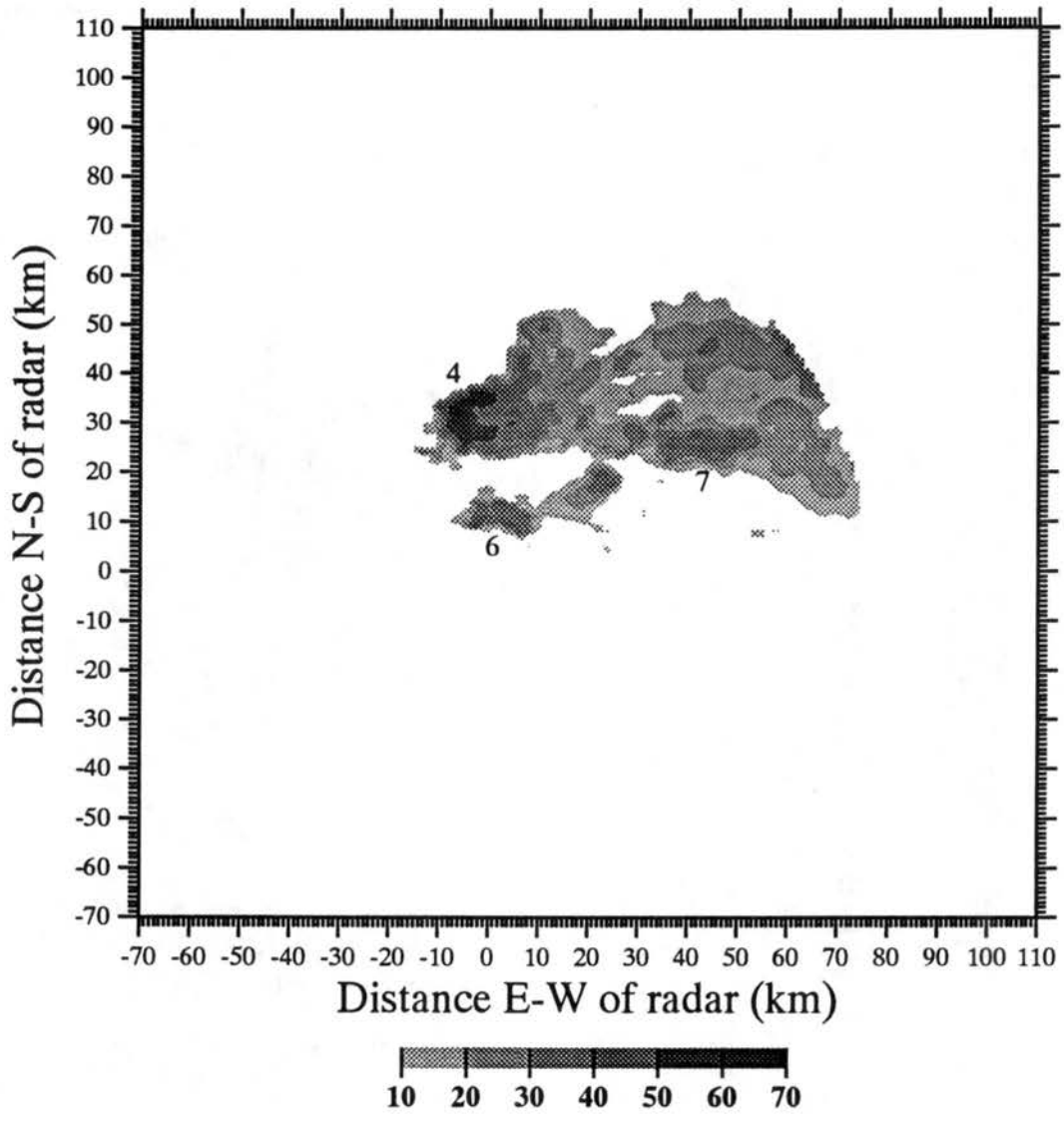

Figure 5.2d: Same as Figure 5.2c except for 1832 MDT.

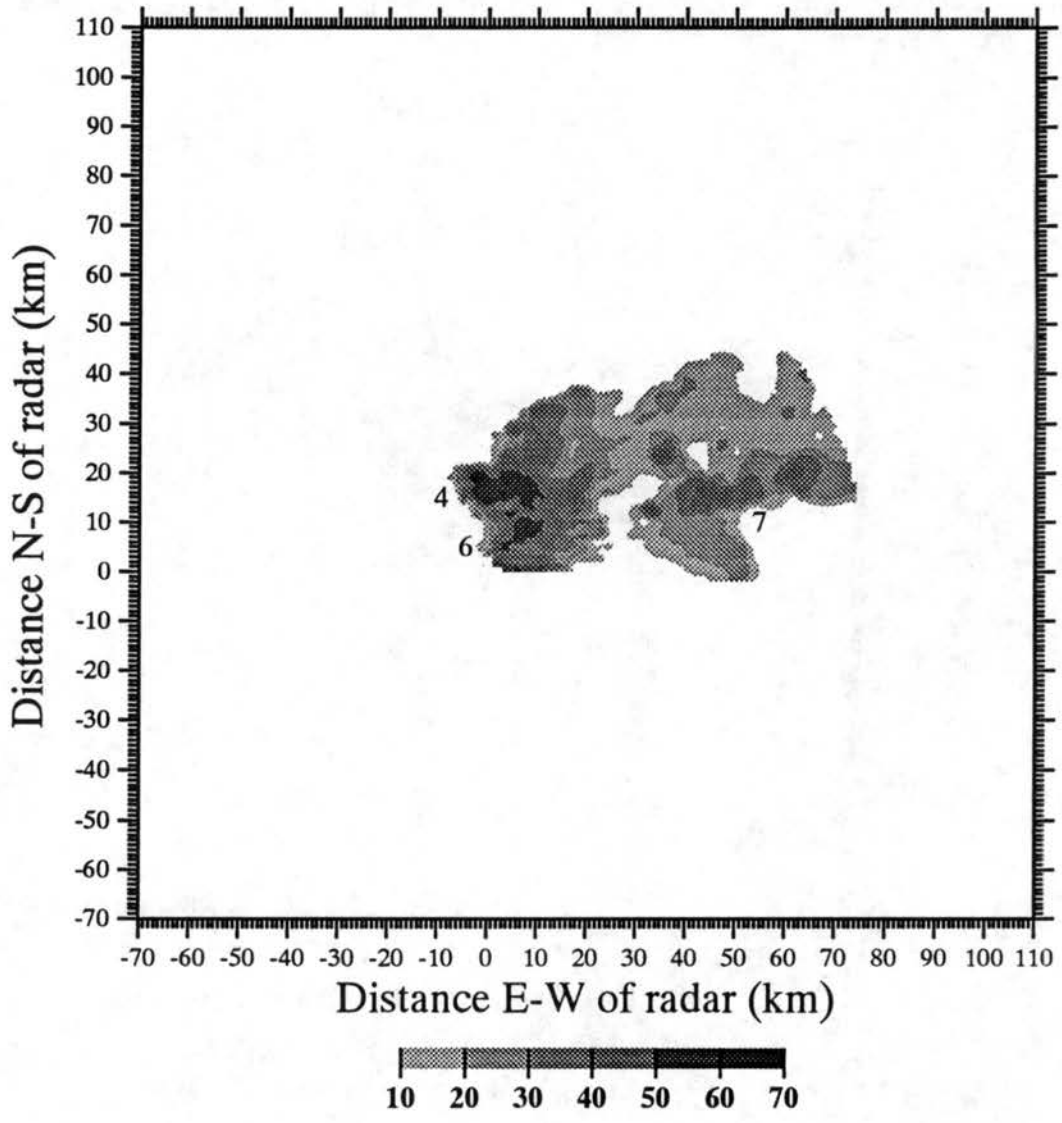

Figure 5.2e: Same as Figure 5.2d except for 1855 MDT.

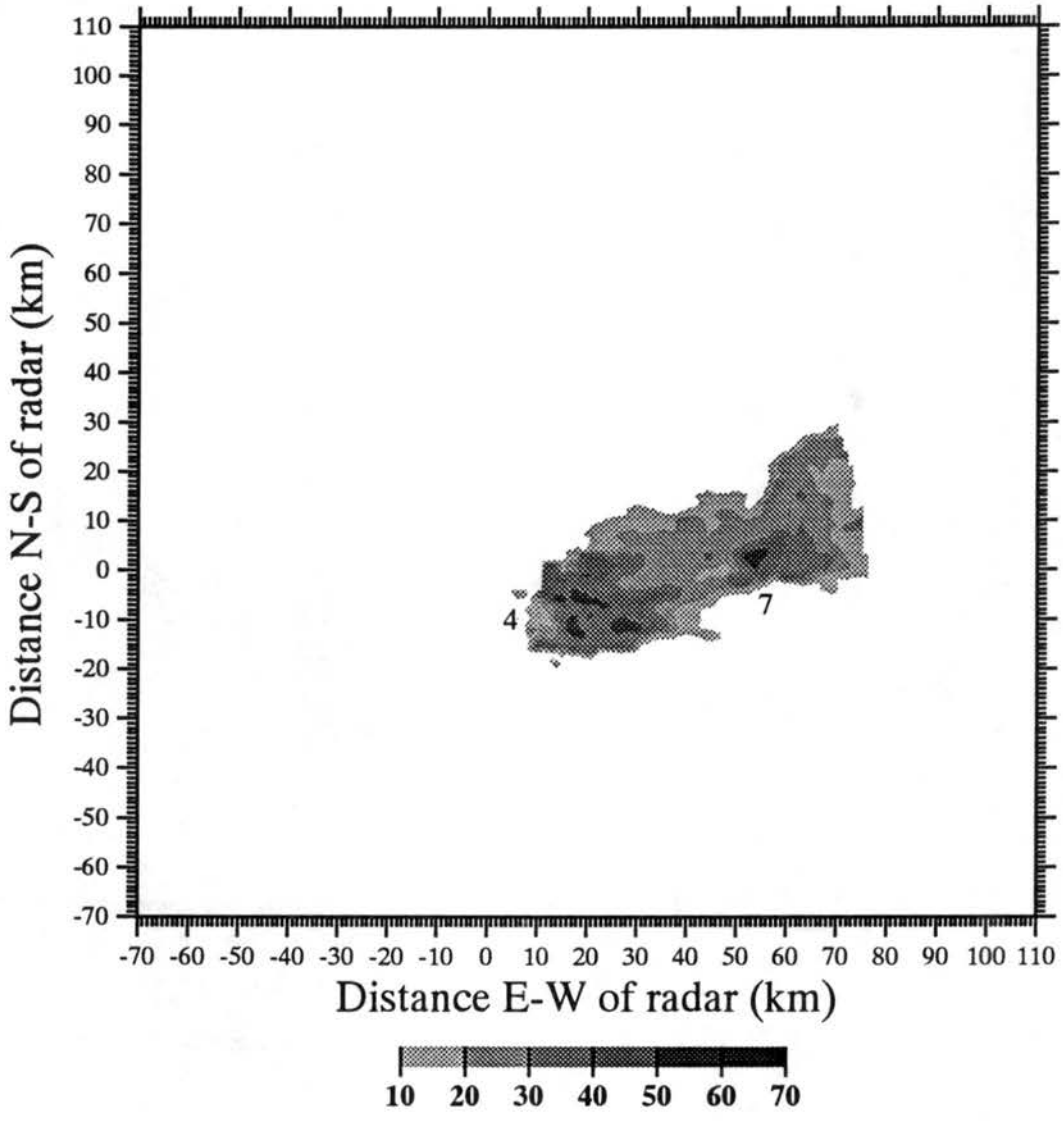

Figure 5.2f: Same as Figure 5.2e except for 1931 MDT.

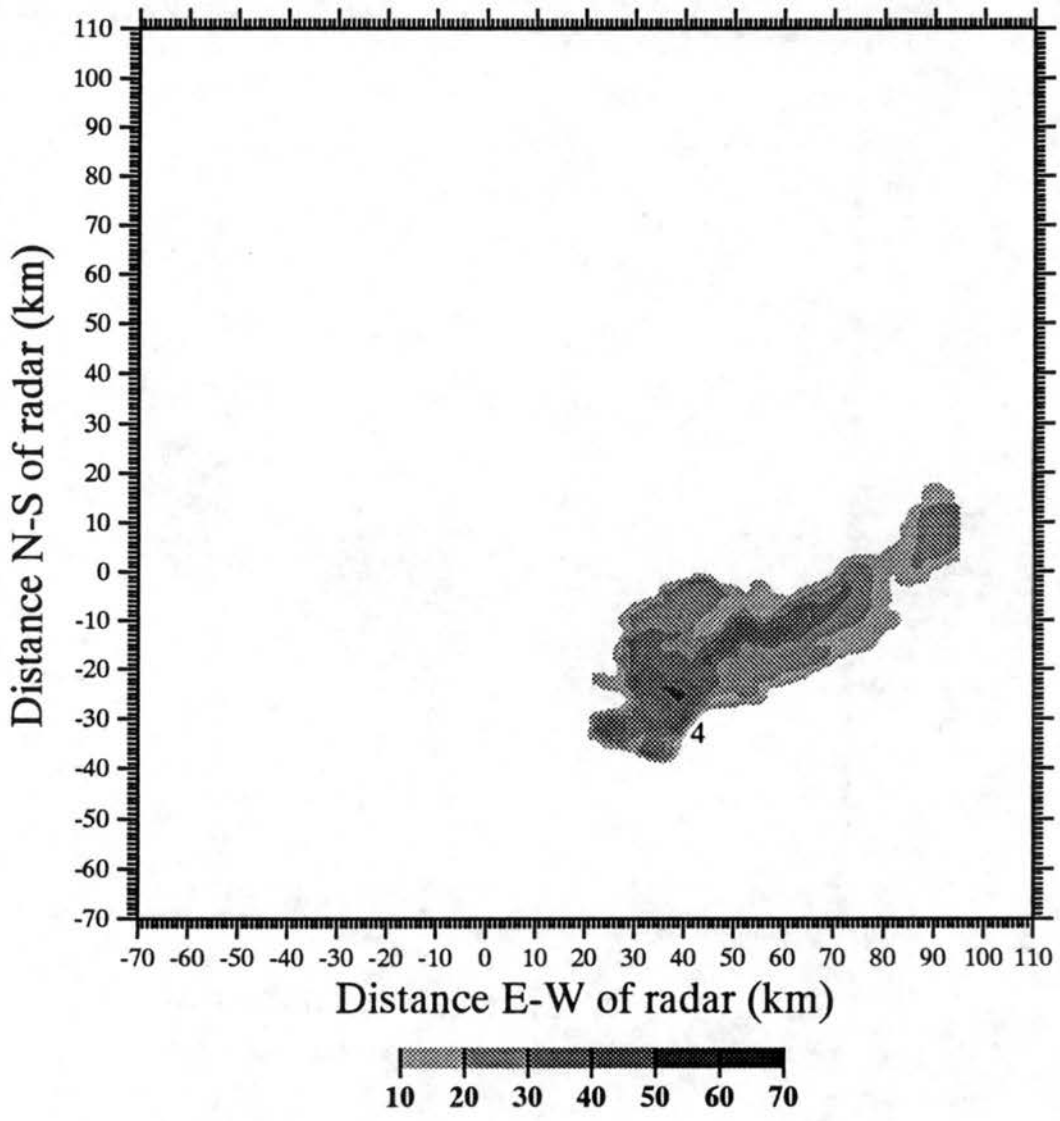

Figure 5.2g: Same as Figure 5.2f except for 1959 MDT.

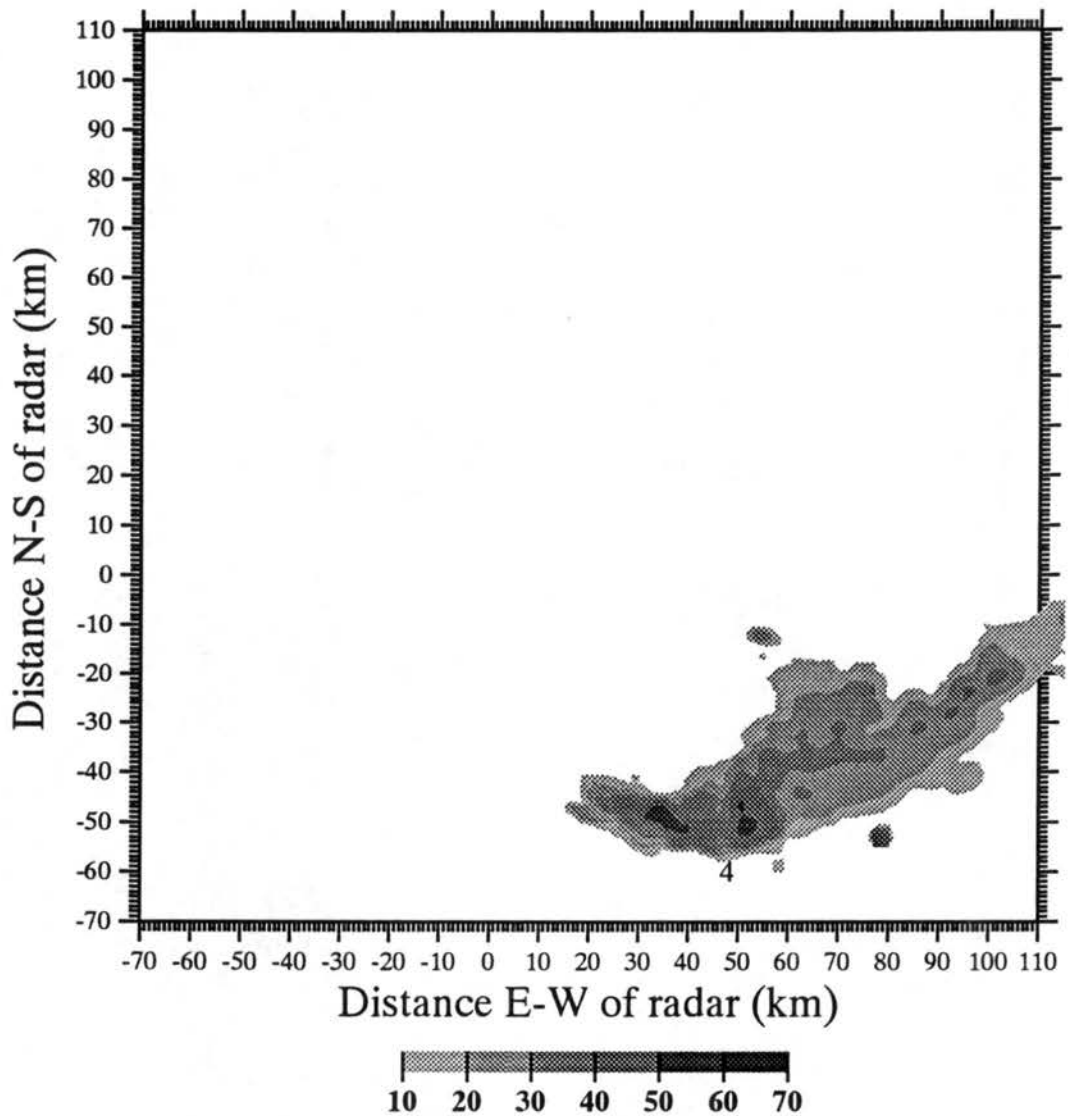

Figure 5.2h: Same as Figure 5.2g except for 2031 MDT.

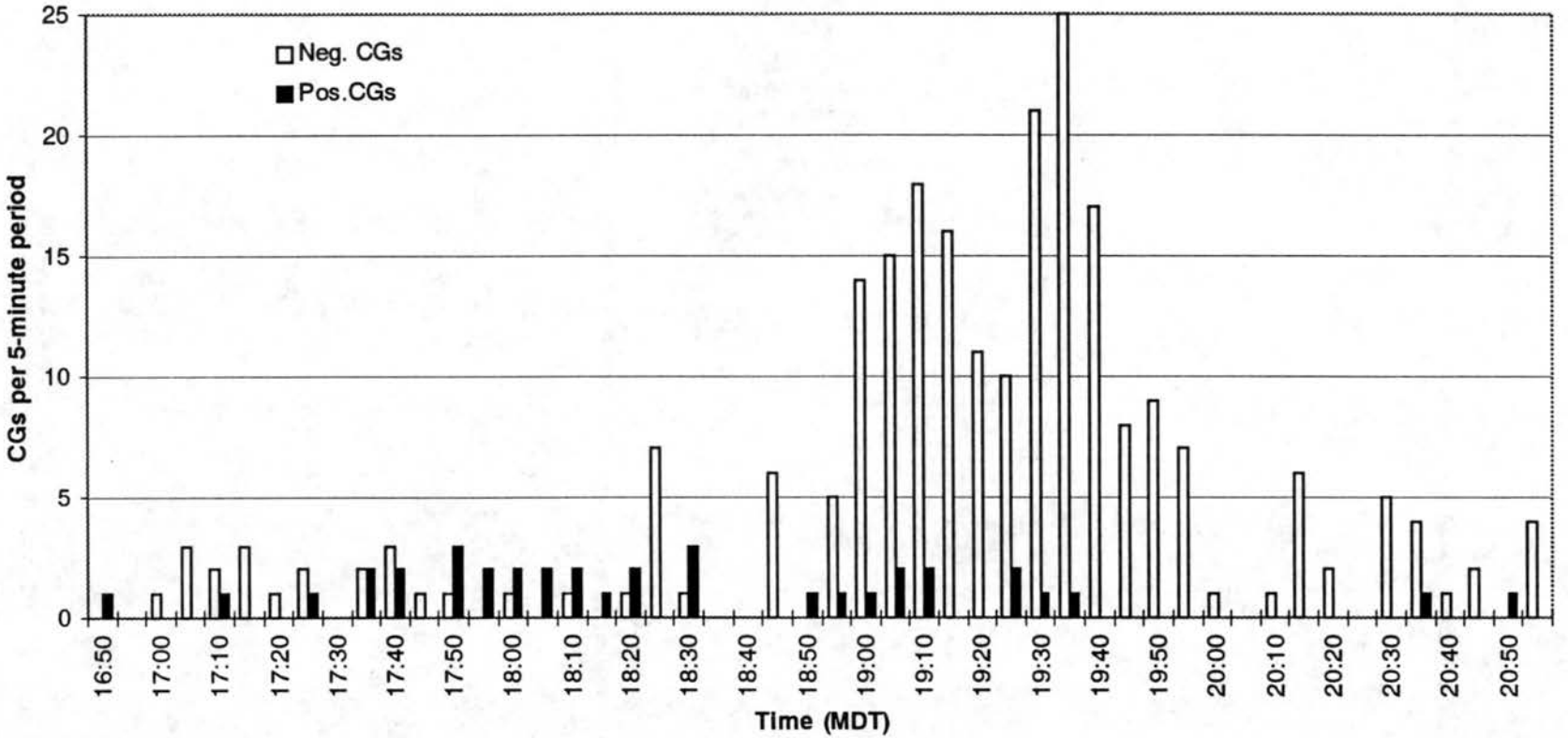

Figure 5.3: Five-minute NLDN CG flash rates for the entire 12 July 1996 storm complex, broken down by polarity.

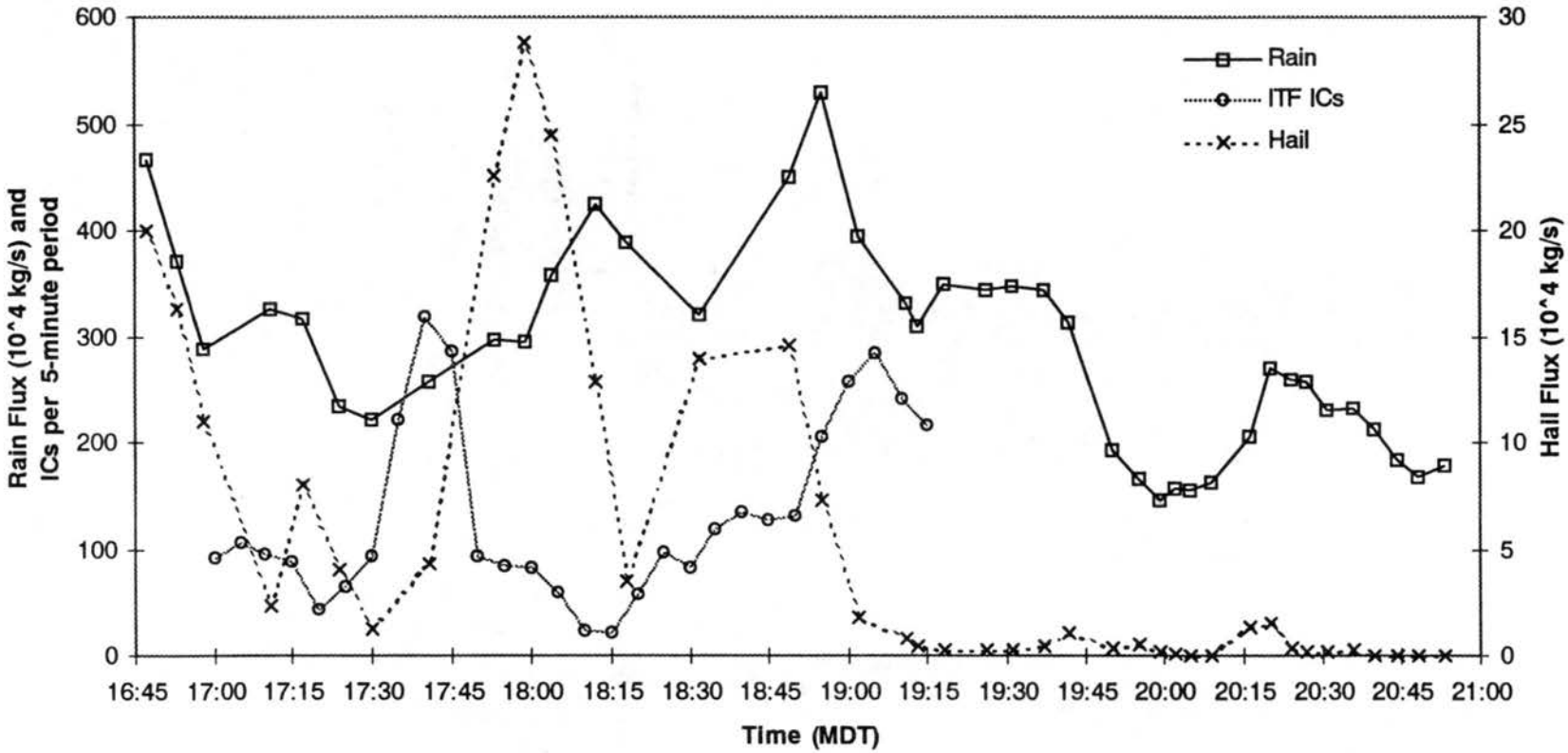

Figure 5.4: Five-minute ITF IC flash rates and radar-inferred rain and hail fluxes at 0.5 km AGL for the entire 12 July 1996 storm complex.

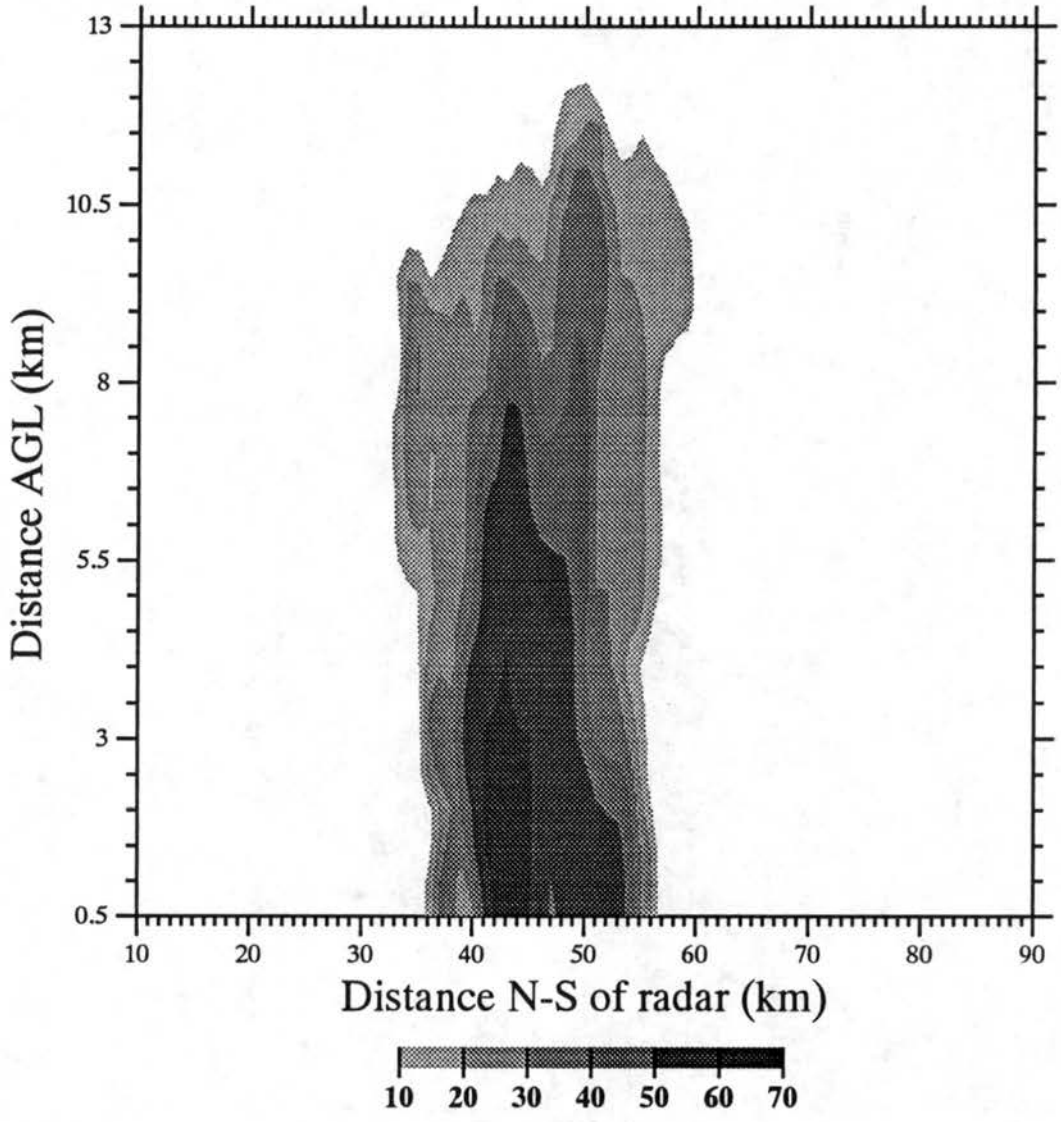

Figure 5.5: Vertical cross-section of radar reflectivity (dBZ) at 11 km west of CHILL for the radar volume beginning at 1804 MDT.

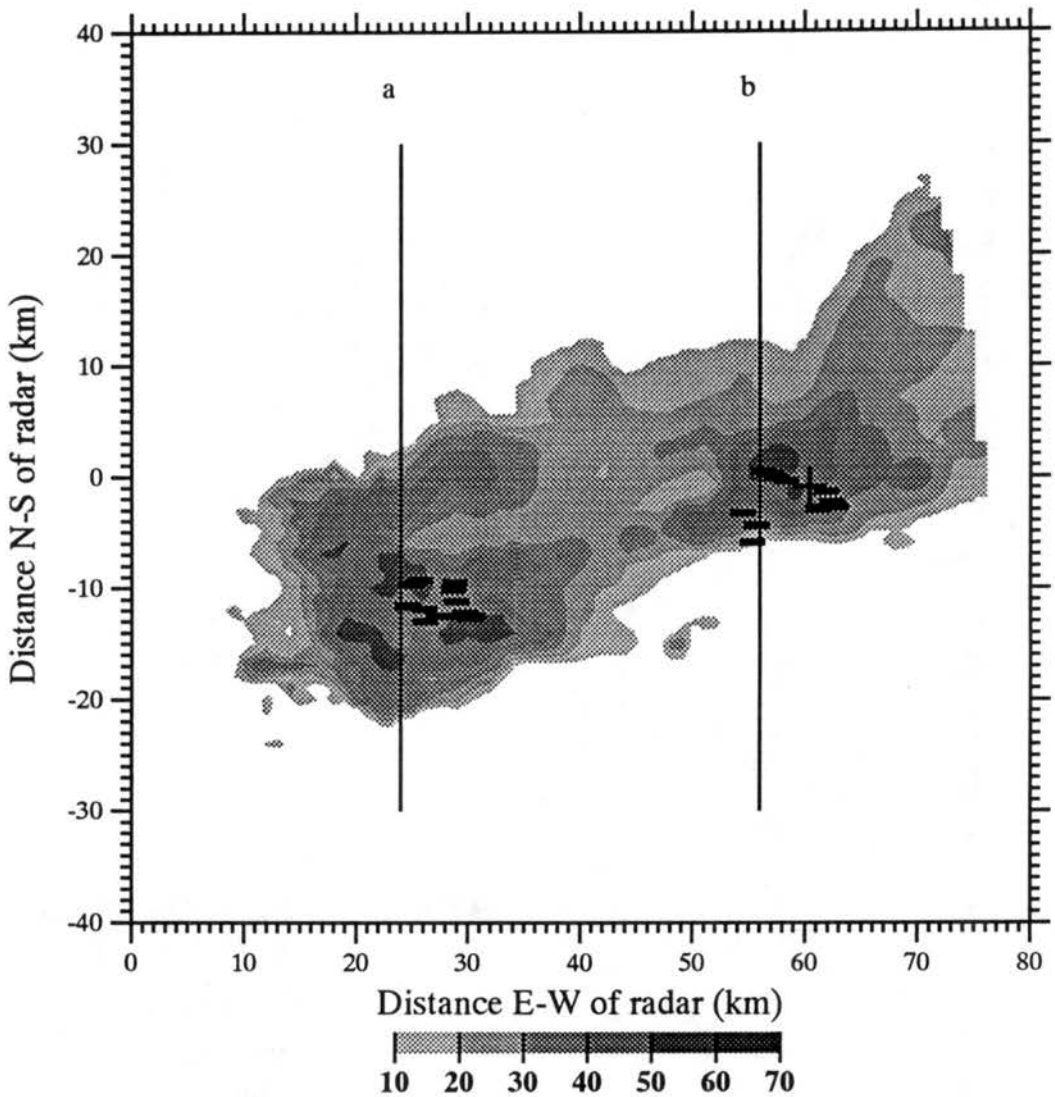

Figure 5.6: Horizontal cross-section of radar reflectivity (dBZ) at 0.5 km AGL for the radar volume beginning at 1937 MDT. Also plotted are the ground strike locations of NLDN-detected CG lightning that occurred during the duration of the volume scan. Plus signs refer to positive CGs, and minus signs to negative CGs. The lines denote the positions along which the vertical cross-sections in Figures 5.7 (a-b, respectively) are taken.

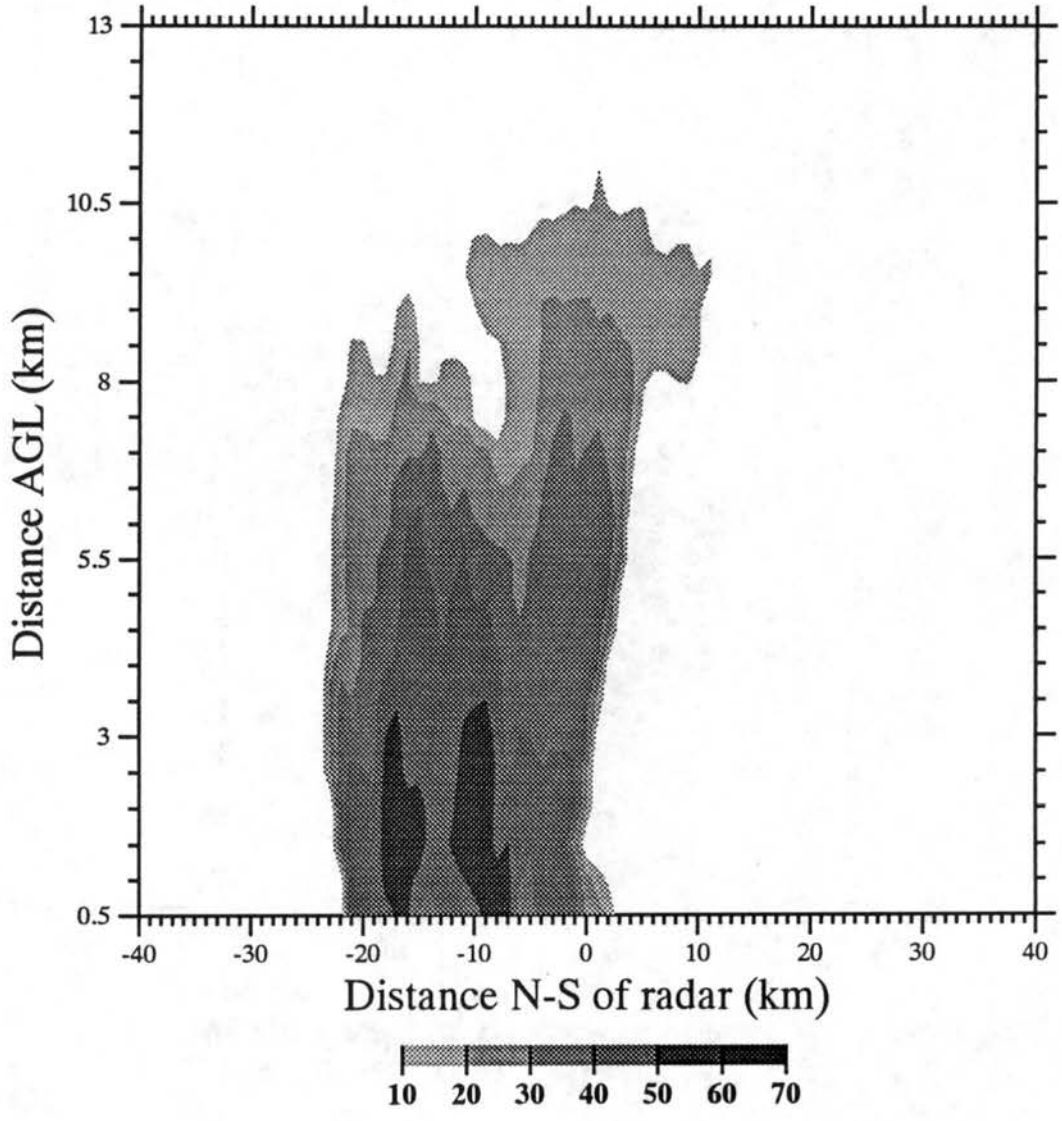

Figure 5.7a: Vertical cross-section of radar reflectivity (dBZ) at 24 km east of CHILL for the radar volume beginning at 1937 MDT.

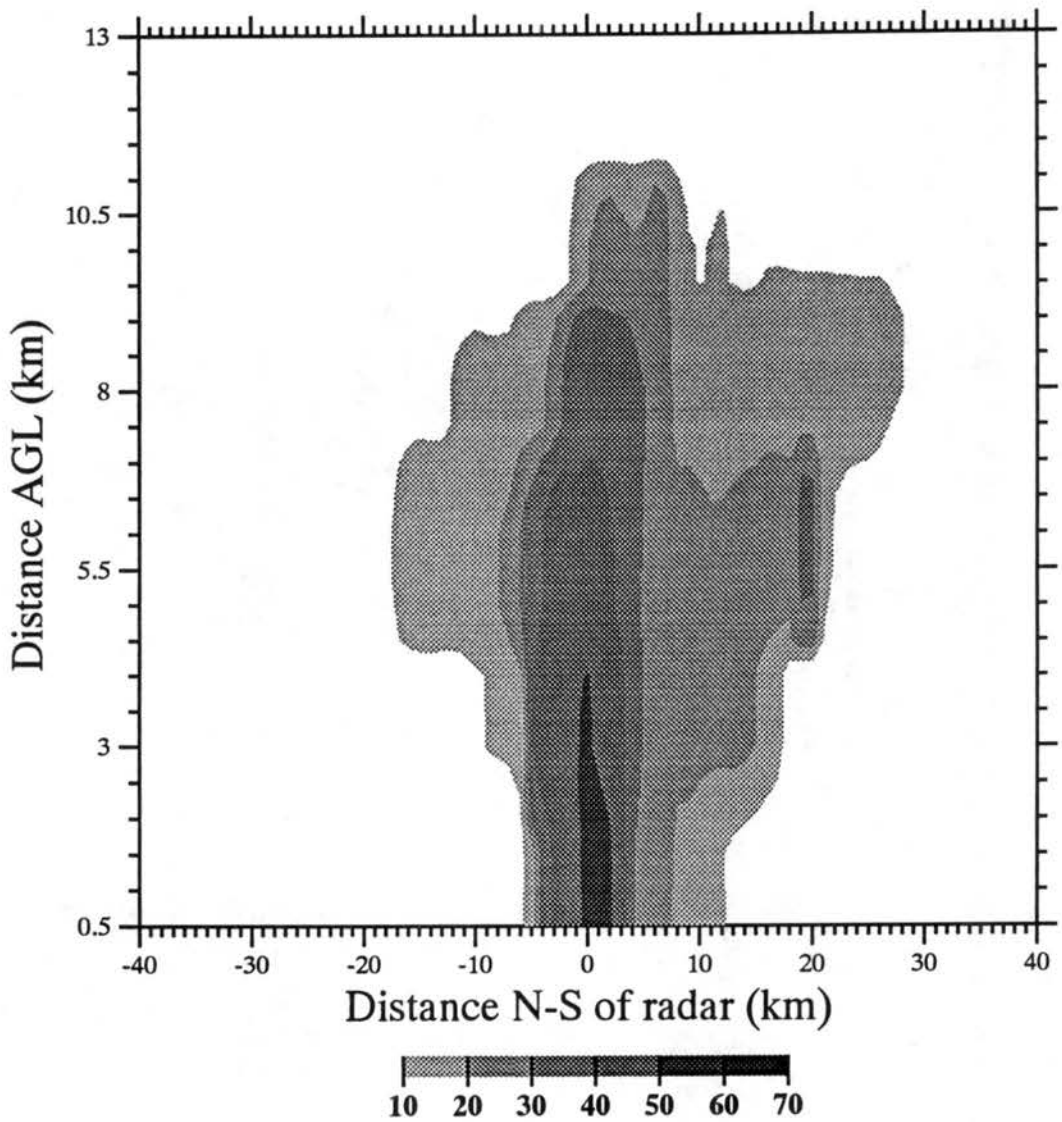

Figure 5.7b: Vertical cross-section of radar reflectivity (dBZ) at 56 km east of CHILL for the radar volume beginning at 1937 MDT.

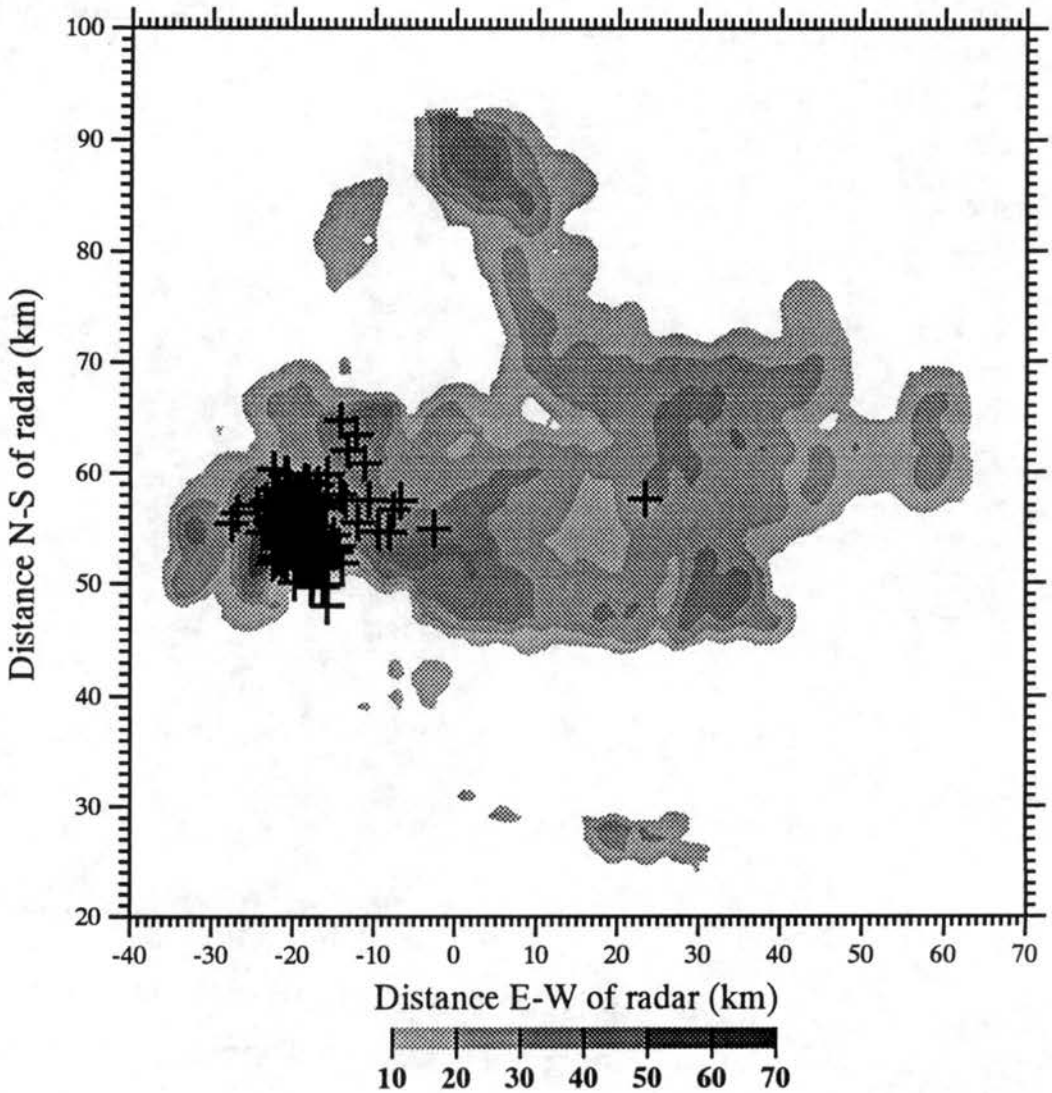

Figure 5.8a: Horizontal cross-section of radar reflectivity (dBZ) at 0.5 km AGL for the radar volume beginning at 1741 MDT. Also plotted are the mean horizontal positions of ITF-detected IC lightning that occurred during the volume scan.

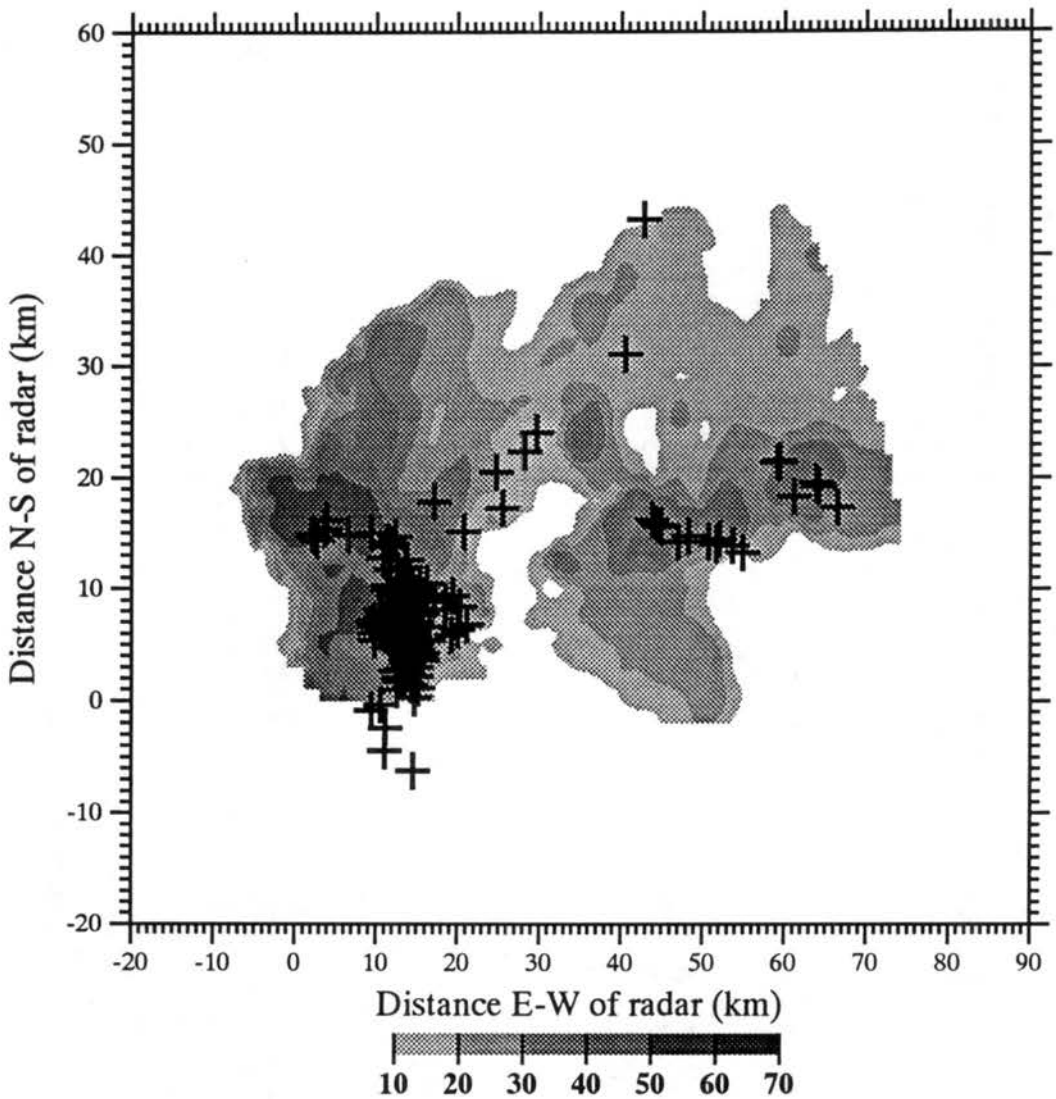

Figure 5.8b: Horizontal cross-section of radar reflectivity (dBZ) at 0.5 km AGL for the radar volume beginning at 1855 MDT. Also plotted are the mean horizontal positions of ITF-detected IC lightning that occurred during the volume scan.

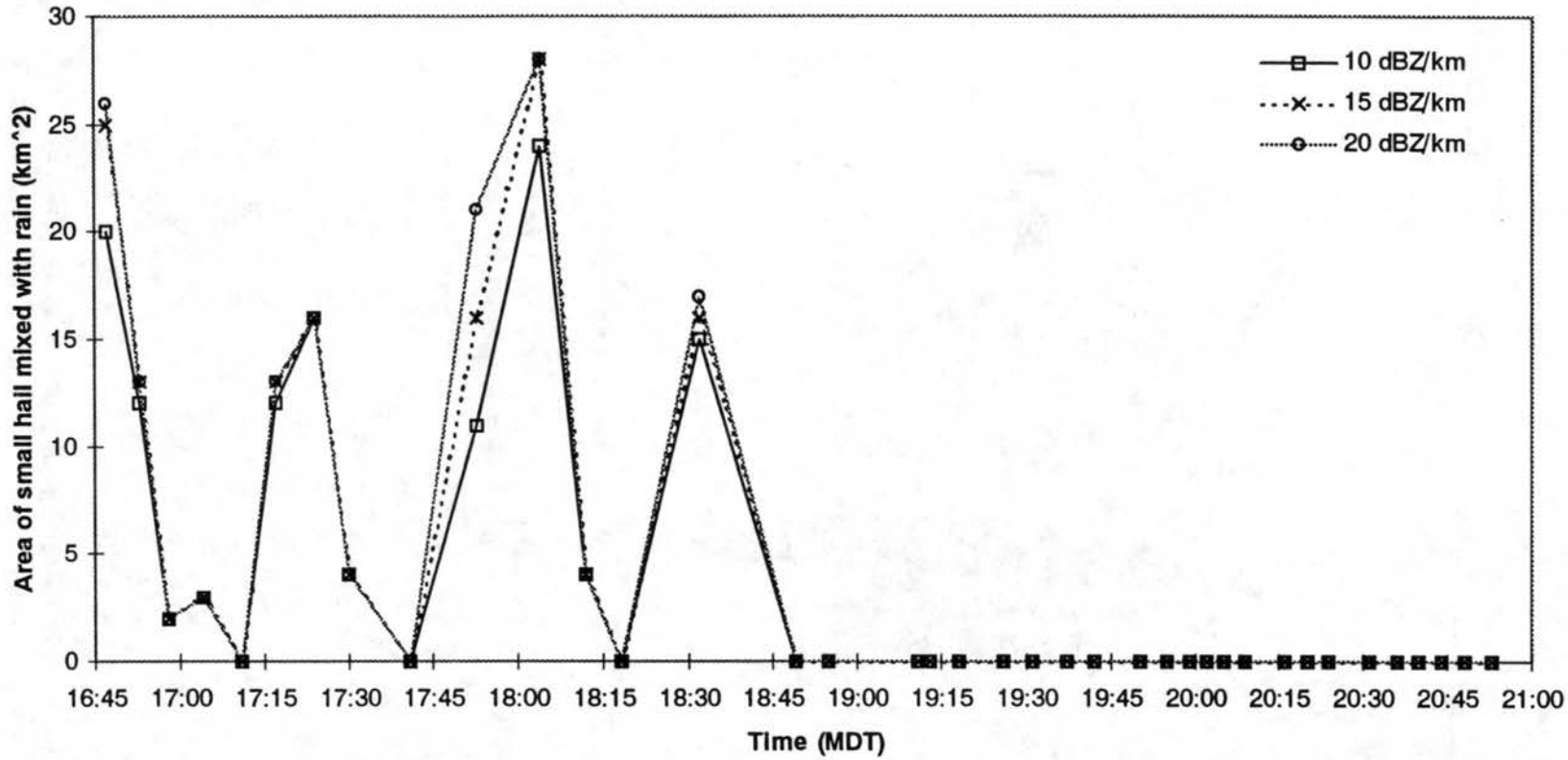

Figure 5.9: Comparison of radar-inferred areal coverages at 0.5 km AGL of small hail mixed with rain, computed using three different reflectivity gradient thresholds.

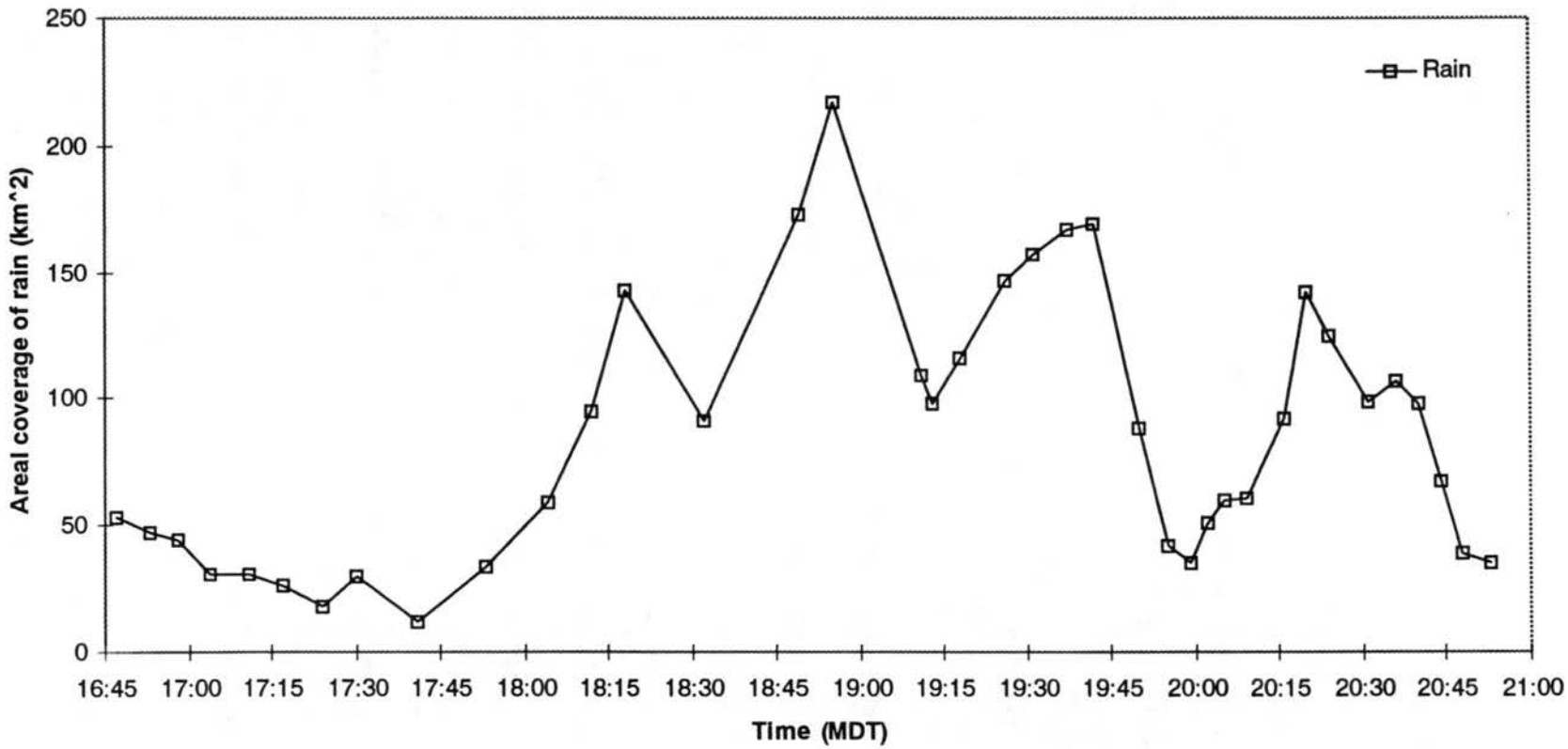

Figure 5.10: Radar-inferred areal coverage of rain at 0.5 km AGL for the 12 July 1996 storm.

CHAPTER 6

DISCUSSION AND CONCLUSIONS

6.1 Analysis of possible mechanisms for low CG production in intense storms

Two case studies of the relationships between the multiparameter radar-inferred microphysics of convective storms and associated lightning have been presented. Both case studies involved thunderstorms which underwent major transitions in structure and intensity sometime during their lifetimes. Emphasis was placed on examining these major transitions to better understand the relationships between microphysics and lightning, especially to examine hypotheses to explain low cloud-to-ground (CG) flash rates in certain intense convective storms. The case studies utilized data from the CSU-CHILL multiparameter Doppler radar, the ONERA VHF lightning interferometer (ITF), and the National Lightning Detection Network (NLDN). The CHILL radar was used to characterize storm structure and to infer both rain and hail rates, and also to differentiate between regions of different bulk precipitation types. The ITF was used to infer intra-cloud (IC) flash rates, while the NLDN provided CG flash rates and ground strike locations.

The storm of 10 July 1996 underwent a major transition approximately halfway through the observation period, evolving from a multicellular line to an intense unicellular storm which featured some characteristics common to supercells, such as mid-level rotation and a Weak Echo Region (WER). Throughout this storm's lifetime CG flash rates were

extremely low, averaging 0-2 CG flashes per 5-minute period. During the peak CG flash rate period flashes typically were associated with less intense (in terms of vertical radar reflectivity structure) cells along the line, while the most intense cells were associated with the bulk of the IC flashes. During the storm's intense unicellular stage, CG production was zero, while IC flash rates peaked near 50 per minute. In general, IC flash rates trended the low-level precipitation fluxes well, although occasionally these fluxes lagged the IC flash rates. Small (< 2 cm) hail was produced throughout the storm's lifetime, though overall precipitation fluxes were significantly lower compared to other intense storms (Carey and Rutledge, 1997).

The storm of 12 July 1996 underwent a major transition from an intense, hail-producing multicellular storm to a weaker multicellular rainstorm with little or no hail production. Before this transition, CG flash rates were low (for both positive and negative polarity flashes), averaging less than 5 per 5-minute period. Afterward, negative CG flash rates rose significantly, to 25 per 5-minute period at their peak. IC flash rate led the fallout of significant precipitation early in the storm's lifetime, but afterward it lagged the low-level precipitation fluxes. This may be due to the superposition of the contributions from multiple cells to these parameters, which could obscure the usual single-cell trend of IC flash rates leading the fallout of significant precipitation (e.g., Williams et al., 1989a,b). When hail was produced by this storm, it was predominantly small hail. Overall, precipitation fluxes seemed comparable to the fluxes seen by Carey and Rutledge (1997). However, Carey and Rutledge (1997) studied a storm that produced significant quantities of radar-detected large hail, unlike 10 and 12 July 1996.

There are some interesting features common to both of these storms. One is that when hail was produced by either storm, even if such production underwent significant pulsing, CG flash rates were low. Another common feature is that CGs were most often associated with weaker cells, in terms of the vertical structure of radar reflectivity and the lack of hail production. The most intense cells typically were associated with the bulk of the IC production. A final common aspect is that, especially when CG flash rates were low, these storms did not seem to follow the common pattern, established by other researchers (Williams et al., 1989a,b; Carey and Rutledge, 1996; Changnon, 1992), of CG flash rates peaking when significant precipitation reached the ground. In fact, CG production was so low during these times that it was difficult to resolve any trends at all. CG flash rates remained low regardless of whether individual cells were developing or collapsing. Only when hail production was largely terminated, on 12 July, did CG rates increase. On 10 July, when hail production was terminated the storm itself collapsed, and no final burst of CGs occurred.

Based on this evidence, the elevated dipole hypothesis (MacGorman and Nielsen, 1991) seems to be a reasonable explanation for the low production of CGs. In cells producing the most CGs, the available proxy data imply weaker updrafts than in cells producing little or no CGs. In the CG-producing cells, vertical reflectivity structure was weaker, in that high radar reflectivity contours either did not exist or extended to lower altitudes than the most intense, low-CG cells. The existence of hail is another proxy for updraft strength, in that intense updrafts are needed for hail production to occur. Thus, if there is little or no hail being produced - as during the latter half of the 12 July storm's lifetime - this implies weaker updrafts, on average, than a hail-producing storm.

Recall that the elevated dipole mechanism involves intense updrafts shifting the negative charge region of the storm (e.g., Williams, 1989) to higher altitudes than average updrafts would suspend this charge region (MacGorman and Nielsen, 1991). This higher altitude should then disfavor CGs, due to the reduced (on average) electric field between the negative charge region and ground. However, based on either convective or precipitation-based charging theories, substantial charging should still be occurring, owing to the intense updraft. Thus, IC flash rates should be higher than an ordinary (i.e., single-cell or non-severe multicell) storm, especially since the charge neutralization process provided by CG flashing is reduced.

These enhanced IC flash rates may be the reason that CGs still are not produced in even moderate quantities when individual cells reach maturation in the storms of 10 and 12 July. High IC flash rates could have served to neutralize most of the produced charge before it began its descent. With reduced charge on the descending precipitation, CGs could be suppressed.

It may be illustrative to view these two storms as points on a continuum of updraft speeds. On one end there are the cells with very weak updrafts and which produce little or no lightning of any type. Then, further along the updraft scale, there would be the "garden-variety" storms, whose individual cells favor average IC lightning flash rates in their developing stages, but once their cores reach ground the production of CG lightning occurs. These are the type of thunderstorms that Williams et al. (1989a,b) and others studied. They may or may not produce hail, but if they do so, it would be only a very small component of the precipitation flux. Then there would be storms like those of 10 and 12 July, with strong updrafts and high IC flash rates, but relatively low CG lightning

production. These storms produce mostly small hail. Then, at the most extreme end, there are the intense severe storms which produce significant quantities of large hail and positive CG lightning, such as those studied by Carey and Rutledge (1997) and others. In these storms, updraft strengths may be so high that large quantities of positive charge are created and then deposited in the upper levels of the storms. This enhanced region of positive charge would provide a source for positive-polarity CGs, despite the high IC flash rates observed in these cases.

This continuum idea is especially consistent with the present cases, since positive CG lightning was present in both storms, though in smaller quantity than the storms studied by Carey and Rutledge (1997) and others. In the storms of 10 and 12 July, positive CGs, when they occurred, were typically associated with the most intense cells, which made the fraction of positive CGs produced by the most intense cells very high (~ 50% or more), even though their overall CG production was low. Perhaps, with somewhat stronger updrafts and greater longevity in the severe phase, these storms could have become significant positive CG producers themselves.

If one accepts the results of Saunders et al. (1991) and Saunders and Brooks (1992), and significant charging does not occur in wet-growth regimes, then the storms of 10 and 12 July might have produced enough wet-growth hail to prevent the production of a lower positive charge region (below the main negative charge region), whose existence is thought to stimulate CG lightning activity (Clarence and Malan, 1957; Williams et al., 1985; Williams et al., 1989a). Hence this is another mechanism that may account for the paucity of CGs in these storms. In even stronger storms such as the one studied by Carey and Rutledge (1997), wet growth may be more prevalent, and this mechanism would act

more efficiently. Though the available observations imply that hail undergoing wet growth was certainly a possibility - indeed a likelihood - in these two storms, the observations also imply that the dry growth regime was more prevalent, due to the paucity of extended regions of enhanced LDR. Note that, because the identification of hail above the freezing level with multiparameter radar data is still in an exploratory stage (e.g., Kennedy et al., 1997), and because there are no in situ data available, this mechanism cannot be totally ruled out. If this mechanism were operating, no significant lower positive charge region should have formed, which could account for the low CG production of these storms. It would be consistent with the rise in CGs after hail fall ended in the 12 July storm, since then there should be little or no wet growth occurring, as hail was not present in bulk. Thus, during the latter half of the 12 July storm, a lower positive charge region could have formed and CGs once again would have been favored.

Note that this wet growth mechanism is compatible with the elevated dipole mechanism, and in fact could act in concert with the latter mechanism to suppress CGs. However, the lack of charging during wet growth observed by Saunders et al. (1991) and Saunders and Brooks (1992) is in contradiction with the laboratory results of Takahashi (1978), especially as interpreted by Williams et al. (1991), who found significant charging during probable wet-growth regimes. The debate over which results are correct is still ongoing.

It is difficult to rule out the possibility that the precipitation current could provide a feasible substitute for the CG lightning current, since charge on precipitation was not measured during STERAO-A. However, as noted in Chapter 1, several researchers have made estimates of the magnitudes of both precipitation currents (Rust and Moore, 1974;

Moore, 1976; Moore and Vonnegut, 1977; Gaskell et al., 1978, Marshall and Winn, 1982; Soula and Chauzy, 1996; Baranski, 1996) and CG lightning currents (Livingston and Krider, 1978; Krehbiel, 1981). Given the wide range of estimates for both types of current, it seems possible that precipitation current could become high enough (provided precipitation fluxes are high) to transfer significant charge to ground and suppress CG lightning. Precipitation fluxes were relatively high for the storm of 12 July, but were much lower during the 10 July storm. For both of these storms the major contributor to the precipitation flux was rain. The rain probably is not contributing enough to the precipitation current to cause suppression of CGs, as rain rates for 12 July were significant both before and after the major transition in the storm. Also, these rain rates were much higher than those that occurred during 10 July, which also featured low CG flash rates. Thus, any hypothesis that invokes the precipitation current due to rain to account for low CG rates faces these counterpoints.

However, what if the hailstones were charged? As noted before, negative CG production is negatively correlated, in a bulk sense, with the production of hail. If the *hail*stones themselves were negatively charged, then the observed hail fluxes may be large enough that the precipitation current due to hail would help suppress CG lightning. The hail fluxes from either storm are typically within a factor of two of one another, so given the possible error involved in these flux calculations there may not be so much difference between the two days. However, note that this hypothesis requires that the hailstones be charged, in contradiction to the hypothesis based on the results of Saunders et al. (1991) and Saunders and Brooks (1992) which contend that hail which underwent significant wet growth would not be charged. Thus, resolving this contradiction would require that the

bulk of hail growth for these storms occur in the dry regime. Based on the available data this probably occurred. However, note that hail probably is not a significant contributor to the overall precipitation current because of its typically low number concentrations (Cheng and English, 1983). Graupel should be the dominant charge carrier because it usually is in higher concentration. Note that if most of the graupel melted before reaching the ground, this charge would be carried by the subsequent rain. This perhaps is an argument for rain being the principle charge carrier in these types of storms (i.e., storms like 10 and 12 July wherein most of the precipitation appears to be in the form of rain, regardless of whether hail is produced or not).

Based on this research, it appears that the exact mechanism(s) responsible for low production of CG flashes in certain intense convective storms is still unclear. The elevated dipole mechanism, in conjunction with increased IC flash rates, is perhaps the simplest explanation available, in that it does not require precipitation to carry any specific charge or lack thereof. It also is entirely consistent with the available evidence. However, other mechanisms may be active, either instead of or in concert with the elevated dipole mechanism.

Nevertheless, this study provides additional documentation of the phenomenon of low CG production in intense storms. It also establishes that the production of negative CGs can be inversely correlated - in a bulk sense - with the production of significant quantities of hail and probably also with the potential for severe weather, in these types of storms.

6.2 Recommendations for future research

The main limitations of the present study include the small number of case studies, the lack of direct data on updraft speeds, the lack of measurements of net charge on hydrometeors, and uncertainties in the interferometer data.

To better establish (or perhaps to refute) the results of the present study, more combined radar and lightning case studies of major transitions in convective storm structure are needed. Alternatively, case studies involving a spectrum of different convective storm types and strengths could be examined and contrasted, to provide more insight into what is causing any observed differences in lightning patters. Critical to such studies is the existence of IC flash data, since these data help to establish the extent to which a storm is electrified, and also provide evidence as to what portion of its life cycle (e.g., initial development, maturation, decay) a given cell is occupying. It is especially useful to have either interferometric (as in the present study) or time-of-arrival (e.g., Proctor, 1981) VHF lightning mapping systems, as these sensors locate lightning in three dimensions This allows for discerning the individual contributions of existing cells to the total storm flash rate.

Future studies also would benefit from direct data on updraft speeds, such as those provided by dual-Doppler radar syntheses. The NOAA WP-3D aircraft which flew during STERAO-A gathered dual-Doppler data for a number of storms, including 10 and 12 July. Currently, however, analyses of these data have not been completed so they were not included in the present study. Such data provide a more direct method of ascertaining updraft speeds, without relying on proxy data like vertical reflectivity structure and hail production.

A way to determine the relative magnitudes of the precipitation currents would be to make in situ observations of the net electrical charge on individual precipitation particles, to gain a sense of the average charge carried per hydrometeor. Using precipitation fluxes and size distribution information, estimates of precipitation currents could be made based on these individual charge measurements. Alternatively, a method to measure precipitation current in a bulk sense - perhaps along the lines of Soula and Chauzy (1996), Baranski (1996), or others - could be used. Data on precipitation currents could be used in conjunction with parameters such as lightning currents, displacement currents, and others to develop complete electrical budgets for a selection of low CG production storms. These budgets could be used to ascertain the relative magnitudes of the lightning and precipitation currents, to better understand if precipitation current could act to suppress CG lightning.

There are still several unknowns regarding the observations of the ONERA VHF lightning interferometer during STERAO-A. The most important of these is how the reduced vertical resolution during STERAO-A impacted the flash identification and classification algorithm, since this algorithm reconstructs individual flashes in three dimensions. The reduced resolution conceivably could impact the estimated VHF burst velocities and separation distances, which could cause the algorithm to produce corrupted flash statistics. This issue will be examined in the future. Also, the nature of the short-duration (< 1 ms) discharges is unknown. They may be a misclassification of individual lightning strokes, or a sub-class of IC discharges, or a combination of both. If they are at least in part a subset of IC discharges, it is not clear what role they would play in either the electrical or chemical budgets of thunderstorms.

REFERENCES

Aydin, K., Seliga, T. A., and V. N. Bringi, 1984: Differential radar scattering properties of model hail and mixed phase hydrometeors. *Radio Sci.*, **19**, 58-66.

Aydin, K., and Y. Zhao, 1990: A computational study of polarimetric radar observables in hail. *IEEE Trans. On GeoSci. and Remote Sensing*, **28**, 412-422.

Balakrishnan, N., and D. S. Zrnic, 1990a: Use of polarization to characterize and discriminate large hail. *J. Atmos. Sci.*, **47**, 1525-1540.

Balakrishnan, N., and D. S. Zrnic, 1990b: Estimation of rain and hail rates in mixed-phase precipitation. *J. Atmos. Sci.*, **47**, 565-583.

Baranski, P., 1996: Precipitation current density at the earth surface accompanying downdrafts from nearby thunderstorms. *Preprints, 10th International Conference on Atmospheric Electricity*, Osaka, Japan, International Commission of Atmospheric Electricity, 112-115.

Billingsley, D. B., and M. I. Biggerstaff, 1994: Evolution of cloud-to-ground lightning characteristics in the convective region of a mesoscale convective region. *Preprints, 5th Symposium on Global Change Studies: Symposium on Global Electrical Circuit, Global Change, and the Meteorological Applications of Lightning*, Nashville, Tennessee, Amer. Meteorol. Soc., 340-344.

Bringi, V. N., Chandrasekar, V., Balakrishnan, N., and D. S. Zrnic, 1990: An examination of propagation effects on radar measurements at microwave frequencies. *J. Atmos. Oceanic Technol.*, **7**, 829-840.

Bringi, V. N., Vivekanandan, J., and J. D. Tuttle, 1986: Multiparameter radar measurements in Colorado convective storms. Part II: hail detection studies. *J. Atmos. Sci.*, **43**, 2564-2577.

Burgess, D. W., and L. R. Lemon, 1990: Severe thunderstorm detection by radar. In *Radar in Meteorology*, D. Atlas, ed., Amer. Meteorol. Soc., Boston, Massachusetts, 619-647.

Carey, L. D., and S. A. Rutledge, 1996: A multiparameter radar case study of the microphysical and kinematic evolution of a lightning producing storm. *Meteorol. Atmos. Phys.*, **59**, 33-64.

Carey, L. D., and S. A. Rutledge, 1997: Electrical and multiparameter radar observations of a severe hailstorm. Accepted in *J. Geophys. Res.*

Chandrasekar, V., Bringi, V. N., Balakrishnan, N., and D. S. Zrnic, 1990: Error structure of multiparameter radar and surface measurements of rainfall. Part III: Specific differential phase. *J. Atmos. Oceanic Technol.*, **7**, 621-629.

Changnon, S. A., 1992: Temporal and spatial relations between hail and lightning. *J. Appl. Meteor.*, **31**, 587-604.

Cheng, L., and M. English, 1983: A relationship between hailstone concentration and size. *J. Atmos. Sci.*, **40**, 204-213.

Clarence, N. D., and D. J. Malan, 1957: Preliminary discharge processes in lightning discharges to ground. *Q. J. R. Meteorol. Soc.*, **83**, 161-172.

Cressman, G. P., 1959: An operational objective analysis system. *Mon. Wea. Rev.*, **87**, 367-374.

Cummins, K. L., Bardo, E. A., Hiscox, W. L., Pyle, R. B., and A. E. Pifer, 1996: A combined TOA/MDF technology upgrade of the U. S. National Lightning Detection Network. *Preprints, 10th International Conference on Atmospheric Electricity*, Osaka, Japan, International Commission of Atmospheric Electricity, 288-292.

Doviak, R. J., and D. S. Zrnic, 1993: *Doppler Radar and Weather Observations*, 2nd Ed., Academic Press, San Diego, California, 562 pp.

Foote, G. B., and H. W. Frank, 1983: Case study of a hailstorm in Colorado. Part III: Airflow from triple Doppler measurements. *J. Atmos. Sci.*, **40**, 686-707.

Frost, I. R., Goddard, J. W. F., and A. J. Illingworth, 1991: Hydrometeor identification using cross polar radar measurements and aircraft verification. *Preprints, 25th Conf. Radar Meteor.*, Paris, France, Amer. Meteorol. Soc., 658-661.

Gaskell, W., Illingworth, A. J., Latham, J., and C. B. Moore, 1978: Airborne studies of electric fields and the charge and size of precipitation elements in thunderstorms. *Q. J. R. Meteorol. Soc.*, **104**, 447-460.

Golestani, Y., Chandrasekar, V., and V. N. Bringi, 1989: Intercomparison of multiparameter radar measurements. *Preprints, 24th Conf. Radar Meteor.*, Tallahassee, Florida, Amer. Meteor. Soc., 309-314.

Herzegh, P. H., and R. E. Carbone, 1984: The influence of antenna illumination function characteristics on deifferential reflectivity measurements. *Preprints, 22nd Conf. Radar Meteor.*, Zurich, Switzerland, Amer. Meteorol. Soc., 281-286.

Holler, H., Bringi, V. N., Hubbert, J., Hagen, M., and P. F. Meischner, 1994: Life cycle and precipitation formation in a hybrid-type hailstorm revealed by polarimetric and Doppler radar measurements. *J. Atmos. Sci.*, **51**, 2500-2522.

Hubbert, J. H., Bringi, V. N., Carey, L. D., and S. Bolen, 1997: CSU-CHILL polarimetric radar measurements from a severe hailstorm in eastern Colorado. Submitted to *J. Appl. Meteor.*

Hubbert, J., Chandrasekar, V., Bringi, V. N., and P. Meischner, 1993: Processing and interpretation of coherent dual-polarized radar measurements. *J. Atmos. Oceanic Technol.*, **10**, 155-164.

Jameson, A. R., 1985: Microphysical interpretation of multiparameter radar measurements in rain. Part III: interpretation and measurement of propagation differential phase shift between orthogonal linear polarizations. *J. Atmos. Sci.*, **42**, 607-614.

Jones, D. M. A., 1955: 3 cm and 10 cm wavelength radiation backscatter from rain. *Proc. 5th Wea. Radar Conf.*, Boston, Massachusetts, Amer. Meteorol. Soc., 281-285.

Kennedy, P. C., and S. A. Rutledge, 1995: Dual-Doppler and multiparameter radar observations of a bow-echo hailstorm. *Mon. Wea. Rev.*, **123**, 921-943.

Kennedy, P. C., Rutledge, S. A., and V. N. Bringi, 1997: Hail precursor signatures observed in multiparameter radar data. *Preprints, 28th Conf. Radar Meteor.*, Austin, Texas, Amer. Meteorol. Soc.

Knight, C. A., and N. C. Knight, 1970: The falling behavior of hailstones. *J. Atmos. Sci.*, **27**, 672-681.

Krehbiel, P. R., 1981: An analysis of the electric field change produced by lightning. Ph.D. dissertation, U. Manchester Inst. Of Sci. & Tech., also published as Rpt. T-11, New Mex. Inst. Min. & Tech., Dec., 1981, 246 pp. + Vol. 2 of figures.

Lang, T. J., Rutledge, S. A., Dye, J. E., and P. Laroche, 1997: An investigation of the relationship between the microphysics of convective storms and their lightning activity. *Preprints, 28th Conf. Radar Meteor.*, Austin, Texas, Amer. Meteorol. Soc.

Laroche, P., Bondiou, A., Blanchet, P., Pigere, J., Weber, M., and B. Boldi, 1994: 3D mapping of lightning discharge within storms. *International Aerospace and Ground Conf. on Lightning and Static Electricity*, Mannheim, Germany.

Livingston, J. M., and E. P. Krider, 1978: Electric fields produced by Florida thunderstorms. *J. Geophys. Res.*, **83**, 385-401.

MacGorman, D. R., and K. E. Nielsen, 1991:Cloud-to-Ground lightning in a tornadic storm on 8 May 1996. *Mon. Wea. Rev.*, **119**, 1557-1574.

Maddox, R. A., Howard, K. W., and C. L. Dempsey, 1997: Intense convective storms with little or no lightning over Central Arizona: a case of indavertent weather modification? *J. Appl. Met.*, **36**, 302-314.

Maier, L., Lennon, C., Krehbiel, P., and M. Maier, 1996: Lightning as observed by a four-dimensional lightning location system at Kennedy Space Center. *Preprints, 10th International Conference on Atmospheric Electricity*, Osaka, Japan, International Commission of Atmospheric Electricity, 280-283.

Marshall, T. C., and W. P. Winn, 1982: Measurements of charged precipitation in a New Mexico thunderstorm: lower positive charge centers. *J. Geophys. Res.*, **87**, 7141-7157.

Mazur, V., Williams, E., Boldi, R., Maier, L., and D. E. Proctor, 1997: Initial comparison of lightning mapping with operational time-of-arrival and interferometric systems. *J. Geophys. Res.*, **102**, 11071-11085.

Moore, C. B., 1976: Reply (to "Further comments on Moore's criticisms of precipitation theories of thunderstorm electrification" by B. J. Mason). *Q. J. R. Meteorol. Soc.*, **102**, 935-939.

Moore, C. B., 1977: An assessment of thunderstorm electrification mechanisms. In *Electrical Processes in Atmospheres*, N. Dolezalek and R. Reiter, eds., Steinkopff, Darmstadt, 333.

Moore, C. B., and B. Vonnegut, 1977: The thundercloud. In *Lightning, Vol. 1: Physics of Lightning*, R. H. Golde, ed., Academic Press, San Diego, California, 64-98.

Mueller, E. A., Rutledge, S. A., Bringi, V. N., Brunkow, D., Kennedy, P. C., Pattison, K., Bowie, R., and V. Chandrasekar, 1995: CSU-CHILL radar upgrades. *Preprints, 27th Conf. Radar Meteor.*, Vail, Colorado, Amer. Meteorol. Soc., 703-706.

Orville, R. E., 1991: Calibration of a magnetic direction finding network using measured triggered lightning return stroke peak currents. *J. Geophys. Res.*, **96**, 17135-17142.

Oye, R., and R. E. Carbone, 1981: Interactive Doppler editing software. *Preprints, 20th Conf. Radar Meteor.*, Boston, Massachusetts, Amer. Meteorol. Soc., 683-689.

Proctor, D. E., 1981: VHF radio pictures of cloud flashes. *J. Geophys. Res.*, **86**, 4041-4071

Pruppacher, H. R., and K. V. Beard, 1970: A wind tunnel investigation of the internal circulation and shape of water drops falling at terminal velocity in air. *Q. J. R. Meteorol. Soc.*, **96**, 247-256.

Rhodes, C. T., Shao, X. M., Krehbiel, P. R., Thomas, R. J., and C. O. Hayenga, 1994: Observations of lightning phenomena using radio interferometry. *J. Geophys. Res.*, **99**, 13059-13082.

Richard, P., and G. Auffray, 1985: VHF-UHF interferometric measurments: applications to lightning discharge mapping. *Radio Sci.*, **20**, 171-192.

Rust, W. D., and C. B. Moore, 1974: Electrical conditions near the bases of thunderclouds over New Mexico. *Q. J. R. Meteorol. Soc.*, **100**, 450-468.

Sachidananda, M., and D. S. Zrnic, 1987: Rain rate estimates from differential polarization measurements. *J. Atmos. Oceanic Technol.*, **4**, 588-598.

Saunders, C. P. R., and I. M. Brooks, 1992: The effects of high liquid water content on thunderstorm charging. *J. Geophys. Res.*, **97**, 14671-14676.

Saunders, C. P. R., Keith, W. D., and R. P. Mitzeva, 1991: The effect of liquid water on thunderstorm charging. *J. Geophys. Res.*, **96**, 11007-11017.

Soula, S., and S Chauzy, 1996: Slow charge transfer by precipitation between thundercloud and ground. *Preprints, 10th International Conference on Atmospheric Electricity*, Osaka, Japan, International Commission of Atmospheric Electricity, 96-99.

Takahashi, T., 1978: Riming electrification as a charge generation mechanism in thunderstorms. *J. Atmos. Sci.*, **35**, 1536-1548.

Taylor, W. L., Brandes, E. A., Rust, W. D., and D. R. MacGorman, 1984: Lightning activity and severe storm structure. *Geophys. Res. Lett.*, **11**, 545-548.

Uman, M. A., 1987: *The Lightning Discharge*. Academic Press, Orlando, Florida, 377 pp.

Vonnegut, B., 1963: Some facts and speculations concerning the origin and role of thunderstorm electricity. *Meteorol. Monogr.*, **5**, 224.

Vonnegut, B., 1982: The physics of thunderclouds. In *CRC Handbook of Atmospherics*, Vol. 1, CRC Press, Boca Raton, Florida, 1.

Warwick, J. W., Hayenga, C. O., and J. W. Brosnahan, 1979: Interferometric directions of lightning sources at 34 MHz. *J. Geophys. Res.*, **84**, 2457-2468.

Waterman, P. C., 1969: Scattering by dielectric obstacles. *Alta Frequenza*, (Speciale), 348-352.

Weisman, M. L., and J. B. Klemp, 1982: The dependence of numerically simulated convective storms on vertical wind shear and buoyancy. *Mon. Wea. Rev.*, **110**, 504-520.

Weisman, M. L., and J. B. Klemp, 1984: The structure and classification of numerically simulated convective storms in directionally varying wind shears. *Mon. Wea. Rev.*, **112**, 2479-2498.

Williams, E. R., 1989: The tripole structure of thunderstorms. *J. Geophys. Res.*, **94**, 13151-13167.

Williams, E. R., Cooke, C. M., and K. A. Wright, 1985: Electrical discharge propagation in and around space charge clouds. *J. Geophys. Res.*, **90**, 6059-6070.

Williams, E. R., Weber, M. E., and R. E. Orville, 1989a: The relationship between lightning type and convective state of thunderclouds. *J. Geophys. Res.*, **94**, 13213-13220.

Williams, E. R., Weber, M. E., and C. D. Engholm, 1989b: Electrical characteristics of microburst producing storms in Denver. *Preprints, 24th Conf. Radar Meteor.*, Tallahassee, Florida, Amer. Meteorol. Soc., 89-92.

Williams, E. R., Zhang, R., and J. Rydock, 1991: Mixed-phase microphysics and cloud electrification. *J. Atmos. Sci.*, **48**, 2195-2203.

Zrnic, D. S., Bringi, V. N., Balakrishnan, N., Aydin, K., Chandrasekar, V., and J. Hubbert, 1993: Polarimetric measurements in a severe hailstorm. *Mon. Wea. Rev.*, **121**, 2223-2238.